CENTRO DE INVESTIGACIONES
EN OPTICA, A.C.

“IMPLEMENTATION OF ALTERNATIVE ORGANIC ANODES BASED ON PROCESSABLE GRAPHENE DERIVATIVES AND APPLIED TO SOLAR CELLS”

Thesis submitted in fulfillment of the requirements for the degree:

Ph.D. in Sciences (Optics)

Author:

MSc. Alvaro-Abdiel Guerra-Him

Advisor:
Dr. José-Luis Maldonado-Rivera

León · Guanajuato · Mexico

Febraury 2024

IMPLEMENTATION OF ALTERNATIVE ORGANIC ANODES BASED ON PROCESSABLE GRAPHENE DERIVATIVES AND APPLIED TO SOLAR CELLS

MSc. Alvaro-Abdiel Guerra-Him

Thesis submitted in fulfillment of the requirements for the degree:

Ph.D. in Sciences (Optics)

Advisor:

Dr. José-Luis Maldonado-Rivera

Research Line:

Photonics

Research Group:

Group of Optical Properties of Materials (GPOM)

OPTICAL RESEARCH CENTER

PHOTONICS

LEÓN, GUANAJUATO, MEXICO

FEBRAURY 2024

Abstract

This work presents the fabrication, characterization, and application of cost-effective, semi-transparent alternative anodes for optoelectronic devices, particularly in photovoltaic applications. Graphene derivatives, SPGSW (solution-processed graphene suspended in water) and PGD (processable graphene derivative), were mechanically synthesized and suspended in water. These derivatives served as alternative anodes in two setups: (1) a three-layer graphene anode (TLGA) with SPGSW/PH1000/PH1000 and PGD/PH1000/PH1000 configurations, PH1000 is a conductive PEDOT:PSS polymer. Both SPGSW and PGD films were deposited via drop-casting on a glass substrate and treated with hydriodic acid (HI) and UV-ozone plasma. The transmittance (T) and electrical resistance (R) parameters of these anodes were T (at 550 nm) $\sim$ 78 % and R $\sim$ 88 Ω/sq; and T (at 550 nm) $\sim$ 74 % and R $\sim$ 170 Ω/sq for SPGSW and PGD based electrodes, respectively. (2) The hybrid multilayer graphene anode (HMGA), comprising a PH1000:PGD (4:1 v/v) bulk hetero-junction (BHJ) with 6 layers, was spin-coated onto a glass substrate and treated with HI. HMGA achieved T (at 550 nm) $\sim$ 79 % and R $\sim$ 134 Ω/sq. The chemical, structural, and morphological characteristics of these anodes were analyzed using various techniques: Raman spectroscopy, XRD, optical microscopy, AFM and FESEM. To validate the opto-electronic application, they were implemented, as a concept test, in organic solar cells (OSCs) based on the PM6:Y7 blend. Preliminary results indicated a power conversion efficiency (PCE) $\sim$ 4 % for TLGA based on PGD, $\sim$ 1.4 % for HMGA and $\sim$ 8 % for ITO (control OSCs). These results suggest that graphene derivatives have a promising application as an alternative electrode to ITO in photovoltaic devices, offering an opportunity to improve manufacturing processes. Additionally, it is noteworthy that both, electrodes and OSCs, were manufactured under regular atmosphere conditions; it was achieved through the use of a top electrode implemented in the solar devices based on Field's Metal (FM), a eutectic alloy of Bi, In, and Sn, deposited by drop-casting at low-temperature (T $\sim$ 95 °C), eliminating the need of high vacuum techniques.

Acknowledgments

First of all, I would like to thank God for guiding me in this new academic stage, which has brought new challenges and knowledge. I would also like to express my sincere gratitude to my wife, Kenia-María Rodríguez-Camaño, for her unconditional support during all these years of study. Likewise, I would like to thank my family and my wife's family, who, despite the distance, have always been present to encourage and support me.

I would like to express my deep gratitude to Dr. José-Luis Maldonado-Rivera for his invaluable support, wisdom, humility, and friendship that he has offered me as a researcher, teacher, and human being during these years of dedication and academic endeavor. Honestly, words are not enough, but I will always be grateful to you for everything.

I thank Drs. Mario Rodríguez, Salvador Fernández-Tavizón$^{\dagger RIP}$, and Bernardo Frontana-Uribe for all the advice, support, corrections, and knowledge, as well as their humility, that they have offered me at all times throughout the Ph.D. process. Thank you for everything.

I would also like to thank all my colleagues who are and have been members of the GPOM: MSc. Andrés Plaza, Dr. Julio Carrillo, Dr. Yaily Fernández, Dr. Sarahí García, MSc. Abril Dzib, and Dr. Jonatan Rodríguez for all their advice, feedback, help and guidance in the fabrication of solar cells to test graphene electrodes and most of all for their friendship. I would also like to thank Martín Olmos for all his technical assistance.

I thank CONAHCYT for the financial support provided through the Ph.D. scholarship. I also appreciate the financial support from CONAHCYT through the National Laboratory of Graphenic Materials (LNMG) and partial support from Fondo Institucional para el Desarrollo Científico, Tecnológico y de Innovación (FORDECyT-PRONACES, CONAHCyT) (Grant No. 51472), Mexico. Likewise, I would like to thank the Optical Research Center, A.C. (CIO) for giving me the opportunity to develop professionally and my scientific thinking skills, as well as allowing me to take full advantage of the infrastructure and equipment necessary to develop this Ph.D. project.

I would like to thank C. Albor (CIO - León) for her help with the XRD and FESEM analyses; Drs. J. Rodríguez and M. Güizado-Rodríguez (CIICAp - UAEM) for the FESEM measurements; Drs. C. Fraustro-Reyes (CIO - Aguascalientes), A. Rodríguez-Rojas (Universidad de Guadalajara - Lagos de Moreno), R. Sato-Berrú (ICAT - UNAM) and MSc. G. Gutiérrez-Valencia (CIO - León) for the Raman spectroscopy measurements and fruitful discussions; Dr. R. Galindo (U de Gto.) for different graphene film treatments.

I thank the University of Panama for giving me the opportunity to go and prepare myself professionally outside of Panama, through the Generational Relay Project of the Department of Physics of the Faculty of Natural Sciences, Exact and Technology.

Finally, I thank all my friends and colleagues who have supported me and encouraged me to move forward. A special thanks to Gustavo Gutiérrez, Yanier and family, Yaily and family, Wilson and family, Gloria Elizabeth and family, Jonatan and family, Luis González, Dayver Daza, Johan Buriticá and Jaiver Chicangana.

Dedication

This thesis is dedicated to:

- *Guerra-Rodríguez Family: Kenia Rodríguez de Guerra and Miguel Guerra Rodríguez.*
- *Guerra-Him Family: Francisco Guerra, Agueda Him de Guerra, Luz Guerra Him, Griselda Luz Cortéz (Vita)*$^{\dagger RIP}$.
- *Rodríguez-Camaño Family: Carlos Rodíguez (Padre), Fimia Camaño (Madre), Carlos Rodríguez Camaño (Calitín), Fimia Rodríguez Camaño (Eli), Isaac Rodríguez Camaño, Yeimy Mosquera and Nathaly Peralta Mosquera*
- *Rodríguez-Cerrud Family: Carlos Rodríguez Camaño (Calito), Julissa Cerrud, Alejandra Rodríguez Cerrud and Thiago Rodríguez Cerrud.*

Contents

List of Figures

List of Tables

List of Abbreviations

2D = Two-dimensional

θ = Zenith Angle

a = Cell Area in m^2

A = Acceptor Material

A-layer = Acceptor-layer

AFM = Atomic Force Microscopy

Ag = Silver

AgNWs = Silver Nanowires

Al = Aluminum

Al_2O_3 = Aluminum oxide

AM = Air Mass

Au = Gold

AZO = Aluminum Zinc Oxide

BHJ = Bulk Hetero-Junction

BHJ-OSCs = Bulk Hetero-Junction-Organic Solar Cells

Bi = Bismuth

BN-Py = Bipyridine with a B←N coordinative bond

Br = Bromine

BTI = Bithiophen Imide

C = Carbon

Ca = Calcium

$CaTiO_3$ = Calcium Titanate

CB = Conductive Band

CdS = Cadmium Sulfide

CdTe = Cadmium Telluride

CIGS = Copper Indium Gallium Selenide

Cl = Chlorine

CO_2 = Carbon Dioxide

CNTs = Carbon Nanotubes

Cs = Cesium

Cu = Copper

CVD = Chemical Vapor Deposition

D = Donor Material

D-layer = Donor-layer

DMSO = Dimethyl Sulfoxide

DSSCs = Dye-Sensitized Solar Cells

Eg = Bandgap

EQE = External Quantum Efficiency

ETL = Electron Transport Layer

FA = Formamidinium

FESEM = Field Emission Scanning Electron Microscopy

FF = Fill Factor

FM = Field's Metal

FTO = Fluorine-doped Tin Oxide

GaAs = Gallium Arsenide

GO = Graphene Oxide

HOMO = Highest Occupied Molecular Orbital

HI = Hydriodic Acid

HMGA = Hybrid Multilayer Graphene Anode

HTL = Hole Transport Layer

I = Iodine

I_0 = Reverse Saturation Current

I_L = Light-Generated Current

In = Indium

IPCE = Incident Photon-to-Current Conversion Efficiency

I_r = Irradiance

I_{SC} = Short-Circuit Current

ITO = Indium Tin Oxide

IZO = Indium Zinc Oxide

J_0 = Reverse Bias Saturation Current Density

J_m = Maximum Power Current Density

J_{ph} = Photocurrent

J_{SC} = Short Circuit Current Density

J_{SC-EQE} = J_{SC} obtained from the EQE

J_{SC-J-V} = J_{SC} derived from the J-V curve

J-V curve = Current Density-Voltage curve

k = Boltzmann's constant

LBG = Low Bandgap

LPE = Liquid Phase Exfoliation

LUMO = Lowest Unoccupied Molecular Orbital

MA = Methylammonium

MBG = Medium Bandgap

n = Ideality factor

NFAs = Non-Fullerene Acceptors

NIR = Near Infrared Region

NREL = National Renewable Energy Laboratory

OM = Optical Microscopy

OSCs = Organic Solar Cells

P_{in} = Incident Solar Power

PAs = Polymeric Acceptors

Pb = Lead

PCE = Power Conversion Efficiency

PDI = Perylene Diimide

PGD = Processable Graphene Derivative

P_m = Maximum Power Point

PV = Photovoltaic

q = charge of an electron

R = Electrical Resistance

R2R = Roll-to-Roll

R_s = Series Resistance

R_sh = Shunt Resistance

RVB = Resonant Valence Bond

Si = Silicon

SMAs = Small Molecule Acceptors

SMDs = Small Molecule Donors

Sn = Tin

SnO_2 = Tin (IV) Oxide

$S(\lambda)$ = Photons per second

SPGSW = Solution-Processed Graphene Suspended in Water

STC = Standard Conditions

T = Temperature

T (at 550 nm) = Transmittance at 550 nm

TCEs = Transparent and Conductive Electrodes

Ti = Titanium

TiO_2 = Titanium Dioxide

TLGA = Three-Layer Graphene Anode

UV = Ultraviolet Region

VB = Valence Band

V = Voltage

Vis = Visible Region

V_{loss} = Volatge Losses

V_m = Maximum Power Voltage

V_{OC} = Open Circuit Voltage

WBG = Wide Bandgap

WT = Without Treatments

XRD = X-Ray Diffraction

Chapter 1

Introduction

In recent years, the planet has suffered considerable deterioration due to global warming and the increase in greenhouse gases; consequently, human health and the global economy have also been seriously affected [1]. Some reports have made it clear that environmental conditions, food production and access to water are aspects that have been considerably affected by the pollution [2] generated through the combustion of coal, oil, gasoline, diesel and other fossil fuels that we use every day. Figure 1-1 shows global fossil fuel consumption broken down by coal, oil and gas from 1800 to 2022, as well as fossil fuel consumption by country [3]. On the other hand, various studies have shown that the concentration of toxic gases (particularly CO_2) increases rapidly almost hundred times faster, causing geological atmospheric changes and global warming [4]. These reports and studies are a clear and forceful warning that it is necessary and important to carry out a transition process from fossil fuels to clean and renewable energies [5]; this is not only due to the depletion of fossil fuels but also to avoid further damage to the environment and, therefore, affecting our health and economy. Renewable resources such as wind, tidal, thermal, biomass and solar are energy sources that can contribute to reducing pollution and its effects on the environment.

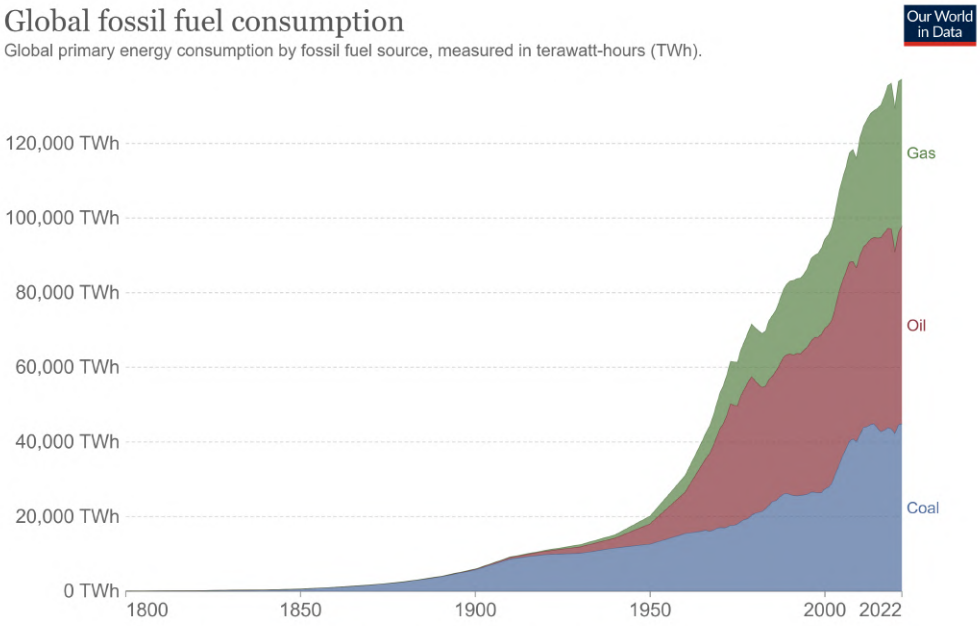

(a)

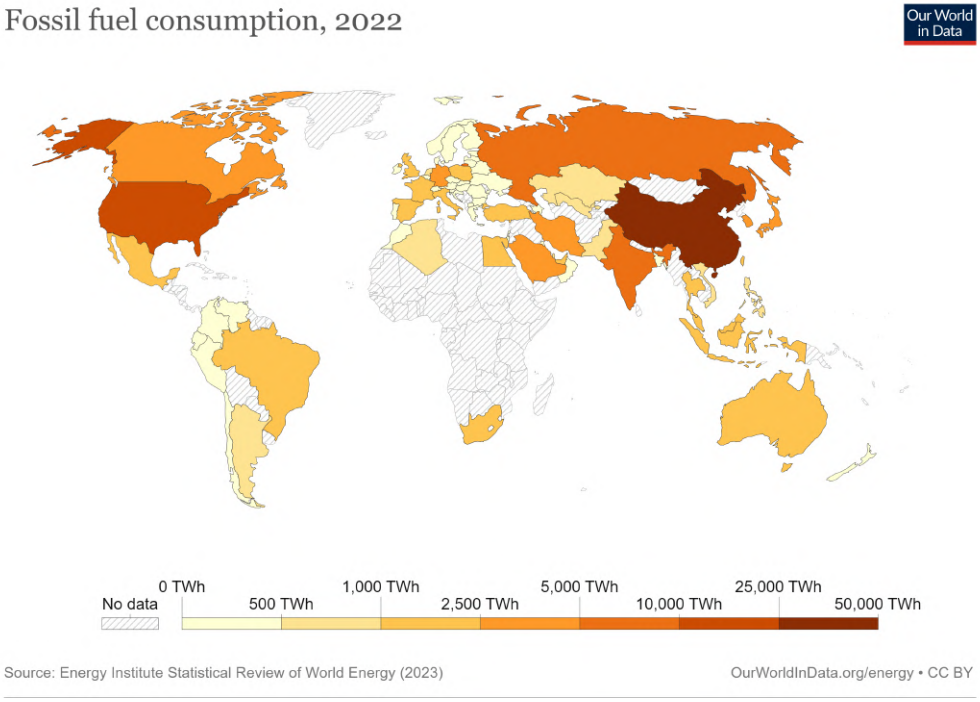

(b)

Figure 1-1: Fossil fuel: (a) Global fossil fuel consumption and (b) Fossil fuel consumption by country.

In this context, solar energy has become a promising alternative since it is a resource available to everyone and at no cost. The Sun generates large amounts of energy ($\sim 6.4\times10^7$ W/m^2), through the fusion of hydrogen nuclei, in the form of electromagnetic radiation. About this radiation, $\sim$ 1 370 W/m^2 hits the Earth's atmosphere and $\sim$ 980 W/m^2 reaches the Earth's surface [6]. Solar energy can be converted into electrical energy through the use of photovoltaic (PV) devices. These PV technologies can be classified in three generations [6, 7]:

- **First Generation** consists of PV devices based on Si and GaAs. These devices have high efficiencies and they dominate the current market. However, its manufacturing process is very expensive and complex; for example, obtaining pure crystalline silicon is extremely costly and difficult.

- **Second Generation** is based on PV devices made of thin films of inorganic materials such as cadmium telluride (CdTe), cadmium sulfide (CdS) and solar cells constructed from copper indium gallium selenide (CIGS).

- **Third Generation** is called emerging PV technologies.The Organic solar cells (OSCs), and Perovskite solar cells (PSCs) are some of these technologies; which have attracted a lot of attention due to their increased power conversion efficiency (PCE) and better properties such as mechanical flexibility, light weight, semitransparency, and low-cost roll-to-roll (R2R) processing techniques [8].

This work will focus on PV third generation materials and technologies. In recent years, a remarkable PCE over 19 % [9] and 20 % [10] for OSCs and 26 % [11] for PSCs have been reported. Figure 1-2 shows the highest levels of research efficiency that have been obtained for different types of solar cells [12]. These alternative devices are in an advanced stage of development that brings them closer to their future commercialization, which could make these devices more economically affordable to the world for the generation of electrical energy. However, these devices still face challenges such as reproducibility, stability, toxicity, life time, among others, which must be resolved before these emerging technologies can be a reality in the market [13].

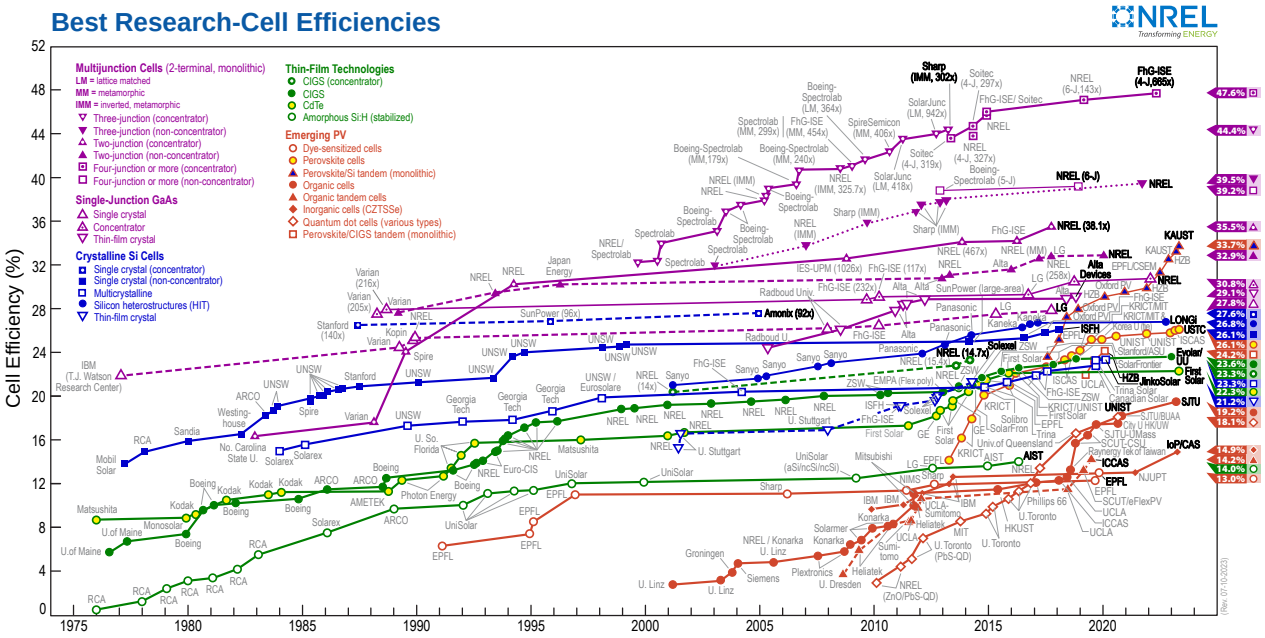

Figure 1-2: Best research-cell efficiencies to 2023. Link: https://www.nrel.gov/pv/cell-efficiency.html.

A very interesting proposal to overcome some of the limitations of third generation PV devices is the incorporation of carbon-based materials due to the properties they offer. In this aspect, graphene (2D material, an allotrope of carbon with a hexagonal honeycomb structure [14]) has generated great interest in the scientific community since its discovery in 2004 [15]. This is due to its unique properties such as large surface area (2 630 m^2/g), high electron mobility (200 000 $cm^2\ V^{-1}\ s^{-1}$), flexibility, stability, notable optical transmittance (97.7 %) and high thermal conductivity (3 000 – 5 000 W $m^{-1}\ K^{-1}$) [14]. Thanks to these properties, graphene and its derivatives have been incorporated into different layers of solar devices to improve their performance and stability. Among some of the layers, we have: hole transport layer (HTL) [16, 17], electron transport layer (ETL) [18, 19], active layer [8] and electrodes (anode or cathode) [20, 21]; in this latter use, the anode has been the most studied electrode.

In the field of electrodes, particularly in the anode, at laboratory level, ITO (indium tin oxide) is the transparent and conductive electrode (TCE) that leads the market applied to photovoltaic devices. ITO has advantages such as low electrical resistance ($\sim$ 10 - 15 $\Omega\ sq^{-1}$),

high optical transmittance (> 90 %), work function (~ 4.8 eV) and electrochemical stability. However, it also presents disadvantages such as sensitivity to acid/temperature, mechanical brittleness and high manufacturing costs. The latter is due to two aspects: (1) its deposition is achieved by sputtering, which is a complex and high vacuum technique and (2) indium is one of the main chemical elements in the manufacture of ITO and is scarce in the Earth's crust [22,23]. Due to limitations of the ITO, various alternatives have been explored to harness very promising properties of graphene, among these the abundance of carbon precursors on the Earth´s crust and the simpler techniques required to process it [22, 24]. However, the synthesis, processing and deposition of graphene and its derivatives also present challenges that must be overcome for these alternative materials to be able to compete with ITO.

In this work, a simple and low-cost method based on drop-casting and spin-coating techniques is proposed to fabricate alternative electrodes composed of a conductive polymer PEDOT:PSS (PH1000) and two graphene derivatives: (1) solution-processed graphene suspended in water (SPGSW) and (2) processable graphene derivative (PGD). Both graphene derivatives were mechanically synthesized. The manufactured electrodes were implemented as anodes in OSCs based on PM6:Y7 as concept test to demonstrate the application of both, the graphenic materials and the manufactured electrodes in photovoltaic devices. The following aspects should be noted: (1) the entire manufacturing process of the electrodes and the OSCs (direct architecture) can be performed under regular atmospheric conditions. (2) The cathode implemented in the OSCs was Field's Metal, which is a eutectic alloy of In (51 %), Bi (32.5 %) and Sn (16.5 %); this cathode does not require high vacuum deposition methods. (3) The graphenic materials used are free of doping of metallic nanomaterials.

Chapter 2

Solar cells evolution

2.1 State-of-art

2.1.1 OSCs

In 1958, Kearns and Calvin reported the first organic solar cell (OSC) with a pristine organic material (magnesium phthalocyanine) placed between two electrodes, which achieved a very low power conversion efficiency (PCE) ($\leq$ 0.1 %), which remained without major changes for more than 20 years [25]. By 1986, Tang manufactured the first bilayer hetero-junction OSCs with a PCE $\sim$ 1 % [26]; however, only the excitons generated at the donor-acceptor interface could be separated into the carrier charges, this was because the diffusion length of the excitons was spatially limited (10 - 20 nm) [27]. In 1995, Yu et al. first fabricated bulk hetero-junction (BHJ) OSCs achieving PCE $\sim$ 3 % [28]. After many years of studies, by 2005, OSCs reached PCEs between 4 - 5 % for the first time with the famous P3HT:PCBM blend, which attracted a lot of attention from the scientific community [29,30]. Subsequently, in 2015, ITIC emerged as a new molecule free of fullerenes that promised fruitful applications for the manufacturing of OSCs. Zhan et al. implemented the ITIC in combination with PTB7-TH as active layer in OSCs and achieved high-performance devices with efficiencies $\sim$ 7 % [31]. A year later, in 2016, Hou et al. mixed ITIC with PBDB-T as a fullerene-free active layer in OSCs and achieved PCEs greater than 11 % [32]. In 2018, Chen et al. manufactured tandem OSCs, which reached PCEs greater than 17 % [33]. However, by

2022, tandem OSCs achieved a record efficiency over 20 % and to date it is the maximum efficiency reported for OSCs [10]. In 2023, Fu et al. manufactured binary OSCs free of fullerene and low non-radiative recombination, reaching an efficiency of 19.31 % [9]. Today, BHJ-OSCs are the most investigated solution-processed organic devices [27]. Although the stability and efficiencies of OSCs are under constant study, these devices present several advantages compared to traditional cells (inorganic), such as [27, 34]: (1) the processability of the organic semiconductor solution provides great potential for the low-cost large area OSCs manufacturing; (2) low temperature processing reduces energy consumption during manufacturing, further reducing energy recovery time; (3) the ability to print on plastic substrates results in applications such as in wearable and flexible electronics.

2.1.2 PSCs

In 2009, Kojima et al. reported the first implementation of a perovskite ($MAPbI_3$) active layer in DSSCs, using a liquid electrolyte as hole transport layer (HTL) and achieving an efficiency of 3.8 % [35]. Despite this success, they observed that the perovskite was soluble in the electrolyte, which accelerated its degradation (less than an hour stability). Nevertheless, the experiment demonstrated the feasibility and potential of perovskite as a light-absorbing layer, revealing great potential in photovoltaic devices. Since then, several research groups have focused on optimizing perovskite deposition and manufacturing methods to improve the performance of PV devices using this active layer. In 2012, Kim et al. fabricated rigid PSCs using spiro-OMeTAD as HTL instead of a liquid electrolyte. They achieved an efficiency of 9.7 % and demonstrated device stability for 500 hours without encapsulation [36]. In the same year, Lee et al. reported PSCs with a rigid structure using Al_2O_3 as the scaffold layer instead of TiO_2, achieving efficiencies close to 11 %. This device exhibited improved charge transport properties and enhanced stability. In addition, they found that perovskite had the ability to transport both electrons and holes [37]. In 2015, Chen et al. reported the development of PSCs with a rigid inverted (p-i-n) structure, which achieved a record efficiency of 15 %. In addition, they highlighted the excellent stability of the device under light exposure for more than 1000 hours [38]. These results have led to increased interest in research aimed

at improving the efficiency of PSCs with an inverted configuration. For 2017, Zhen et al. reported inverted PSCs with a PCE greater than 20 % [39]. Then, in 2020, Zheng et al. reported for the first time inverted PSCs with efficiencies of 22.3 % [40]. In 2021, Min et al. presented PSCs with a record efficiency of 25.8 % [41], marking a significant milestone for these devices. In these PSCs, an interlayer was implemented between the electron transport layer (ETL) and the active layer to mitigate interface defects. Even without encapsulation, these devices were able to maintain $\sim$ 90 % of their initial efficiency even after 500 hours of continuous light exposure. These results indicate the possibility of improving both the efficiency and stability of the device by reducing defects at the interface between the ETL and the active layer. On the other hand, for 2022, the inverted PSCs presented a significant increase in their efficiency. At the beginning of the year, efficiencies greater than 23 % were reported and by the end of the year, the PSCs had already achieved efficiencies greater than 26 % [11, 42–44].

2.2 Active layer materials

2.2.1 OSCs

BHJ-OSCs, in basic form, are composed of transparent electrodes, an active layer, and hole and electron transport layers. Specifically, the active layer in these devices is composed of a material that acts as an donor (D) and another that acts as an acceptor (A). In general, these D and A materials are organic molecules that containing a π-conjugated backbone [45]. Such materials are mixed to form an interpenetrating network, which favors the efficient dissociation of excitons and facilitates rapid charge transfer to the corresponding electrodes [27]; therefore, D and A materials play an essential role in BHJ-OSCs to achieve high efficiencies [46]. These materials must have certain properties, such as [45,46]: (1) matching absorption spectrum; (2) proper molecular energy level alignment; (3) nanoscale phase separation; (4) high mobility of charge carriers; (5) favorable solubility; (6) appropriate geometry.

2.2.1.1 Acceptor materials

- **Fullerene acceptors:**

In 1992, Sariciftci et al. first identified that photoinduced electrons could be transferred from the polymer to the fullerene cage [47]. From then until before 2015, $PC_{61}BM$ and $PC_{71}BM$ were the dominant fullerene-based acceptors in BHJ-OSCs due to their high electron mobility (10^{-3} cm^2 V^{-1} s^{-1}), isotropic charge transport behavior, and high electron affinity. Despite these advantages, fullerenes limited the performance of organic devices due to their inherent weak absorption, unsustainable energy levels, large voltage losses (V_{loss}), morphological instabilities, etc [27]. Due to these limitations, the scientific community began to study the structure of the $PC_{61}BM$ to determine which variables they could modify and thus improve the efficiency of the OSCs. Figure 2-1 shows the chemical structures of $PC_{61}BM$ and $PC_{71}BM$ [46]. $PC_{61}BM$ is composed of a C_{60} fullerene cage, an aryl group, an alkyl chain and a terminal group (figure 2-1c), so there are four possible variables to improve the efficiency of fullerene-based OSCs: (1) modify the aryl group, (2) vary the length of the alkyl chain, (3) modify the terminal ester group, and (4) change the fullerene cage with highly absorbent higher fullerenes. However, in most cases, $PC_{61}BM$ modifications did not make a significant difference in the PCE of BHJ-OSCs; therefore, fullerene derivatives with higher C_{70} fullerene content were introduced into the OSCs fields [46]. However, fullerene-based OSCs are still limited, so it is necessary to explore new materials to further improve the photovoltaic performance of OSCs [27].

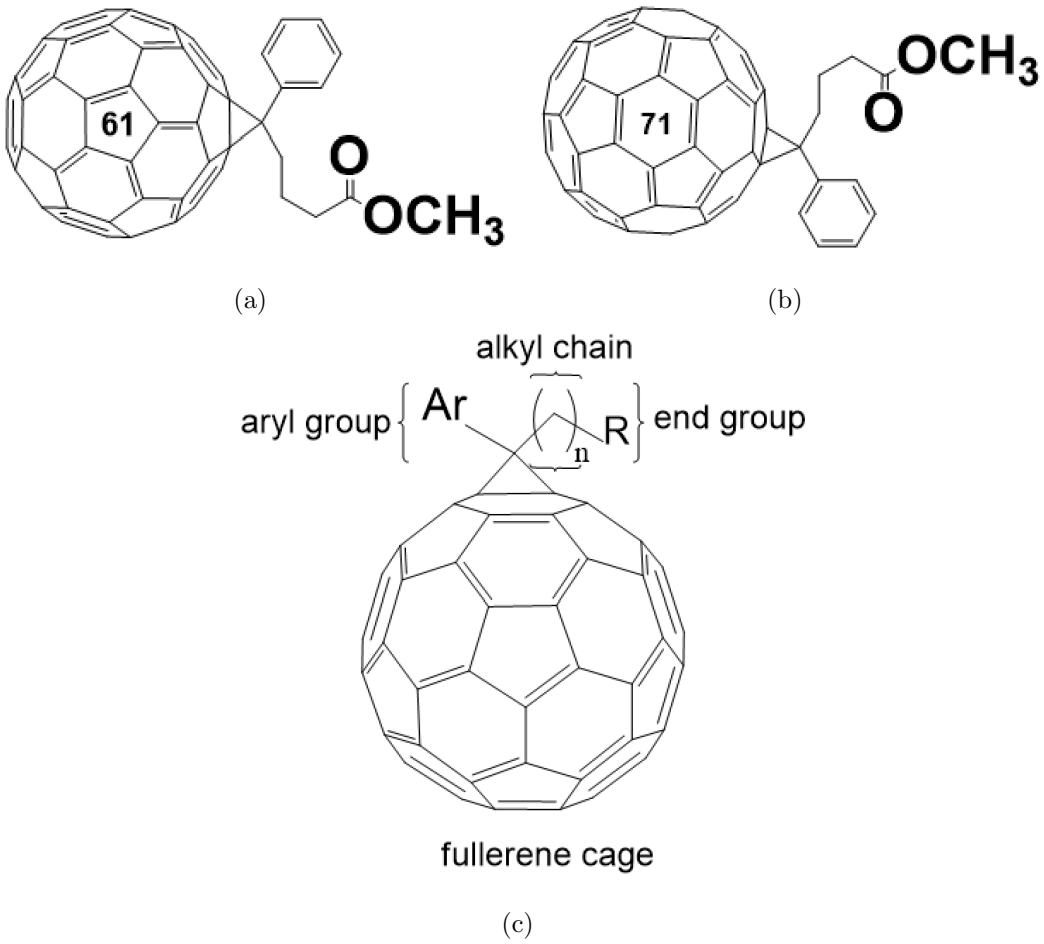

(a) (b)

(c)

Figure 2-1: Chemical structures: (a) $PC_{61}BM$, (b) $PC_{71}BM$ and (c) Parts of the $PC_{61}BM$.

- **Non-fullerene acceptors (NFAs)**

Since the emergence of the ITIC molecule in 2015 [31], NFAs have attracted a lot of attention due to their characteristics such as [27, 46]: stronger light absorption with a readily tuneable energy levels, higher electron mobility, improved D and A materials miscibility compared with fullerene acceptors and easy synthesis methods. Furthermore, the performance of OSCs with NFAs has shown significant progress in recent years. NFAs are also divided into two groups [27, 46]: (1) small molecule acceptors (SMAs), within which we have: perylene diimide (PDI) that are characterized by having a broad and planar structure, high photochemical stability, easy synthesis and modification, which have been widely used as n-type materials; unfused-ring SMAs refer to those with partially or completely unfused backbone

structures, where non-covalent intramolecular interactions are used to mediate the planarity of the molecular structures. These molecules can usually be prepared by simple synthesis methods; among others SMAs are the ITIC, Y6 and L8-BO. (2) Polymeric acceptors (PAs) have notable characteristics that SMAs cannot provide, such as good film-forming performance. Furthermore, all-polymeric solar cells offer potential advantages such as structural flexibility and long-term morphological, thermal and mechanical stability. Among some PAs materials are: bithiophen imide (BTI) with advantages of coplanar structure, short intermolecular $\pi \cdots \pi$ stacking distance and favorable orientations of solubilizing substituents to synthesize new n-type semiconductors; among others are bipyridine with a B←N coordinative bond (BN-Py), PDI and PBN-12.

2.2.1.2 Donor materials

Donor materials also play an important role in OSCs. Initially, conjugated polymers such as P3HT, PTB7, PTB7-Th, among others, were synthesized to match with fullerenes and their derivatives to improve the capacity of the active layer to harvest light in OSCs [27]. Donor materials can be classified, according to their bandgap (E_g), into three types: wide bandgap (WBG, $E_g > 1.8$ eV), medium bandgap (MBG, 1.6 eV $< E_g \leq 1.8$ eV) and low bandgap (LBG, $E_g \leq 1.6$ eV) [46]. P3HT is one of the most relevant donor materials due to its large-scale preparation and ease of tuning of opto-electronic properties. However, OSCs with active layer P3HT:$PC_{61}BM$ achieved a PCE of only 5 % due to the super miscibility between P3HT and fullerenes and their derivatives, which leads to poor phase separation in the active layer and restricts its later development [27]. Another donor polymer is PTB7, which was soon superseded by its derivative PTB7-Th with 2-ethylhexyl-thienyl units introduced into the BDT group. This derivative of PTB7 presented an increase in molecular coplanarity and the absorption coefficient, as well as a decrease in its bandgap. The first OSCs with PTB7-Th:$PC_{70}BM$ active layer achieved a PCE of $\sim$ 10 % [27]. On the other hand, narrow bandgap NFAs have been used as a complement to synthesize WBG-donor polymers such as J-series, PBDB series, PTQ10 and D18, etc. Of which, PBDB-T, PBDB-T-2F (PM6) and D18 were the most used polymers due to their good processability, adequate energy levels

and better phase separation [27].

There are also small molecule donors (SMDs) that have been implemented in OSCs. These molecules have attracted a lot of attention because they present high purity synthesis with negligible variation from batch-to-batch, a well-defined chemical structure, easier purification, and defined molecular weight [27, 48]. Among some SMDs are dyes, fused acenes, oligothiophenes and triphenylamine-based molecules [48]. OSCs based on SMDs have presented, in recent years, great progress in their efficiency ($\sim$ 17 %); however, there are still key points that must be improved to achieve better development of SMDs-free of fullerenes-based OSCs; among these points is optimizing the control of morphology, since it is difficult to form a continuous interpenetrating network due to the strong crystallinity of SMDs; a solution to this would be to implement better post-processing methods or suitable additives that allow the morphology to be modulated [27].

2.2.2 PSCs

Typically, the PSCs are composed of transparent electrodes (anode and cathode), an active layer (the perovskite, a crucial element in these devices), and hole and electron transport layers. Initially, the term *perovskite* referred only to the mineral calcium titanate ($CaTiO_3$), which did not attract much interest from researchers, resulting in slow progress in the field. In the last decade, however, researchers have discovered the benefits of perovskite materials and have synthesized compounds with structures similar to calcium titanate. As a result, many research groups have incorporated perovskites into new generation solar cells, which have seen rapid development [49]. In general, the perovskite used in PSCs is a mixed organic-inorganic compound (although there are PSCs with completely inorganic perovskite) with the molecular formula ABX_3 (figure 2-2 shows the crystal structure of a perovskite). Here, A and B represent two cations, while X is an anion. A can be an organic or monovalent cation such as Ca^{2+}, Cs^{+}, methylammonium (MA $\rightarrow$ $CH_3NH_3^+$), or formamidinium (FA $\rightarrow$ $CH(NH_2)_2^+$); B can be a metal-divalent ion such as Ti^{2+}, Pb^{2+} or Sn^{2+}; and X can be a halide anion such as Cl^{-}, Br^{-} or I^{-} [49–52]. Perovskites are characterized by high light absorption coefficients, excellent charge carrier lifetime, and a relatively simple preparation process compared to pure

crystalline silicon [49]. This process includes methods such as spray-coating, dip-coating, two-step deposition (spin-coating and sublimation), chemical vapor deposition, ink-jet printing, and blade coating [52, 53].

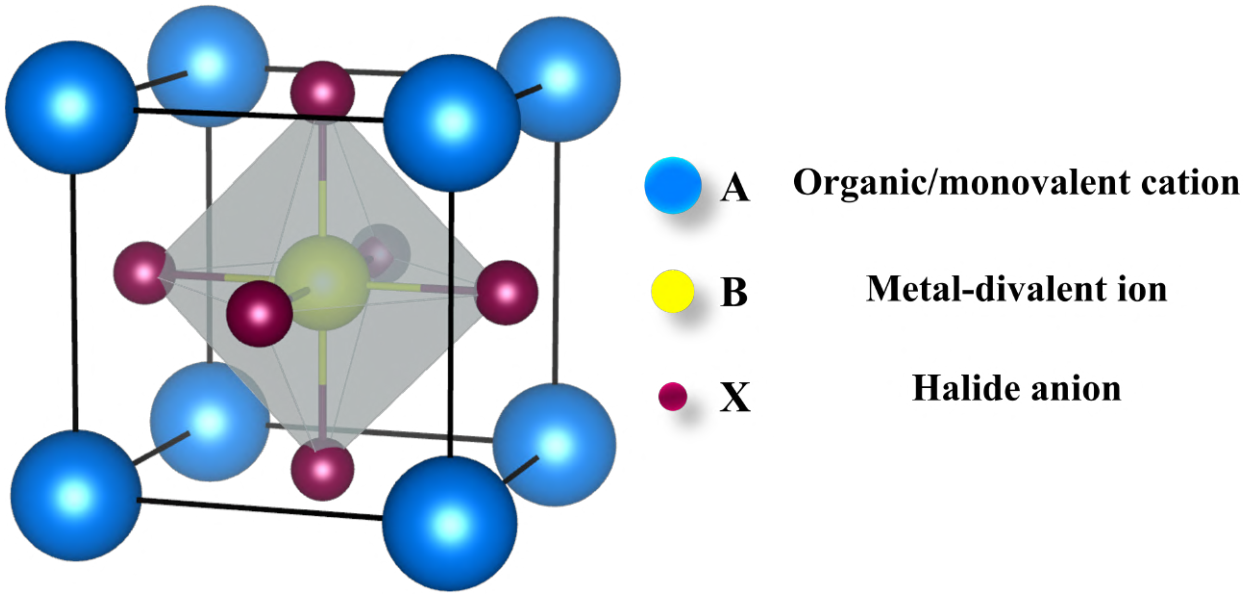

Figure 2-2: Crystal structure of a perovskite ABX_3

2.3 Operating principle

The physical operation principle of OSCs and PSCs is the photovoltaic effect. The main difference between the two devices lies in their active layer; OSCs use organic semiconducting materials, such as polymers or small molecules, while PSCs use perovskite. Both organic semiconductor materials and perovskite serve to absorb solar energy and convert it to electrical energy. The schematic diagram in figure 2-3 illustrates the common operating principle of OSCs and PSCs, which can be divided into four phases.

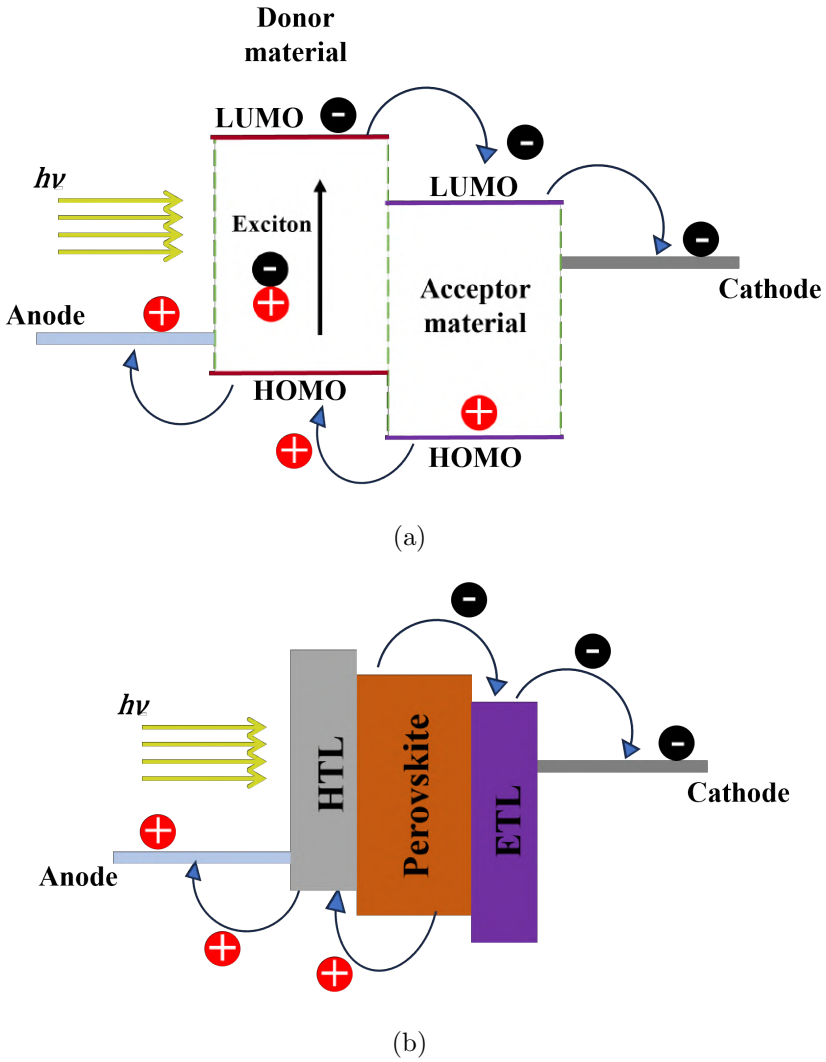

Figure 2-3: Schematic diagram of the operating principle of (a) OSCs and (b) PSCs.

- **Light absorption**

The active layer (D-A blend) in OSCs is responsible for absorbing external light (photons); during this process, the photons (with energy, hν, equal or greater than the bandgap energy of the D-A) excite the electrons in the active layer from the highest occupied molecular orbital (HOMO) to the lowest unoccupied molecular orbital (LUMO) to generate the electron-hole pair (exciton). D and A materials exhibit strong absorption in the visible spectral range to maximize the conversion of solar energy to electrical energy. However, the absorption depends on certain characteristics of D and A materials such as the chemical structure,

molecular weight, orientation of the materials and morphology of the active layer. This last characteristic plays an important role, since it must guarantee that the D and A materials are in contact and that the excitons generated by the absorption of light are separated and transported efficiently to the respective electrodes [54]. In PSCs, the electron-hole pair generation mechanism is similar to that of organic solar cells (OSCs). However, an important difference is that the active layer in PSCs is made of perovskite. In addition, the valence band (VB) and conduction band (CB) are commonly mentioned in PSCs, which correspond to the HOMO and LUMO of OSCs, respectively [49, 55].

- **Charge separation**

The excitons, once generated by the absorption of incident light, diffuse towards the interface between D and A materials in order to separate into free electrical charges. The distance that these excitons can travel, known as the exciton diffusion length, determines both the maximum possible thickness of the active layer in OSCs and the distance at which the D-A phases can be separated. In other words, if this distance is too short, the excitons will not reach the interface before decaying through radiative or non-radiative processes, resulting in a loss of energy. In general, it has been observed that in organic semiconductors, the exciton diffusion length tends to be in the range of 10 - 20 nm [34].

The excitons are dissociated into free charges at the D and A materials interface by means of a built-in electric field that is present in the active layer and occurs due to the difference in the energy levels between the LUMO and HOMO of the D and A materials. D-materials, as conjugated polymers, have high ionization potential, so they tend to donate electrons; on the contrary, A-materials, fullerenes or non-fullerenes, have low electron affinity, so they have a strong tendency to accept electrons. Again, morphology is a key piece in the dissociation process of electron-hole pairs. On the other hand, the electronic properties of D and A materials also influence the charge separation process. For example, the energy levels of D and A materials must be properly aligned to facilitate efficient charge separation. The energy offset between the LUMO and HOMO of materials D and A determines the driving force for charge separation, and adequate compensation is required to ensure that the generated

charges can be efficiently collected at the respective electrodes [54].

- **Charge collection**

The charge collection stage in OSCs refers to the process by which separated electrical charges move to the corresponding electrodes (generally composed of conductive materials such as indium tin oxide (ITO), aluminum or silver) before they decay or recombine. This process is important, since its efficiency directly affects the overall performance of the device. The charge capture efficiency is influenced by several factors such as [34, 54]: (1) the structure of the active layer; (2) the mobility of charge carriers: in a junction between D and A materials, a potential gradient is established for the electrons and holes. This is due to the displacement of the HOMO of the donor and LUMO of the acceptor. This internal gradient determines the maximum open circuit voltage and facilitates the movement of charges. Also, by asymmetrical contact arrangement, it is possible to create an external electric field. This is achieved by using a metal with a low work function to collect electrons and a metal with a high work function to collect holes. This external electric field contributes to the displacement of charge carriers, and (3) the alignment of energy levels between D and A materials. For efficient collection of electrons at the cathode and holes at the anode, it is essential to ensure the presence of adequate ohmic contact between the organic materials and the electrodes.

For PSCs, after the separation of the charges in the perovskite and due to the internal electric field, the electrons and holes start to drift and move towards the cathode and anode, respectively [49]. Previously, the photogenerated electrons and holes were injected into the CB or LUMO of the ETL and the VB or HOMO of the HTL, respectively. These injection processes are only possible due to the energy matching of the layers: the CB of the perovskite is higher than the CB or LUMO of the ETL, while the VB of the perovskite is lower than the VB or HOMO of the HTL [55].

- **Electrical output**

The electric current generated by OSCs and PSCs is the result of two essential processes: charge separation and charge collection at the electrodes. This means that the generated

carriers must reach the appropriate interfaces before recombining, otherwise the collection efficiency would decrease. The electrical generation of OSCs and PSCs is characterized by four fundamental parameters: short circuit current density (J_{SC}), open circuit voltage (V_{OC}), fill factor (FF), and power conversion efficiency (PCE). These parameters are essential indicators that help us measure and understand the quality and performance of [54] devices. These parameters are discussed in detail in Section 2.5.

2.4 Architectures

2.4.1 OSCs

OSCs can be divided into four architectures (figure 2-4): single-layer, bilayer, BHJ and tandem.

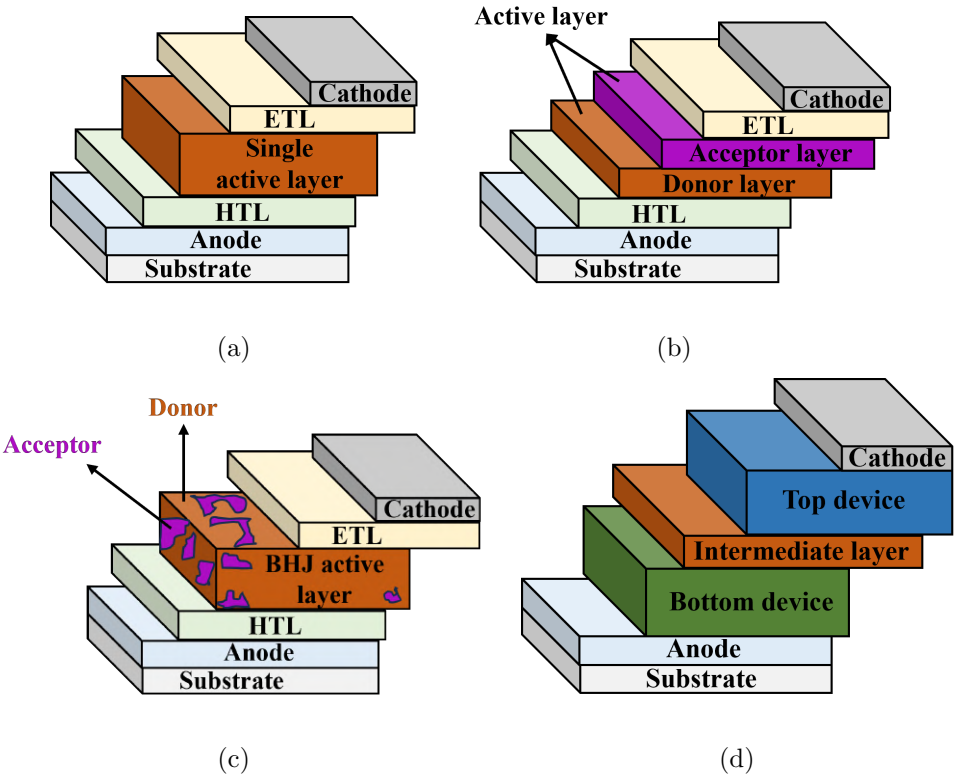

Figure 2-4: OSCs-architectures: (a) Single-layer, (b) Bilayer (c) Bulk hetero-junction (BHJ) and (d) Tandem.

- **Single-layer**

These OSCs are characterized by having a single-layer of organic material as the active layer between electrodes. These devices usually have lower efficiency compared to other architectures and this may be due to an intrinsic limitation arising from the fact that the organic layer (p-type or n-type) between the electrodes cannot adequately generate individual charges (holes and electrons) due to the extremely low charge separation performance caused by the nature of the tightly bound excitons in organic semiconductors [56].

- **Bilayer**

In bilayer OSCs, the active layer consists of two layers of organic semiconductor materials that sit between two electrodes. These two layers are generally a D-layer (usually a conjugated polymer or small molecule) and an A-layer (usually a fullerene derivative or non-fullerene acceptor) [54]. When incident light reaches the D-layer of the bilayer OSC, excitons are generated. The creation of these excitons results in an increase in the concentration of these structures, and due to this increase, the excitons begin to move towards the interface between the D and A layers [56]. Once there, the excitons separate into free electrons and holes. Subsequently, these free charges flow through their respective layers and the external electrical circuit, resulting in the generation of electrical current [54].

- **BHJ**

BHJ-OSCs are a type of photovoltaic device with a thin active layer that is composed of an interlocking structure of D and A materials. These OSCs have an improved interaction surface compared to bilayer devices. To create the BHJ, volumes of materials D and A are mixed. As a result of this mixing, the diffusion length that the excitons must travel before recombining is very short at the interface between D and A. In these devices, the excitons are generated when the active layer absorb photons from sunlight. The separation of excitons then results in the collection of charges at the corresponding electrodes, and this process takes place at the heterojunction interface [56].

- **Tandem**

A tandem OSC is, in essence, a solar device made up of two or more subcells connected in series, designed to increase their efficiency. Each of these subcells can be made of different materials and have variations in the width of their bandgap, allowing them to absorb different portions of the solar spectrum. In each subcell there are two essential components: a material that fulfills the function of absorbing the incident light, converting it into excitons, and another material that facilitates the movement of the electrons generated in this process. The union between the subcells allows the charges produced to be transferred efficiently between them. In the case of a tandem photovoltaic cell, it is common for the initial subcell to have a wider bandgap than the second subcell. This has the advantage that the first subcell can absorb high-energy photons, while the second subcell specializes in capturing low-energy photons. In short, tandem photovoltaic cells optimize solar energy conversion efficiency by harnessing a broader spectrum of sunlight and converting a greater portion of this light energy into usable electricity [54].

2.4.2 PSCs

In general, planar PSCs are divided into two structures according to the arrangement of HTL and ETL: (1) regular planar (n-i-p) PSCs, which have a configuration of cathode/ETL/perovskite/HTL/ano and (2) inverted planar (p-i-n) PSCs and its configuration is anode/HTL/perovskite/ETL/cathode [52]. Figure 2-5 illustrates the n-i-p and p-i-n architectures. regular PSCs implement ETLs such as TiO_2 and SnO_2, and HTLs such as spiro-OMeTAD; however, these devices face challenges such as high hysteresis and insufficient stability. In contrast, inverted PSCs typically employ PCBM-based ETLs and PEDOT:PSS-based HTLs; these cells have demonstrated good stability, low hysteresis and competitive efficiency. Therefore, most of the research on inverted PSCs in recent decades has focused on improving their power conversion efficiency (PCE) [57].

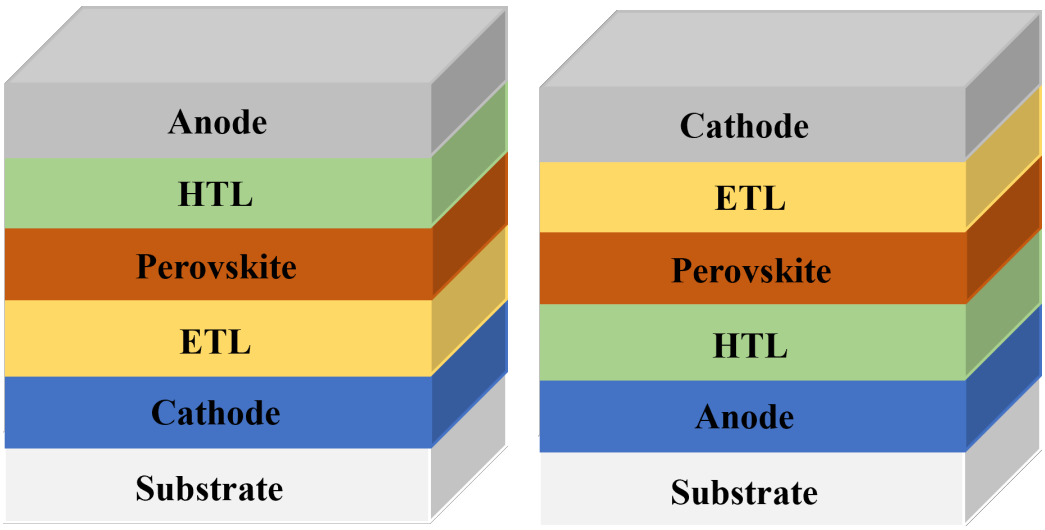

(a) (b)

Figure 2-5: Schematic diagram of the structure of PSCs: (a) n-i-p and (b) p-i-n.

2.5 J-V curve

The current density-voltage (J-V) curve (figure 2-6) represents the characteristic curve of photovoltaic devices and covers all possible operating points in terms of current and voltage. These devices are affected by various environmental conditions, such as temperature, solar radiation or humidity. To obtain this curve, standard conditions (STC) are considered, which include an irradiance (I_r) = 1000 W/m^2, and an air mass (AM) value equal to 1.5. AM coefficient provides information about the thickness of the atmosphere as a function of the zenith angle θ (see equation 2-1). For AM = 1.5, the value of θ is equal to 48.2°. This specification is used in combination with a standard power density to ensure an accurate and direct comparison of solar cell performance at different times and locations. The terms "AM 1.5G" (G stands for global), which incorporates both direct and diffuse radiation, or "AM 1.5D", which encompasses only direct radiation, are used to represent the standard spectrum of sunlight at the Earth's surface [56].

$$\mathrm{AM} = \frac{1}{\cos(\theta)} \tag{2-1}$$

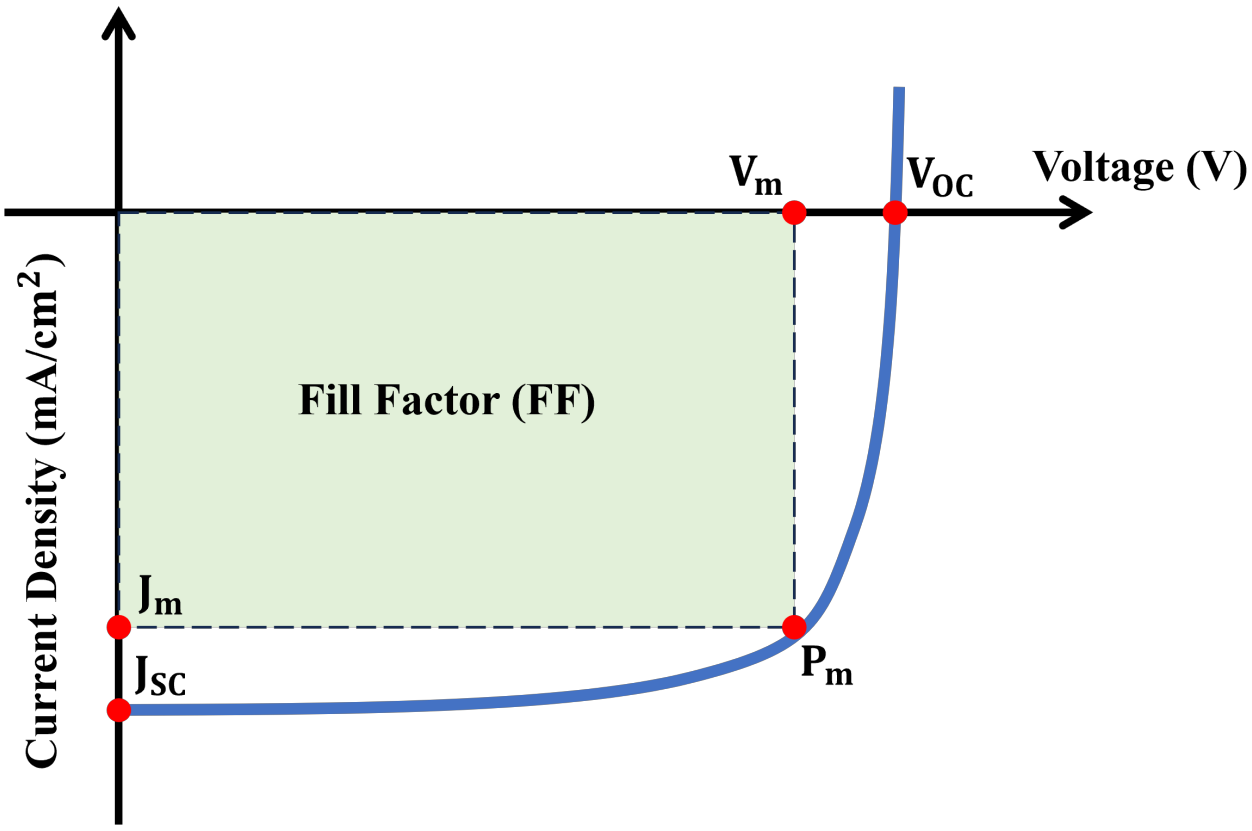

Figure 2-6: OSCs J-V curve.

From the J-V curve, it is possible to derive several photovoltaic parameters such as:

- **Open circuit voltage (V_{OC}):**

It is the maximum voltage supplied by the photovoltaic device and is a parameter that depends much more on temperature. Its unit is voltage (V). It occurs when the flow of electrons (current) is zero on the J-V curve and can be measured with a voltmeter at the device terminals, without any load connected. Theoretically V_{OC} can be determined by taking into account the difference of HOMO of the donor component and LUMO of the

acceptor component. This theoretical HOMO-LUMO difference can be correlated with the experimentally obtained value of the J-V characteristics [56]. V_{OC}, mathematically, is given by equation 2-2, where n is ideality factor, k is Boltzmann's constant, T is the temperature in Kelvin, q is the charge of an electron, I_L is the light-generated current and I_0 is the reverse saturation current [54]:

$$\mathrm{V_{OC}} = \frac{\mathrm{nkT}}{\mathrm{q}} \ln\left(\frac{\mathrm{I_L}}{\mathrm{I_0}} + 1\right) \tag{2-2}$$

- **Short-circuit current density ($\mathbf{J_{SC}}$):**

J_{SC} is directly and inversely proportional to the short-circuit current (I_{SC}) and the cell area (a), respectively. See the equation 2-3. The units of I_{SC} and J_{SC} are Ampere (A) and A/m^2, respectively. Mathematically, I_{SC} is given by equation 2-4 [54], where V is the voltage, and knowing a, J_{SC} can be calculated. On the other hand, J_{SC} is also directly proportional to the light intensity and it is the maximum current that a PV device can deliver, which happens when the voltage of PV device is zero on the J-V curve. In addition, J_{SC} is more commonly used instead of I_{SC} to eliminate the dependence of cell area.

$$\mathrm{J_{SC}} = \frac{\mathrm{I_{SC}}}{\mathrm{a}} \tag{2-3}$$

$$\mathrm{I_{SC}} = \mathrm{I_L} - \mathrm{I_0}\left[\exp\left(\frac{\mathrm{qV}}{\mathrm{nkT}}\right) - 1\right] \tag{2-4}$$

- **Maximum power current density ($\mathbf{J_m}$):**

It is the current delivered by the PV device at its maximum power point, under certain conditions of light intensity and temperature. It is used as the nominal current of the PV device.

- **Maximum power voltage ($\mathbf{V_m}$):**

It is the voltage delivered by the PV device at its maximum power point under certain conditions of light intensity and temperature. It is used as the nominal voltage of the PV device.

- **Maximum power point ($\mathbf{P_m}$):**

It is the maximum power that the PV device can supply under certain conditions of light intensity and temperature. Its unit is Watts (W) and mathematically, it is expressed as:

$$\mathrm{P_m} = \mathrm{V_m}\ \mathrm{J_m} \tag{2-5}$$

- **Fill factor (FF):**

Indicates how efficient the PV device is and quantifies the relationship between the maximum experimental power of the PV device and the maximum power of an ideal PV device, where the J-V relationship constitutes a prefect rectangle of sides J_{SC} and V_{OC}. FF is dimensionless. Mathematically, it is expressed as [54]:

$$\mathrm{FF} = \frac{\mathrm{P_m}}{\mathrm{V_{OC}}\ \mathrm{J_{SC}}} \tag{2-6}$$

- **Power conversion efficiency ($\boldsymbol{\eta}$ or PCE):**

It is the percentage of power transformed into electrical energy from the total sunlight absorbed for the operation of a given electrical circuit. Mathematically, it is expressed by equation 2-7, where, P_{in} is the incident solar power with $\mathrm{I}_r = 1000\ \mathrm{W/m^2}$ [54].

$$\mathrm{PCE} = \frac{\mathrm{J_{SC}}\ \mathrm{V_{OC}}\ \mathrm{FF}}{\mathrm{P_{in}}} \times 100\ \% \tag{2-7}$$

2.6 EQE/IPCE curve

The external quantum efficiency (EQE) or incident photon-to-current conversion efficiency (IPCE) is used as an additional measure to support the J_{SC} derived from the J-V curve

(J_{SC-J-V}) of solar devices. The EQE evaluates the conversion of an incident photon to an electron as a function of the wavelength of the photon. This measurement provides information about the different spectral regions that contribute to or cause losses in the photocurrent generation in the device [58].

Experimentally, EQE can be determined using a light source combined with a xenon lamp and a monochromator. The light source illuminates the sample through a suitable shadow mask, while the device is kept short-circuited and the current through the device is measured with a source meter for each wavelength. The raw current data must be normalized to the number of exposures by calibration to a reference solar cell with a known spectral response for each wavelength [58].

Since the EQE represents the specific response of the device under illumination, the J_{SC} can be calculated by the equation 2-8, where $S(\lambda)$ is photons per second. However, it is common for the J_{SC} obtained from the EQE (J_{SC-EQE}) to be lower than the J_{SC-J-V}, and the error range is generally between 10 - 20 % [58]. Zimmerman et al. investigated the discrepancy between J_{SC-EQE} and J_{SC-J-V} and they concluded that several factors affect this measurement, including incorrect measurement conditions, use of different shadow masks for EQE and J-V measurements, spectral response and cell calibration reference, and homogeneity and spectral matching of the light output [59].

$$J_{SC-EQE} = \int qEQE(\lambda)S(\lambda)d\lambda \tag{2-8}$$

2.7 Equivalent circuit of PV devices

The J-V curve shown in figure 2-6 is characteristic of any photovoltaic device, whether organic, inorganic or hybrid. This curve presents the behavior of a diode, so the OSCs or PSCs, from an electrical/electronic point of view, can be modeled through the simple diode model based on the Shockley relationship (equation 2-9) and its equivalent circuit is shown in figure 2-7.

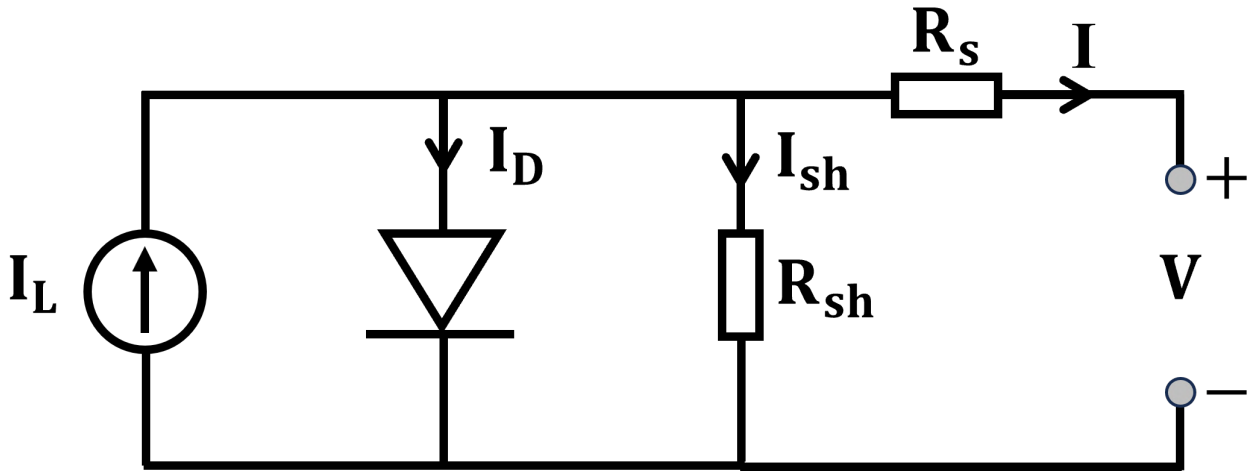

Figure 2-7: OSCs equivalent circuit.

$$\mathrm{J} = \mathrm{J}_0 \left[\exp\left(\frac{\mathrm{e}(\mathrm{V} - \mathrm{JR_s})}{\mathrm{nk_B T}} \right) - 1 \right] + \frac{\mathrm{V} - \mathrm{JR_s}}{\mathrm{R_{sh}}} - \mathrm{J_{ph}} \tag{2-9}$$

Where, J_0 is the reverse bias saturation current density, e is the elemental charge, V is the bias voltage, J is the current density through the whole device, R_s is the series resistance, n is the ideality factor of the diode, k_B is the Boltzmann's constant, T is the temperature, R_{sh} is the shunt resistance and J_{ph} is the photocurrent. From this equation, the first term on the right side corresponds to the recombination current and the second term to the shunt current. Recombination current explains how a PV device acts like diode in the dark, and the shunt current represents device leakage due to sources such as pinholes that allow parasitic current to move directly from one electrode to the other [60].

The resistances R_s and R_{sh} are parasitic resistances. R_s is known as the internal resistance of the PV device and it arises from the organic materials of the device. Also the resistance of the electrodes and the interfacial connection affect the R_s of the device. For example, the resistance of the active layer is inversely related to the mobility of the charge carriers; this means that the R_s of OSCs is higher than that of inorganic devices [61]; therefore, the electrical performance of the OSCs is affected in terms of the FF, and the mobility of charges

is affected by traps or other barriers (jumps) [62]. On the other hand, R_{sh} is due to a leakage current that occurs at the donor-acceptor and active layer-electrode boundaries. Generally, R_{sh} is related to the charge recombination process, i.e., a low carrier recombination rate under light illumination, without polarization, indicates the presence of a large R_{sh} value for the device [63]. A highly efficient OSC, in theory, should present a minimum R_s ($R_s \longrightarrow 0$) and a maximum R_{sh} ($R_{sh} \longrightarrow \infty$) [64].

2.8 Electrodes

The materials used in TCEs typically exhibit high optical transmittance, low electrical resistance, and a wide bandgap (> 3.1 eV) [65]. To achieve these properties, it is critical to understand the fundamental properties of the materials, such as their structure, surface, optical and electrical properties. In addition, TCEs should have high chemical stability and low-cost preparation process; this is essential for the production of photovoltaic devices that are long-term stable and affordable in terms of cost [66]. Several types of electrodes have been investigated, including metal oxides (ITO, FTO, IZO, AZO, etc.), conductive polymers, metal films/grids/nanowires, carbon nanotubes (CNTs) and graphene (this will be discussed in detail in chapter 3) [22, 65–67]. PEDOT:PSS, which is one of the most widely known conductive polymers, shows excellent flexibility and high optical transmittance; however, its intrinsic acidic and hygroscopic properties limit its applicability. On the other hand, metal films such as Au, Ag, Al and Cu show low resistance and acceptable transmittance; they are deposited by thermal evaporation or sputtering. However, Au and Ag have high cost, while Al and Cu tend to oxidize easily in atmospheric environment. In addition, metal grids and nanowires require complicated processes such as photolithography or spinning. CNTs have good optoelectrical performance; however, they usually have rough morphologies, which makes their application in thin-film devices difficult. In addition, CNTs are usually difficult to disperse uniformly due to Van der Waals interactions. Among some reports that implement the alternative electrodes mentioned above in OSCs and PSCs are:

- Wen et al. [68] implemented an alternative anode in flexible OSCs (PET/AgNWs

FTEs/PH1000 (100 nm)/PEDOT:PSS/PM6:Y6/PDNIO/Al) and reached a PCE of $\sim$ 12.7 %. This anode was composed of a silver nanowires (AgNWs) layer and a PH1000 (100 nm) layer. PH1000 was used to enhance the surface roughness of the AgNWs. The alternative anode showed T (at 550 nm) $\sim$ 80 - 90 % and R $\sim$ 31 Ω/sq.

- Jeon et al. [69] implemented Double-walled CNTs (DWNT) as alternative anode in PSCs (DWNT/PTAA (35 nm)/$MA_{0.6}FA_{0.4}PbI_{2.9}Br_{0.1}$ (450 nm)/C_{60} (20 nm)/BCP (6 nm)/Cu (50 nm). DWNT was doped with TFMS (2 v/v %) and reached R $\sim$ 74 Ω/sq. With this electrode, a PCE of $\sim$ 17.2 % was achieved.

- Kim et al. [70] implemented a W-doped In_2O_3 (IWO) metal oxide anode in flexible PSCs (PET/IWO/PEDOT:PSS/$MAPbI_3$/PCBM/BCP/Ag), achieving a PCE around 11.33 %. IWO reached T (at 550 nm) $\sim$ 96 % and R $\sim$ 37 Ω/sq.

Chapter 3

Graphene: general overview and an alternative promising electrode to ITO

3.1 Definition and its properties

Graphene is one of the allotropic forms of carbon. Carbon is a chemical element with symbol C, atomic number 6 and atomic mass 12.01. It is a tetravalent non-metal, having four electrons and six protons to form covalent chemical bonds. Furthermore, it is well known that carbon is one of the most abundant elements in the Earth's crust and plays an important and direct role in supporting life on Earth [71]. On the other hand, carbon has an extreme versatility, with multiple possibilities to form chemical bonds, which gives rise to the existence of a large number of carbon allotropes due to the possibility of forming different hybridization states (sp, sp^2 and sp^3) [71, 72]. Currently, various research groups have focused their efforts on studying and manufacturing novel two-dimensional (2D) carbon materials and their applications depend on what type of carbon atoms combine mutually with a variety of morphologies, including fullerenes, carbon nanotubes and graphene [71]. The latter, graphene, has attracted a lot of attention in recent years due to its exceptional properties, derived from a fortunate combination of the electronic structure of carbon, the symmetry of its network and its 2D nature [73]. Due to its 2D nature, graphene has unique different properties such as:

- **Electronic properties**

Graphene is a highly flexible material that exhibits remarkable electrical properties [14]. The structural robustness of this 2D material is due to the trigonal planar structure formed by the sp^2 hybridazed carbon atom, establishing strong σ bonds (responsible for the stability of the material) with a distance of 1.42 Å between the carbon atoms. The p orbitals, which remain perpendicular to the planar structure, generate covalent bonds with neighboring carbon atoms, forming π electronic bands. The nature of their tight bonds gives rise to high Coulomb energies, leading to prominent collective effects such as magnetism and insulating behavior due to correlation gaps. Despite this, there is an evolving theoretical understanding of its electronic properties, through the resonant valence bond (RVB) theory proposed by Linus Pauling, where the band structure of graphene classifies it as a semimetal with Dirac electrons. Most experimental investigations are based on this band structure, although electron-electron interaction in graphene remains a topic of intense research [74].

- **Mechanical properties**

Graphene stands out for its notable strength and lightness. It is extraordinarily strong (E = 1.0 TPa), and at the same time, it is extremely light (0.77 mg m^{-2}) [14]. The intrinsic strength and elastic properties of a single-layer graphene have been evaluated by nanoindentation using an atomic force microscope (AFM). These experiments have revealed that graphene shows a nonlinear response to stress-strain, and possesses a second-order elastic stiffness of 340 N m^{-1}, a third-order elastic stiffness of 690 N m^{-1}, and a resistance to fracture of 42 N m^{-1}, in addition to a Young's modulus of E = 1.0 TPa. These measurements have confirmed that graphene is the most resistant material known. Its exceptional strength and lightness make it suitable for both individual applications and to reinforce the manufacturing of composite materials [74].

- **Thermal properties**

Different forms of carbon have been studied to understand their thermal conductivity, revealing notable variations. This conductivity varies from just 0.01 W m^{-1} K^{-1} in amorphous

carbon to more than 2 000 W m^{-1} K^{-1} at room temperature in diamond and graphene [75]. An intriguing aspect focuses on how the thermal conductivity of graphene changes with the number of atomic layers. Here, two factors, one intrinsic and the other extrinsic, influence thermal transport phenomena. The extrinsic thermal properties of multilayer graphene depend on the dispersion of defects in its structure. As the number of atomic layers increases, a significant alteration in phonon scattering is observed, providing more phase space for scattering. This limits phonon scattering from the upper to lower limits, if the number of atomic layers is kept constant throughout the graphene layer [76]. The thermal conductivity of graphene has been measured using non-contact optothermal Raman techniques, in suspended graphene layers obtained by exfoliation of bulk graphite. These experiments have shown that the thermal conductivity can exceed 3 000 W m^{-1} K^{-1} at room temperature in large sheets of graphene [76]. For suspended monolayer graphene, the thermal conductivity varies between 4.84 ± 0.44 x 10^3 and 5.30 ± 0.48 x 10^3 W m^{-1} K^{-1} [74].

The electronic contribution to the thermal conductivity of undoped graphene is minimal due to the low carrier concentration. In this case, thermal conductivity is primarily governed by phonon transport, specifically through diffusive conduction at high temperatures and ballistic conduction at low temperatures. Furthermore, introducing disorder or roughness into the structure of the graphene network allows its thermal conductivity to be adjusted over a wide range. In summary, the exceptional heat conduction properties of graphene make it a promising candidate for various electronic and photonic applications [74].

- **Optical properties**

Monolayer graphene has been shown to have a high light transmittance of 97.7 % [14]. Light absorption in graphene is influenced by the fine-structure constant (α) and increases linearly with the number of stacked graphene layers, as experimentally confirmed up to five layers. Regarding reflection, graphene reflects less than 0.1 % of incident light in the visible range, increasing to approximately 2 % in the case of ten layers. Therefore, the optical absorption of graphene is proportional to the number of layers, and each layer absorbs approximately

2.3 % of the light within the visible spectrum [74].

Figure 3-1 shows the graphene hexagon-honeycomb structure, while Table 3-1 summarizes the various properties of this material.

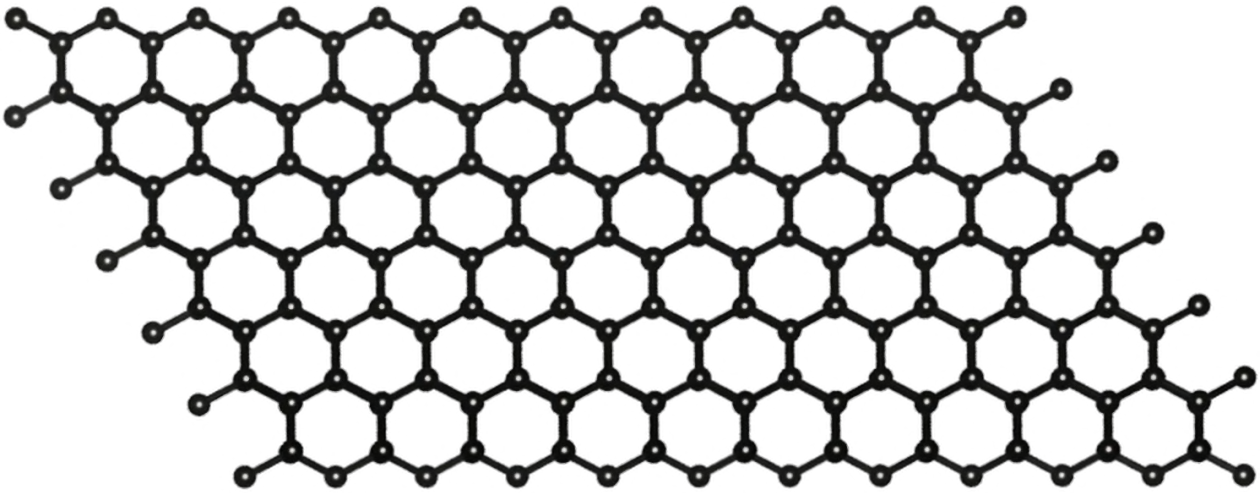

Figure 3-1: Chemical structure of monolayer graphene

Table 3-1: Properties of monolayer graphene [74, 77].

Properties	**Values**
single-atomic thickness	0.334 nm
Surface area	2 630 m^2 g^{-1}
Mobility	200 000 cm^2 V^{-1} s^{-1}
Band gap	zero-gap semiconductor
Fermi velocity	c/300 = 1 000 000 m s^{-1}
Electrons and holes near of Dirac point	They behave as massless fermions ($m^* = 0$)
Thermal conductivity	(5.3 ± 0.48) x 10^3 W m K^{-1}
Tensile strength	130 GPa
Young modulus	1 TPa

Optical absorbance	2.3 %
Optical transparency	97.7 %

3.2 Fabrication methods

Despite the incredible properties of graphene, other aspects such as the synthesis, processing and deposition of the 2D material remain a challenge. The synthesis of graphene can be divided into two methods [78]: (1) Bottom-up where it starts from a carbon precursor, and its atoms are subsequently arranged to have a high-quality graphene. Commonly used techniques are chemical vapor deposition (CVD) and epitaxial growth; however, with these techniques the amount of material produced is very small and the production cost is very high [79] and (2) Top-down, which starts from a structural base containing graphene, and then is exfoliated by physical and chemical methods (micromechanical, electrochemical, liquid phase exfoliation (LPE) of graphite and chemical exfoliation of graphite oxide) to overcome Van der Waal forces and then separate the sheets until low deffecta graphene is obtained [79, 80].

As mentioned above, the deposition of graphene and its derivatives on a desirable, usually transparent substrate (e.g., glass or plastic), for electrode fabrication also remains a challenge. CVD is one of the most effective techniques to synthesize high-quality graphene, which is even comparable to that of mechanically exfoliated graphene. The properties of CVD-graphene are affected by growth parameters, including gas mass transfer, partial pressure, substrate selection, and carbon source. Furthermore, the choice of graphene transfer process can control the overall properties of graphene. Initially, the graphene is deposited on a catalytic metal sheet (Cu, Ni), followed by a transfer process to deposit it onto a transparent substrate in order to manufacture a graphene-based electrode. Although CVD has resolved the scalability issues faced by mechanical exfoliation, CVD is expensive because it requires sophisticated, energy-intensive instruments and suffers from expensive and time-consuming graphene transfer processes. Also, from the point of view of graphene electrodes, transfer processes can generate defects in the graphene film and even contaminate it, which would affect the conductive properties of graphene [79].

3.3 Graphene electrodes implemented in solar cells

As mentioned in the introduction, the ITO, at the laboratory level, is the TCE that leads the market applied to photovoltaic devices due to its various advantages (R $\sim$ 10 - 15 Ω sq^{-1}, T $>$ 90 % and work function $\sim$ 4.8 eV). However, ITO presents limitations for which various alternatives have been explored. In this perspective, graphene has been considered as a strong option due to its various exceptional properties to address many of the ITO-related constraints in manufacturing electrodes for solar devices. Furthermore, despite obstacles in synthesis processes, graphene production can be cheaper and on a larger scale compared to ITO. Several investigations have been carried out on OSCs and PSCs where alternative hybrid anodes based on graphene and its derivatives have been incorporated. Among some reports are:

- Chen et al. [20] implemented a hybrid alternative anode in OSCs (glass/SU-8/Graphene/ PH1000/PEDOT:PSS/PCDTBT:PC71BM/Ag/Ca) and reached a PCE of $\sim$ 4.67 %. This anode was composed of a monolayer of graphene deposited by CVD with thermally induced wrinkles and a layer of PH1000 to enhance the surface roughness of the graphene. The hybrid anode showed T (at 550 nm) $\sim$ 89 % and R $\sim$ 148 Ω/sq.

- Fernández-Arteaga et al. [24] manufactured and implemented in OSCs (glass/SPG /PH1000/PEDOT:PSS/PBDB-T:ITIC/PFN/FM) an alternative bilayer anode (T (at 550 nm) $\sim$ 82 % and R $\sim$ 226 Ω/sq) based on a graphene derivative deposited by drop-casting and a layer of PH1000 to improve the morphology of the graphene material; in addition, a chemical treatment (hydroiodic acid) was used to reduce the oxygenated groups of the graphene derivative and a PCE of $\sim$ 4.2 % was achieved.

- Shin et al. [81] implemented a graphene-based hybrid electrode in flexible OSCs (PET/GR TCE/PEDOT:PSS/P3HT:PCBM/Al), achieving a PCE around 3.63 %. This anode was composed of a monolayer of graphene deposited by CVD, and doped with graphene quantum dots (GQDs)-mixed silver nanowires (AgNWs) with the aim of reducing the electrical resistance of graphene and improving its flexibility and performance of the device. The alternative anode reached T (at 550 nm) $\sim$ 90 % and R $\sim$ 594 Ω/sq.

- Zhang et al. [82] worked in an graphene anode for PSCs (FTO/SnO_2/Perovskite/ spiro-OMeTAD/Graphene) reaching a PCE $\sim$ 18.25 %. Graphene was deposited by spray coating and the device presented excellent flexibility and stability during exposure to humidity and heat. This anode achieved T (at 550 nm) $\sim$ 30 – 35 % and R $\sim$ 32 Ω/sq.

- Jeong et al. [83] manufactured an alternative graphene anode for flexible PSCs (PI/Cu-grid/Graphene/PEDOT:PSS/$FA_{0.8}MA_{0.2}Pb(I_{0.8}Br_{0.2})_3$/$PC_{61}BM$/ZnO/Ag) and they obtained a PCE $\sim$ 16.4 %. This anode is formed by a Cu-grid/graphene (GCEP) where graphene was deposited by CVD. The flexible PSCs presented good chemical and mechanical stability and GCEP improved the PSC photostability by blocking the ultraviolet (UV) and near-UV light. GCEP presented T (at 550 nm) $\sim$ 81 % and R $\sim$ 5.2 Ω/sq.

- Du et al. [84] implemented a graphene anode in OSCs (PET/BI-Graphene (3 layers)/ MoO_x/PPDT2FBT:$PC_{71}BM$/Ca/Al) which achieved a PCE $\sim$ 6.46 %. The three layers of graphene were deposited by CVD and doped with benzimidazole (BI). The OSCs showed excellent performance and the ability to scale the device. BI-Graphene (3 layers) anode showed T (at 550 nm) $\sim$ 92 % and R $\sim$ 208 Ω/sq.

These reports highlight the versatility of graphene as alternative electrodes in third generation PV devices such as OSCs and PSCs. Typically, these 2D materials are often synthesized and deposited expensively using methods such as CVD. In this work, unexpensivelly synthesized graphene derivatives were used in the low cost fabrication of electrodes (three-layer anodes and hybrid multilayer graphene anode). In the case of three-layer anodes, the graphene derivatives were deposited by drop-casting technique (easy to use and economical). The following chapters detail the electrode manufacturing processes, their implementation in OSCs, and the results of the electrode characterizations and their concept test in OSCs.

Chapter 4

Experimental section

4.1 Materials

Powder graphite (< 20 μm), natural flake graphite (< 320 μm), hydriodic acid (HI), DMSO, 1-chloronaphthalene and anhydrous chloroform were supplied by Sigma Aldrich. H_2SO_4 (98 wt %), $KMnO_4$ (99.5 wt %), HCl (37.3 wt %) and H_2O_2 (30.3 wt %) were purchased from Fermont (Productos Químicos Monterrey S.A. de C.V. PEDOT:PSS (PVP AI 4083 (semi-conductive) and PH1000 (conductive)) was acquired from Heraeus Clevios. Furthermore, Poly[(2,6-(4,8-bis(5-(2-ethylhexyl-3-fluoro)thiophen-2-yl)-benzo[1,2-b:4,5-b']dithiophene))-alt-(5,5-(1',3'-di-2-thienyl-5',7'-bis(2-ethylhexyl) benzo[1',2'-c:4',5'-c']dithiophene-4,8-dione)] (PBDB-T-2F (PM6) – MW = 126,690 g/mol) and 2,2'-((2Z,2'Z)-((12,13-bis(2-ethylhexyl)-3,9-diundecyl-12,13-dihydro-[1,2,5] thiadiazolo[3,4-e]thieno[2",3":4',5']thieno[2',3':4,5]pyrrolo[3,2-g]thieno[2',3':4,5] thieno[3,2-b]indole-2,10-diyl)bis(methanylylidene))bis(5,6-dichloro-3-oxo-2,3-dihydro-1H-indene-2,1-diylidene)) dimalononitrile (BTP – 4Cl (Y7) – MW = 1517.75 g/mol) were purchased from Ossila. The eutectic alloy Field's Metal (FM: Bi (32.5 %), In (51 %), Sn (16.5 %)) was purchased from Rotometals, ITO substrates ($\sim$ 10 Ω/sq) from Delta Technologies and glass substrates from Corning Incorporated. For the synthesis process of SPGSW and PGD, the water was purified through a Millipore system and reagents were used as received without further purification steps.

4.2 Synthesis of graphene derivatives

4.2.1 SPGSW

- **Exfoliation Method:**

  15 g of powder graphite (or flake graphite) was placed in a 2 L beaker, 1 L of distilled water was added. This suspension (15 mg/ mL) was treated at 8000 rpm for 60 min using a Ross high shear mixer. The solid was separated by gravity filtration and dried in an oven at 80 ^{o}C for 16 h.

- **Graphene Oxide (GO) synthesis:**

  For the preparation of oxidized graphene, 15 g of potassium permanganate ($KMnO_4$) was slowly added to 125 mL concentrated H_2SO_4 at 0 °C in 2 L double-layer beaker with a cooling system based on Cole-Parmer Polystat. Then 5 g exfoliated powder graphite (or flake graphite) was slowly added to this mixture in 30 minutes while was stirring. The temperature was increased to 36.5 °C and kept for 3 h. Subsequently, the obtained slurry was transferred to a 4 L beaker containing 1 L of distilled water and kept under magnetic stirring. The exothermic reaction raised the temperature of the mixture, then 20 mL of hydrogen peroxide at 30 wt % was slowly added. It is left in agitation for 10 min and then allowed to rest until precipitating the solid. It is decanted and 70 mL of concentrated HCl are added to the solid. It is left agitated for 15 min, and 1 L of distilled water is added, maintaining the magnetic agitation for 15 min more. Then, it is allowed to precipitate, it is decanted, and 4 L of water is added and stirred magnetically for 15 min. Subsequently, it was centrifuged at 4000 rpm for 20 min and washes were carried out until the pH is 7 (in total, there were 5 washes). Finally, the wet solid was frozen and freeze-dried for one week until dry GO was obtained.

- **Preparation of exfoliated graphite powder (GH) dispersions with GO:**

  1 g and 50 mg of exfoliated graphite powder and GO, respectively at 20:1 w/w were placed in 100 mL of distilled water. The mixture was tip sonicated for 30 min using an Ultrasonic processor Cole-Parmer Model CPX130PB. To favour the suspension of

graphene in water, GO was used as a surfactant. The resulting graphene suspension, in distilled water, was named SPGSW (solution-processed graphene suspended in water).

4.2.2 PGD

- **Exfoliation method**

  Graphene nanoplatelets are obtained by delamination treatment of aqueous graphite suspensions by high shear mixing. A 15 mg/mL flake graphite suspension in deionized water was treated during 60 min at 8000 rpm using a Ross high shear mixer with external cooling to maintain the internal temperature of the suspension at 25 °C.

- **GO synthesis**

  375 mL of H_2SO_4 are added to a jacketed reactor of 2 L capacity with recirculation of an ethylene glycol:water mixture (50:50) at 0 °C through the jacket. After the sulfuric acid reaches that temperature, 45 g of $KMnO_4$ is slowly added. This mixture reaches an emerald green color to which 15 g of flake graphite previously exfoliated at 8000 rpm for 1 h is slowly added. After obtaining a homogeneous mixture, the temperature is raised to 36.5 °C and kept under mechanical stirring for 3 h. Subsequently, this reaction mixture is transferred to a flask containing 1 L of distilled water. After 15 minutes, 30 mL of H_2O_2 (30 %) is added in order to stop the oxidation reaction. 3 L of distilled water is added and once all the solid precipitates, it is decanted and 200 mL concentrated HCl and 2 L of distilled water are added to eliminate the manganese salts. After 15 minutes of stirring, it is allowed to precipitate and the solid is decanted again and washed repeatedly with distilled water until a pH of 7 is reached.

- **Preparation of the dispersion**

  50 mg of GO was added to 100 mL of a 10 mg/mL dispersion of exfoliated flake graphite in distilled water. The suspension was treated with a tip of a sonotrode Cole-Parmer CPX130PB by immersion at an intensity of 60 % for 30 min. GO was used as a stabilizing agent to promote the suspension of graphene in water. The resulting suspension was called PGD (processable graphene derivative).

4.3 Anodes fabrication process

4.3.1 Three-layer graphene anode (TLGA)

The general configuration of the alternative TLGA was glass/SPGSW or PGD/PH1000 /PH1000 (SPGSW and PGD are in films). The chemical structure of SPGSW, PGD and the conducting polymer PEDOT:PSS (PH1000) are shown in figure 4.1. The glass substrates (SiO_2) were previously cut ($\sim$ 1.5 cm $\times$ 1.5 cm). For the TLGA based on SPGSW, the glass substrates were ultrasonically cleaned for 15 min, consecutively, with soap solution, distilled water, acetone, ethanol, and isopropyl alcohol. Then, substrates were dried overnight in an oven at 80 °C. After that, the UV-ozone plasma treatment was applied to the clean substrates for 15 min. For the TLGA based on PGD, the glass substrates were ultrasonically cleaned for 10 min, consecutively, with soap solution, ethanol, isopropyl alcohol, and deionized water; then, substrates were dried with air compress, and immediately they were treated with UV-ozone plasma for 15 min.

After the corresponding cleaning processes of the glass substrates, the SPGSW and PGD suspensions (40 μL) were deposited by drop-casting on the surface of the glass substrates at 40 °C for 40 min under regular atmosphere conditions. Subsequently, the SPGSW and PGD (films) were treated with HI at 90 °C for 2 h and dried overnight; this treatment was applied to reduce the oxygenated groups presented in the films and recover -their electrical properties. Then, UV-ozone plasma treatment was applied to the SPGSW and PGD for 1 min and 2 min, respectively, to functionalize only the surface of both films and improve the adhesion of the PH1000 layer. Previously, PH1000 was mixed with ethanol and DMSO at 1:1:0.1 v/v/v and stirred on a plate with magnetic stirring for about 48 h at room temperature. Then, 100 μL of the modified PH1000 solution was used to deposit the two PH1000 films; both films were deposited by spin-coating at 3000 rpm for 1 min with annealing treatment at 120 °C for 10 min. The final thickness for both electrodes were $\sim$ 96 nm and $\sim$ 106 nm for TLGA based on SPGSW and PGD, respectively.

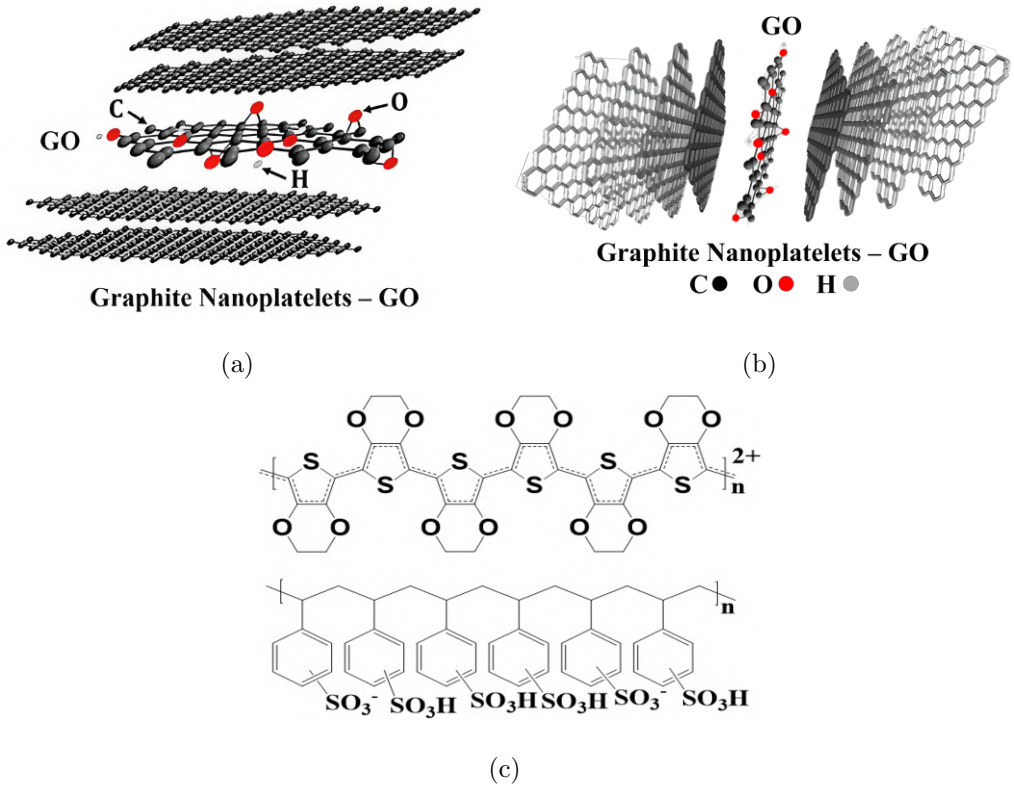

Figure 4-1: Chemical structures: (a) SPGSW, (b) PGD and (c) PEDOT:PSS (PVP AI 4083 (semi-conductive) and PH1000 (conductive)).

4.3.2 Hybrid multilayer graphene anode (HMGA)

The configuration of HMGA was glass/PH1000:PGD (4:1 v/v) – 6 layers. The PH1000 solution was the same one used in the manufacture of the TLGAs. Also, the cleaning process for the glass substrates was the same as that described for the TLGA based on PGD. For HMGA, the PH1000 solution was mixed with PGD (PH1000:PGD) at a ratio of 4:1 v/v and stirred magnetically on a plate for 12 h at room temperature. Then, 150 μL of the PH1000:PGD solution was taken to deposit one layer at a time by sping-coating over glass substrate at 3000 rpm for 1 min and each layer was dried at 120 °C for 10 min. Subsequently, PH1000:PGD anode was treated with HI at 90 °C for 2 h, this treatment was applied with the aim to reduce the oxygenated groups presented in the films and improve the electrical properties of the alternative graphene anode. After this process, anode was cleaned twice

with isopropyl alcohol by spin-coating (dynamic mode) at 2000 rpm for 30 s, and substrates were dried overnight at temperature room. The final thickness of the HMGA was $\sim$ 170 nm.

4.4 PM6:Y7-based OSCs fabrication process

TLGA based on PGD and HMGA were tested in PM6:Y7-based OSCs with configuration anode/PEDOT:PSS/PM6:Y7/PFN/FM, where PEDOT:PSS is the hole transport layer (HTL), PFN is the electron transport layer (ETL) and FM is Field's Metal (cathode) that is eutectic alloy of Bi (32.5 %), In (51 %) and Sn (16.5 %). In figure 4-2, chemical structures of PM6, Y7 and PFN are shown and the chemical structure of PEDOT:PSS is shown in figure 4-1. The ITO was used like reference anode, and it was cut ($\sim$ 1.5 $\times$ 1.5 cm), ultrasonically washed and treated with UV-ozone plasma just as glass substrates explained above for TLGA based on PGD. It is important to mention that the process used for deposit each layer of the OSCs was the same for the anodes (ITO, TLGA and HMGA) under regular atmosphere conditions. Previously, the active layer solution, PM6:Y7 (1:1.2 w/w), was prepared at a concentration of 16 mg/mL in anhydrous chloroform; the mixture was stirred magnetically at 80 ℃ for 2 h. PFN solution was prepared at a concentration of 0.3 mg/mL dissolved in anhydrous methanol and 0.2 % of acetic acid (99.8:0.2 v/v) and stirred magnetically for 24 h. Both solutions, PM6:Y7 and PFN, were stirred out of glovebox. PEDOT:PSS (HTL) was deposited by spin-coating over anodes at 4500 rpm for 1 min ($\sim$ 40 nm of thickness) with a thermal annealing at 120 ℃ for 15 min in a hot plate. Subsequently the active layer PM6:Y7 was deposited by spin-coating on top of PEDOT:PSS films at 2500 rpm for 1 min (thickness: $\sim$ 100 nm). Continuously, the PFN was also deposited by spin-coating on the active layer surface at 6000 rpm for 1 min (thickness in the range of 5 – 10 nm). No annealing treatments were applied to both layers, PM6:Y7 and PFN. The active area of the cells ($\sim$ 0.07 cm^2) were delimited using a shadow mask. Finally, FM was melted at 95 ℃ and deposited by drop-casting with a micropipette (50 μL) onto the active cell area of the preheated devices at the same temperature of FM.

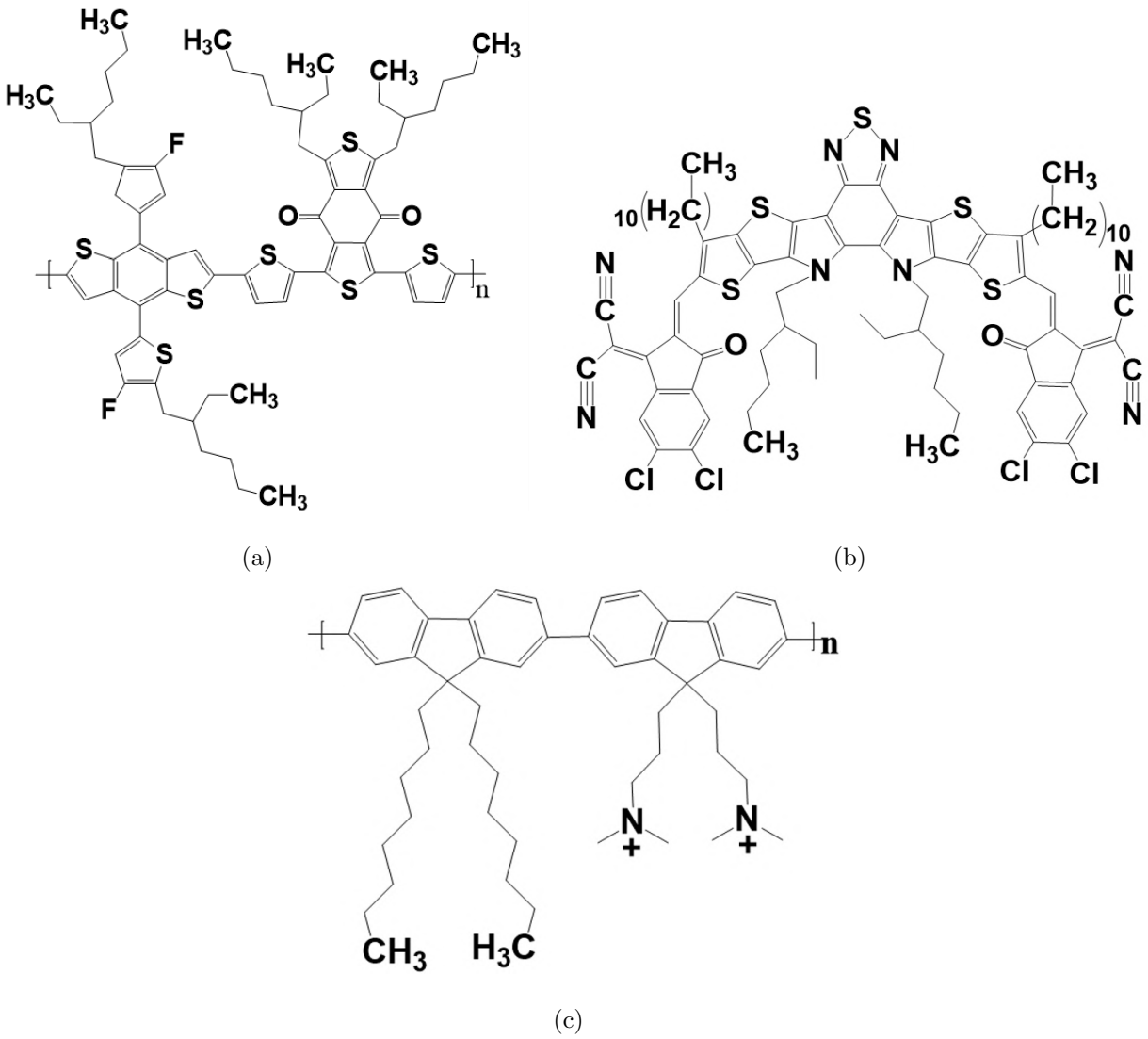

Figure 4-2: Chemical structures: (a) PM6, (b) Y7 and (c) PFN.

4.5 Equipment used for characterization

The chemical/structural features of SPGSW, PGD and HMGA were determined by Raman spectroscopy (Microraman Witec confocal, $\lambda = 532$ nm, and a 100X microscope objective (AN = 0.9)) and X-ray diffraction analyzes (XRD) was carried out with a Bruker D8 Advance ECO diffractometer ($\lambda \approx 0.154$ nm).

The morphological analysis of the films and the electrodes were carried out by Optical microscopy (OM, Keyence VHX 5000), Atomic force microscopy (AFM, easyscan2 from Nanosurf) operating in contact mode and Field Emission Scanning Electron Microscopy (FE-SEM, Model JSM-F from Jeol).

The electrical and optical properties of films and electrodes were measured by a four-point home-made experimental setup (resistance by square) and a Perkin Elmer UV/Vis/NIR spectrophotometer, respectively.

The OSCs based on ITO, TLGA based on PGD and HMGA were characterized by solar simulator Sciencetech SS150 class AAA (AM 1.5 condition (100 mW/cm^2, 1 sun light)). The current density curve as a function of voltage (J-V plot) was acquired with a Keithley 2450 source-meter. The PV parameters: open circuit voltage (Voc), short circuit current (Jsc), fill factor (FF) and power conversion efficiency (PCE), were determined from the J-V plot.

Chapter 5

Results and discussions

5.1 Electrode characterizations

5.1.1 Raman spectra

Figure 5-1 shows the Raman spectra of SPGSW, PGD and HMGA (PH1000:PGD at 4:1 v/v - 6 layers) at 532 nm ($\sim$ 2.33 eV).

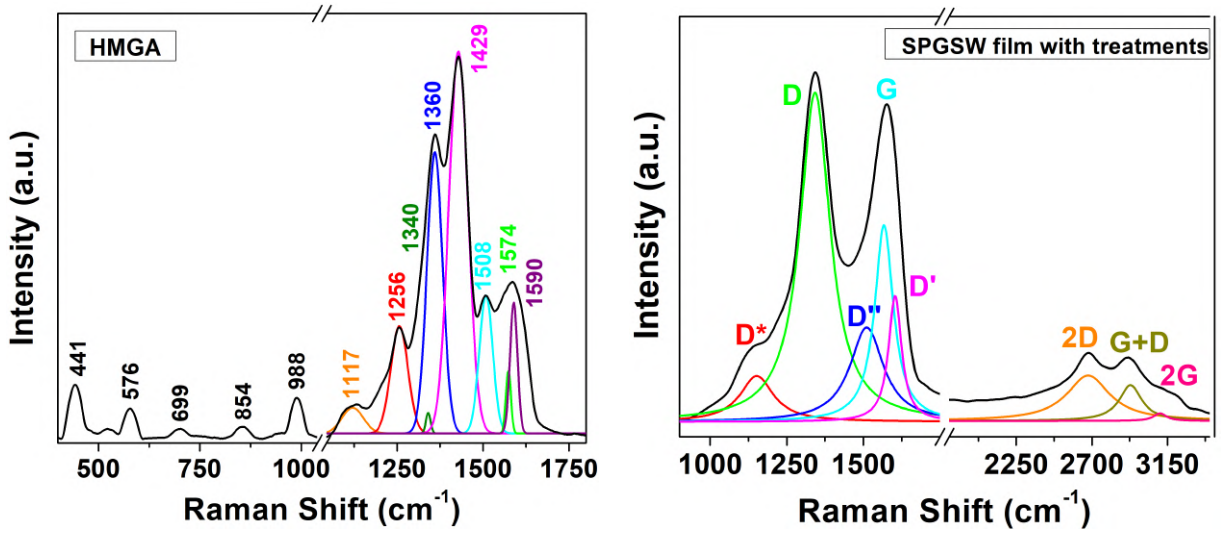

(a) (b)

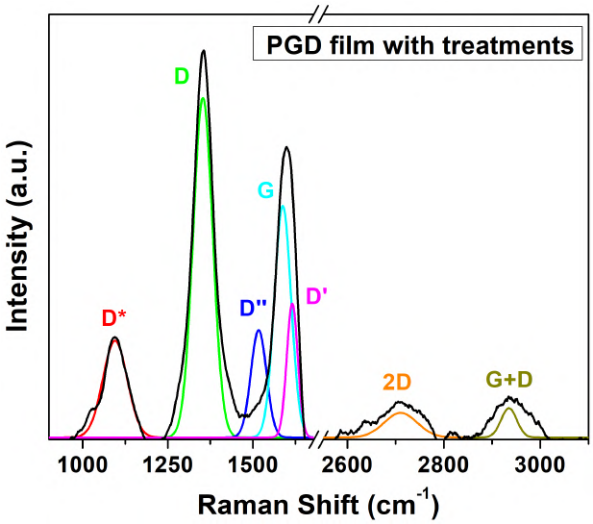

(c)

Figure 5-1: Raman spectra: (a) HMGA, (b) SPGSW and (c) PGD.

The Raman spectrum of figure 5-1a corresponds to the bulk heterojunction (BHJ) between PH1000 and PGD. The characteristic peaks of PH1000 are located at $\sim$ 441 cm^{-1}, $\sim$ 576 cm^{-1}, $\sim$ 699 cm^{-1}, $\sim$ 854 cm^{-1}, $\sim$ 988 cm^{-1}, $\sim$ 1117 cm^{-1}, $\sim$ 1256 cm^{-1}, $\sim$ 1360 cm^{-1}, $\sim$ 1429 cm^{-1}, $\sim$ 1508 cm^{-1} and $\sim$ 1574 cm^{-1}, which coincide with other reports in the literature [85, 86]. On the other hand, the peaks located at $\sim$ 1340 cm^{-1} and $\sim$ 1594 cm^{-1} correspond to the D and G bands, respectively. This corroborates the presence of PGD in the BHJ films.

The Raman spectra of figures 5-1b and 5-1c corresponds to SPGSW and PGD films, respectively. These figures present two characteristic zones: (1) first order bands (D, G, D*, D", D') are observed in the range from 1100 cm^{-1} to 1700 cm^{-1} and (2) second order bands (2D, D+G, 2G) observed in the range of 2500 cm^{-1} to 3200 cm^{-1}.

The D band ($\sim$ 1330 cm^{-1} - 1350 cm^{-1}) is related to defects in the graphene material and occurs due to intervalley processes [87]; D-band peaks for SPGSW and PGD were centered at $\sim$ 1342 cm^{-1} and $\sim$ 1353 cm^{-1}, respectively; located within of the range reported in the literature.

The G band ($\sim$ 1581 cm^{-1} - 1587 cm^{-1}) is related to C=C bond stretching and strain effects in carbon materials [88]; the G-band peaks for SPGSW and PGD were centered at $\sim$ 1567 cm^{-1} and $\sim$ 1588 cm^{-1}, respectively. The SPGSW presents a redshift of the G band, which indicates the recovery of the hexagonal network of carbon atoms with defects; on the other hand, PGD presents the G band with a slight blueshift, which indicates lattice distortions and a large number of defects caused by the oxidation process [89]. Also, it is important to mention that in graphene materials, the G band can present a redshift or blueshift due to the application of external stress, which would cause a deformation of the network, that is, a change in the interatomic distances and a redistribution of electronic charge [89]. In the literature there are several works that have reported the G band of graphene materials with a redshift [90, 91] or blueshift [88, 92].

The degree of defects or the graphitic film quality is determined by the ratio between the D and G band intensities (I_D/I_G) [93–96]. In general, highly-ordered graphitic samples (few defects) show low I_D/I_G values [97], as in the case of graphite (I_D/I_G = 0.01 - 0.24) [88, 96] or graphene (I_D/I_G = 0.21) [90]. On the other hand, a high I_D/I_G ratio indicates a high level of defects in the graphitic sample structure [97], as in the case of GO (I_D/I_G = 1.05 - 1.76) [93,98]. I_D/I_G values of 1.43 and 1.35 were achieved for SPGSW and PGD, respectively. This indicates that both samples have a high degree of defects, which correlates with the G band shift explained above. On the other hand, the size of the crystallite along the plane (L_a) can be calculated using equation 5-1 [99], where E_λ is the laser excitation energy in eV, I_D and I_G are the intensities of the D and G peaks, respectively. L_a is directly proportional to $\left(\frac{I_D}{I_G}\right)^{-1}$ for larger crystallites (L_a > 2 nm), while for smaller crystallites, (L_a < 2 nm), the linear relation breaks down, and I_D/I_G varies quadratically with crystallite size. For our samples, a L_a of $\sim$ 13 nm and $\sim$ 12 nm were calculated for the SPGSW and PGD, respectively. These calculated L_a are smaller than those reported in [94, 99]. Within the linear regime, this means that the size of the crystallite gives information about the defects of the graphene material, that is, a small L_a indicates greater defects and a large L_a indicates fewer defects. Based on the above, the crystallite sizes calculated for the SPGSW and PGD corroborate that these graphene samples have high degrees of defects, an observation that correlates with

the G band shift of both samples.

$$L_a = \frac{560}{E_\lambda{}^4} \left(\frac{I_D}{I_G}\right)^{-1} \tag{5-1}$$

The D' band ($\sim$ 1610 cm^{-1} - 1620 cm^{-1}) is associated with the impurity-induced intervalley dispersion process [87]; the peaks for SPGSW and PGD were centered at $\sim$ 1603 cm^{-1} and $\sim$ 1616 cm^{-1}, respectively. The $I_{D'}/I_G$ ratios for SPGSW and PGD were $\sim$ 0.77 and $\sim$ 0.69, respectively; which are quite high values compared to another previously reported ($I_{D'}/I_G \sim$ 0.12 - 0.23) [90,100]. The increase in the $I_{D'}/I_G$ ratio indicates a greater number of defects at the edges of the crystal structure (these types of defects are known as edge states) [100]. The values of the $I_{D'}/I_G$ ratio for SPGSW and PGD corroborated, once again, that both samples have defects in their structure and this correlates with the shift of the G band of both films, as well as with the results of the I_D/I_G ratio and the crystallite sizes calculated above.

The D* band ($\sim$ 1050 cm^{-1} - 1200 cm^{-1}) originates from the sp^3 orbital, it can be related to disorders in the graphitic lattice [87, 101], and the D" band ($\sim$ 1500 cm^{-1} - 1550 cm^{-1}) is related to the amorphous phases of the material [87]. The D* and D" band peaks for the SPGSW and PGD were centered at $\sim$ 1151 cm^{-1} and $\sim$ 1512 cm^{-1}; and $\sim$ 1095 cm^{-1} and $\sim$ 1517 cm^{-1}, respectively; these are located within of the range reported in the literature.

On the other hand, the 2D band ($\sim$ 2700 cm^{-1}) provides information on the number of layers present in the graphene samples. This band arises from the activation of two phonons with similar momentum and does not require the presence of defects in the material, that is, it is always present [88, 102]. The 2D-band peaks for SPGSW and PGD were centered at $\sim$ 2680 cm^{-1} and $\sim$ 2711 cm^{-1}, respectively. There are three ways to analyze the peak of the 2D band: (1) regarding its shape (broad or sharp) [93, 103]; in our spectra, the 2D band has a wide shape, which would indicate a multilayer structure. (2) FWHM of $\sim$ 329 cm^{-1} and $\sim$ 81 cm^{-1} were calculated for SPGSW and PGD, respectively; which corroborates, quantitatively, the multilayer structure of both graphene samples (monolayer if FWHM $\leq$ 30 cm^{-1} and multilayer if FWHM $>$ 30 cm^{-1}) [104]. (3) The I_{2D}/I_G ratio obtained were $\sim$ 0.52 and $\sim$ 0.33 for SPGSW and PGD, respectively; which agrees, once again, the multilayer structure of

the graphene samples (monolayer if $I_{2D}/I_G \geq 2$, and multilayer if $I_{2D}/I_G \leq 0.85$, [93, 97, 105]. According to what is stated in reference [106], an I_{2D}/I_G ratio around 0.5 usually indicates $\sim$ 7 layers of graphene, for the case of the SPGSW a quantity close to 7 layers could be estimated, while in the case of the PGD, given that the I_{2D}/I_G ratio is less than 0.5, it could indicate that there are more than 7 layers.

The D+G band ($\sim$ 2940 cm^{-1}) is an overtone of the D and G peaks positions and the 2G band ($\sim$ 3170 cm^{-1}) is attributed to the G band [107]; the D+G and 2G band peaks for the SPGSW and PGD were centered at $\sim$ 2929 cm^{-1} and $\sim$ 3106 cm^{-1}; and $\sim$ 2935 cm^{-1} and the 2G band was not presented, respectively.

5.1.2 XRD spectra

Figure 5-2 shows the XRD patterns of the graphite powder, SPGSW powder, PGD powder, PGD film and HMGA. Table 5-1 summarizes the characteristic planes of each sample. The crystal plane (001) was observed in SPGSW powder, PGD powder and PGD film; which indicates the presence of GO (low quantities) in the samples [90, 108]. GO was used as a surfactant to facilitate the suspension of the graphene materials in water. The crystal plane (002) of SPGSW powder and PGD powder practically matches that of graphite powder; these results corroborate that both samples are graphitic materials. However, for the PGD film, the plane (002) presents a notable shift to the left, which is in agreement with other reports of graphene derivatives: 26.4° - 26.5° [24, 90, 98]; also, this indicates that the PGD film has a greater amount of oxygenated groups [98, 109]. On the other hand, HMGA presents a peak located at 26.64°, which corresponds to the crystalline plane (002) characteristic of graphitic materials and corroborates the presence of PGD in the BHJ of HMGA.

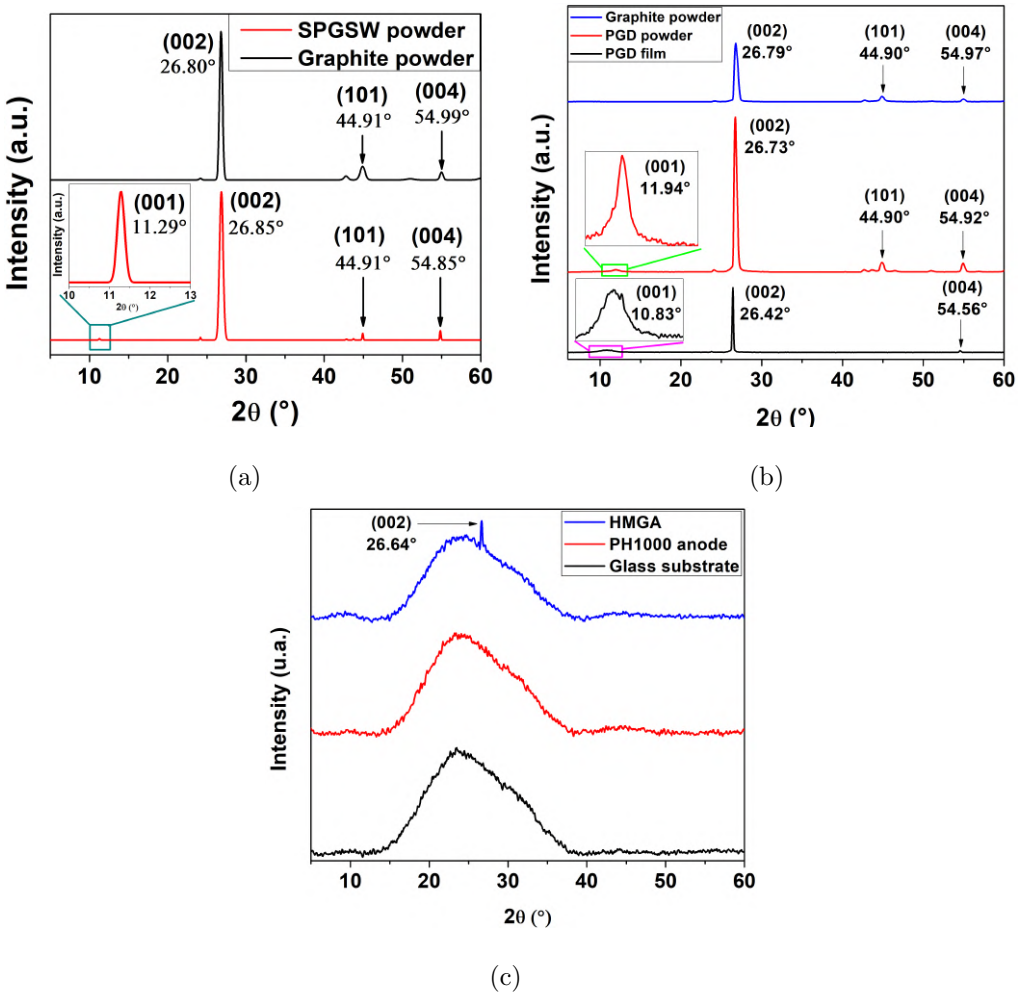

Figure 5-2: XRD spectra of samples: (a) SPGSW, (b) PGD and (c) HMGA.

Table 5-1: Crystal planes fo graphite powder, SPGSW powder, PGD powder, PGD film and HMGA.

	Crystal planes			
Samples	**(001)**	**(002)**	**(101)**	**(004)**
Graphite powder	—	26.80°	44.91°	54.99°
SPGSW powder	11.29°	26.85°	44.91°	54.85°
PGD powder	11.94°	26.73°	44.90°	54.92°
PGD film	10.83°	26.42°	—	54.56°
HMGA	—	26.64°	—	—

On the other hand, the (002) plane peak is used to calculate the interlayer spacing ($d_{(002)}$) by Bragg's law and the average crystallite size perpendicular to the plane (L_c) in the graphene lattice by Scherrer's equation [91, 99, 103]. Furthermore, through the ratio of L_c and $d_{(002)}$ (Equation 5-2), the number of layers along the c-axis (N_c) of the samples can be estimated [99, 103]. Table 5-2 summarizes these parameters.

$$N_c = \frac{L_c}{d_{(002)}} \tag{5-2}$$

Table 5-2: $d_{(002)}$, L_c and N_c calculations.

Samples	$\mathbf{d_{(002)}}$	$\mathbf{L_c}$	$\mathbf{N_c}$
Graphite powder	$\sim$ 0.331 nm	$\sim$ 18 nm	$\sim$ 54 sheets
SPGSW powder	$\sim$ 0.332 nm	$\sim$ 15 nm	$\sim$ 45 sheets
PGD powder	$\sim$ 0.333 nm	$\sim$ 28 nm	$\sim$ 84 sheets
PGD film	$\sim$ 0.337 nm	$\sim$ 53 nm	$\sim$ 157 sheets

These results have been previously reported for different commercial graphenes ($d_{(002)} \sim$ 0.333 nm – 0.334 nm, $L_c \sim$ 24.96 nm – 34.14 nm and $N_c \sim$ 75 – 102 layers) [91], graphene nanoplatelets ($d_{(002)} \sim$ 0.335 nm, $L_c \sim$ 14.42 nm and $N_c \sim$ 43 layers) [103], and different graphite samples ($d_{(002)} \sim$ 0.334 nm – 0.335 nm, $L_c \sim$ 14.68 nm – 14.69 nm and $N_c \sim$ 44 layers) [110]. Thus, our estimations indicate that SPGSW powder, PGD powder and PGD film have a multilayer structure remembering that Nc, from the point of view of XRD, depends on the material crystallinity, the order degree, and the amount of oxygenated groups in the interlayers.

5.1.3 Optical microscopy (OM)

Figure 5-3 shows the topography of SPGSW with different treatments and the SPGSW-based TLGA (SPGSW/PH1000/PH1000) by OM. It shows that the glass substrate (5-3a) was adequately covered by the SPGSW without treatments (WT) (5-3b). Figure 5-3c corresponds

to the topography of SPGSW treated with HI, several black dots can be observed that could indicate defects in the graphene material film. Figure 5-3d corresponds to SPGSW treated with HI and UV-ozone plasma; certain black spots (defects) and light and dark areas can be seen in its topography. The light zones could be because there is less graphene content because plasma treatment removes some of the material. Figure 5-3e shows the topography of the SPGSW-based TLGA, the clusters and the light and dark areas that are usually present after the HI and plasma treatments (5-3d) are not observed, indicating that the PH1000 layers completely covered defects and improved the SPGSW homogeneity.

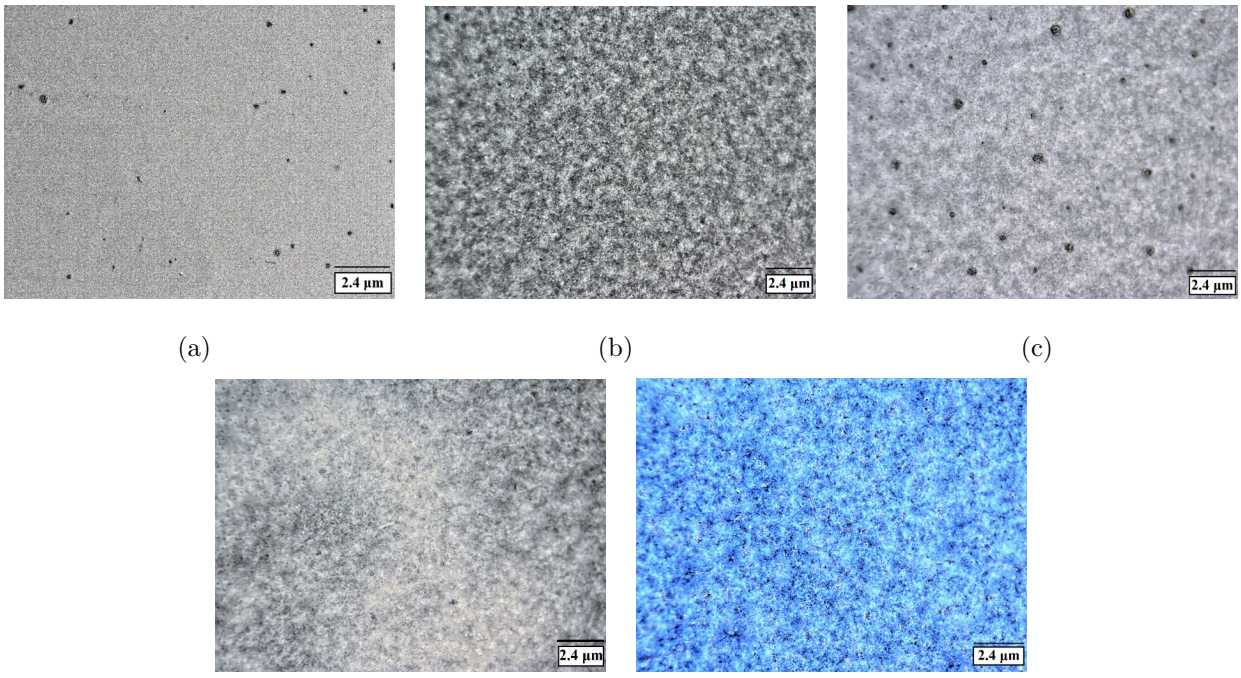

Figure 5-3: Topography by OM of: (a) glass substrate, (b) SPGSW/WT, (c) SPGSW+HI, (d) SPGSW+HI+UV-ozone plasma, and (e) SPGSW-based TLGA.

Figure 5-4 shows the topography by OM of the glass substrate (5-4a), PGD with treatments (HI and UV-ozone plasma) (5-4b), PGD-based TLGA (PGD/PH1000/PH1000) (5-4c), PH1000 anode (composed of 6 layers) (5-4d) and HMGA (5-4e). OM images confirmed that

the glass substrate was reasonably covered by the PGD, PH1000 and PH1000:PGD films. After HI and UV-ozone plasma treatments, PGD showed a more uniform topography, with some grains that appear to be part of the graphenic material. In the case of PGD-based TLGA, areas covered by PH1000 (blue) were observed to complement the regions where PGD (brown-orange) could not completely covered. This helped to improve the uniformity and conductivity of the electrode. PH1000 anode and HMGA images showed quite similar topography and acceptable uniformity.

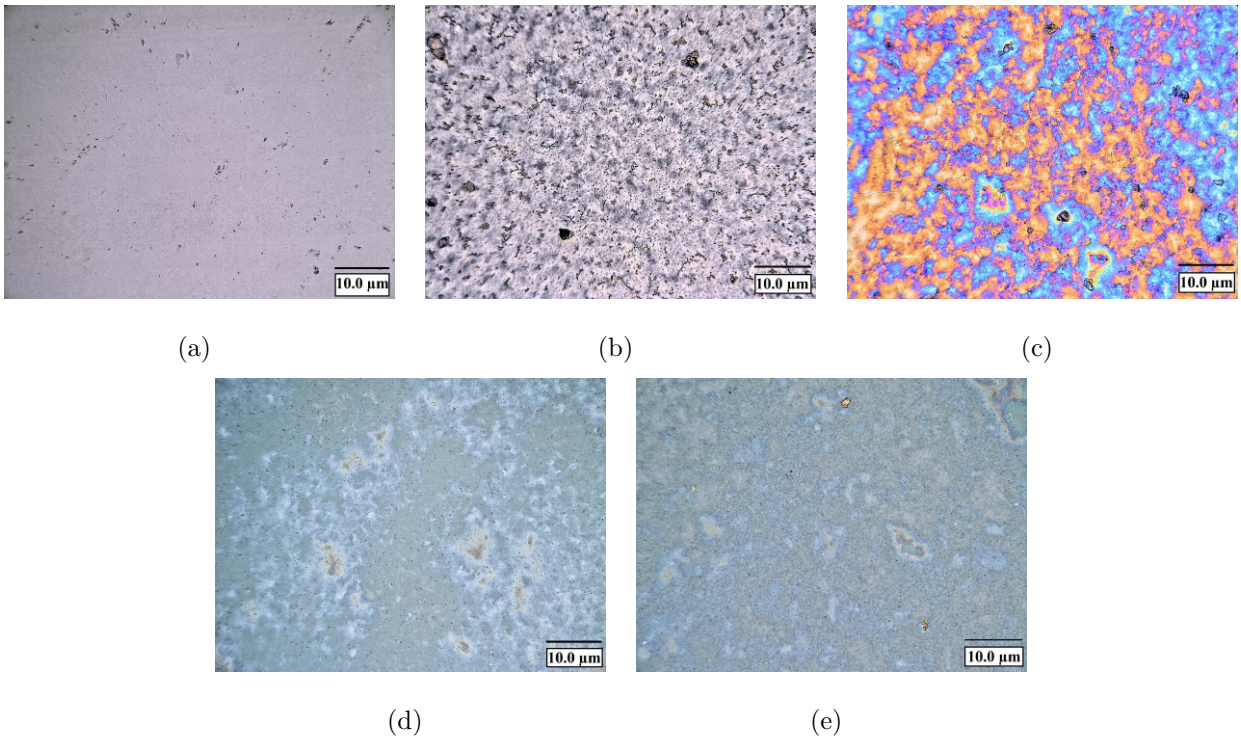

Figure 5-4: Topography by OM of: (a) glass substrate, (b) PGD with treatments, (c) PGD-based TLGA, (d) PH1000 anode, and (e) HMGA.

5.1.4 Atomic force microscopy (AFM)

AFM images shown in figure 5-5 reveals the morphology of SPGSW with and without treatments as well as that of SPGSW-based TLGA. AFM images confirmed that the glass substrate (5-5a) was covered with SPGSW. The SPGSW/WT (5-5b), SPGSW+HI (5-5c) and SPGSW+HI+UV-ozone plasma (5-5d) films presented roughness of $\sim$ 5 nm, $\sim$ 4 nm and $\sim$ 7

nm, respectively. These roughnesses show a significant decrease compared to that for SPG ($\sim$ 11 nm) which was also deposited by drop-casting [24]. However, when the plasma treatment was applied to the samples previously reduced by HI, the roughness increased slightly until $\sim$ 7 nm; this behavior may be because the plasma removes part of the deposited graphene material, leaving spaces that affect the morphology of the film. Furthermore, a significant contrast can also be observed between the roughness of the SPGSW films deposited by drop casting and the graphene film deposited by CVD (roughness $\sim$ 0.38 nm) [20]. Moreover, the roughness of the SPGSW films mentioned above is still high with respect to ITO ($\sim$ 1.85 nm) [20]. The fabrication of an electrode with homogeneous morphology and low roughness is also extremely important, as this would allow a better contact between the electrode and the other stacked layers of the photovoltaic device [24]. PH1000 polymer is a viable and simple option that could allow obtaining more homogeneous morphologies and mainly improving the electrical conductivity of SPGSW+HI+UV-ozone plasma. With the deposition of PH1000 layers, the roughness of the SPGSW-basedd TLGA was $\sim$ 6 nm (5-5f) with a total thickness of $\sim$ 96 nm. Each layer thickness of the alternative electrode was $\sim$ 5 nm, $\sim$ 45 nm and $\sim$ 46 nm for the SPGSW+HI+UV-ozone plasma (5-5e), first and second layers of PH1000, respectively.

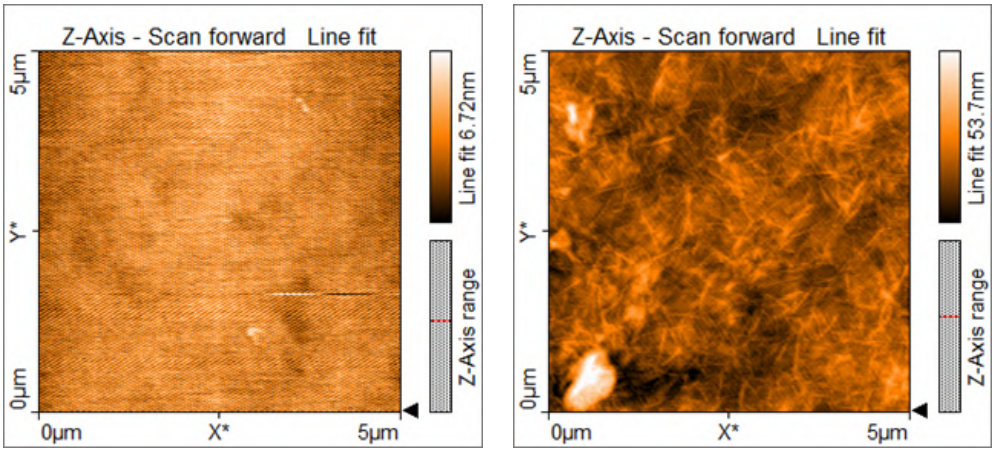

(a) (b)

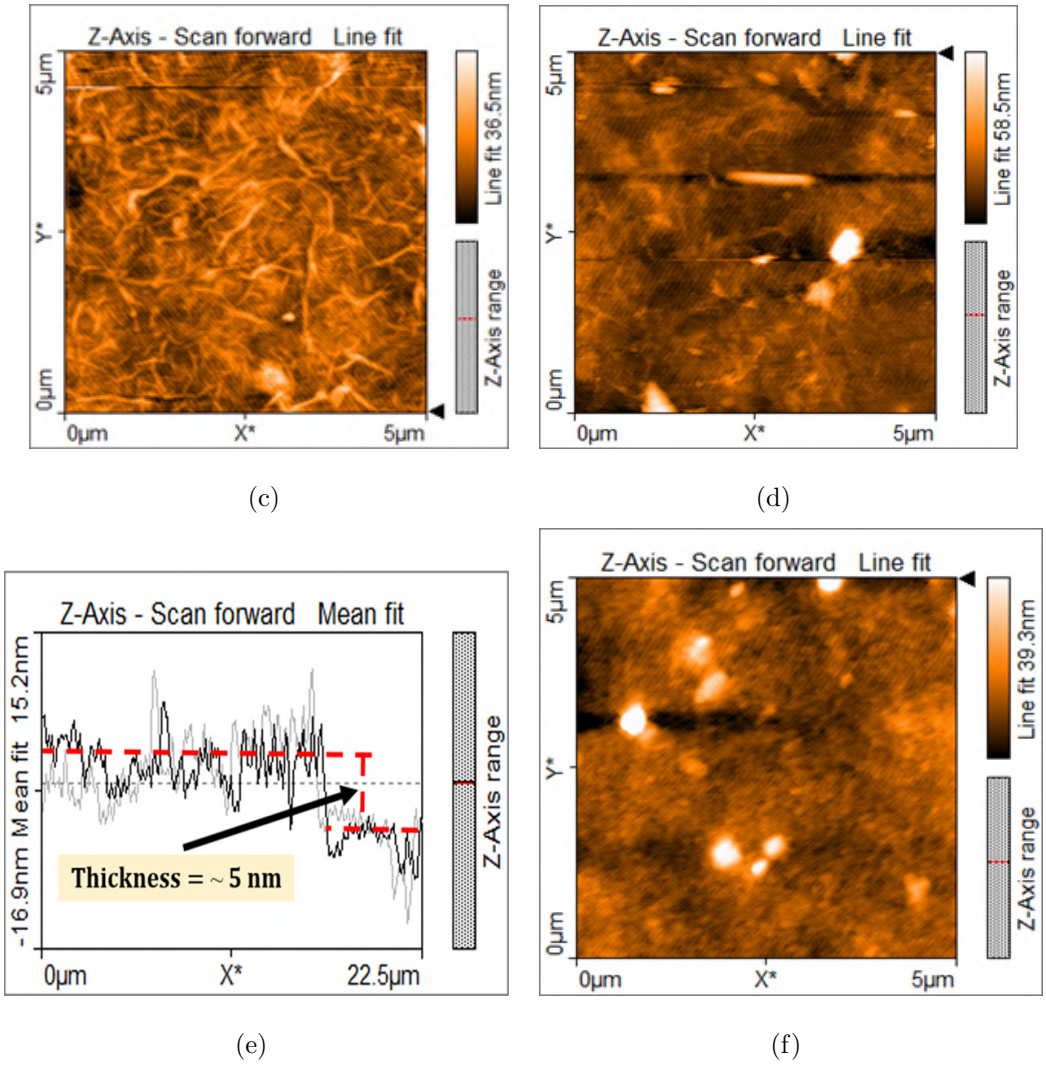

Figure 5-5: Morphology by AFM of: (a) glass substrate, (b) SPGSW/WT, (c) SPGSW+HI, (d) SPGSW+HI+UV-ozone plasma, (e) average thickness of SPGSW with treatments, and (f) SPGSW-based TLGA.

Figure 5-6 shows the morphological characterization by AFM of glass substrate (5-5a), PGD (5-5b), PGD-based TLGA (5-5c), PH1000 anode (6 layers) (5-5d) and HMGA (5-5e). AFM also confirmed that the glass substrate was covered by the layers of PGD and PGD:PH1000. The first layer of the PGD-based TLGA was PGD (treated with HI and UV-ozone plasma), in which the characteristic wrinkles of graphene materials can be observed. This layer reached an average roughness and thickness of $\sim$ 10 nm and $\sim$ 30 nm, respectively. The average roughness

and thickness of the PGD-based TLGA was ∼ 6 and ∼ 106 nm, respectively. On the other hand, the PH1000 anode and HMGA achieved average roughness of ∼ 5 nm and ∼ 7 nm, and average thickness of ∼ 200 nm and ∼ 170 nm, respectively. For PGD-based TLGA, PGD roughness (∼ 10 nm) is relatively high, thus, deposition of the PH1000 layers helped to reduce this roughness (∼ 6 nm), resulting in an electrode with a more homogeneous morphology that would allow better contact with the other device layers; PH1000 also contributes to the conductivity of the PGD-based TLGA. For the HMGA, there was a slight difference in roughness with respect to the PH1000 anode, which could be due to the presence of PGD grains (see Figure 5-4e) in HMGA films. Regarding the difference in thickness between the PH1000 anode and HMGA, this could be to the graphene material suspension in distilled water, which allows a greater dilution of the PH1000 solution, which helps to reduce the thickness of the HMGA films. When comparing PGD-based TLGA and HMGA thicknesses with ITO (170 – 200 nm, information given by the manufacturer), it is observed that the reached results are acceptable.

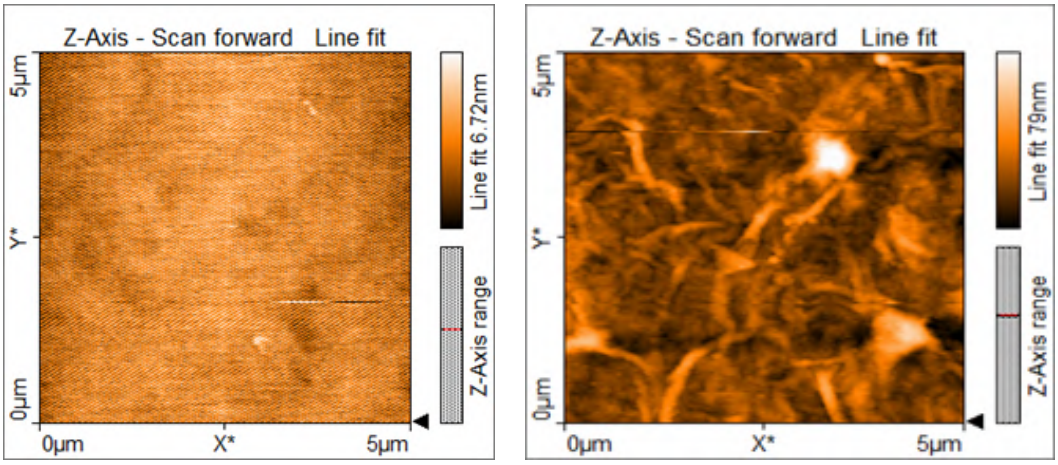

(a) (b)

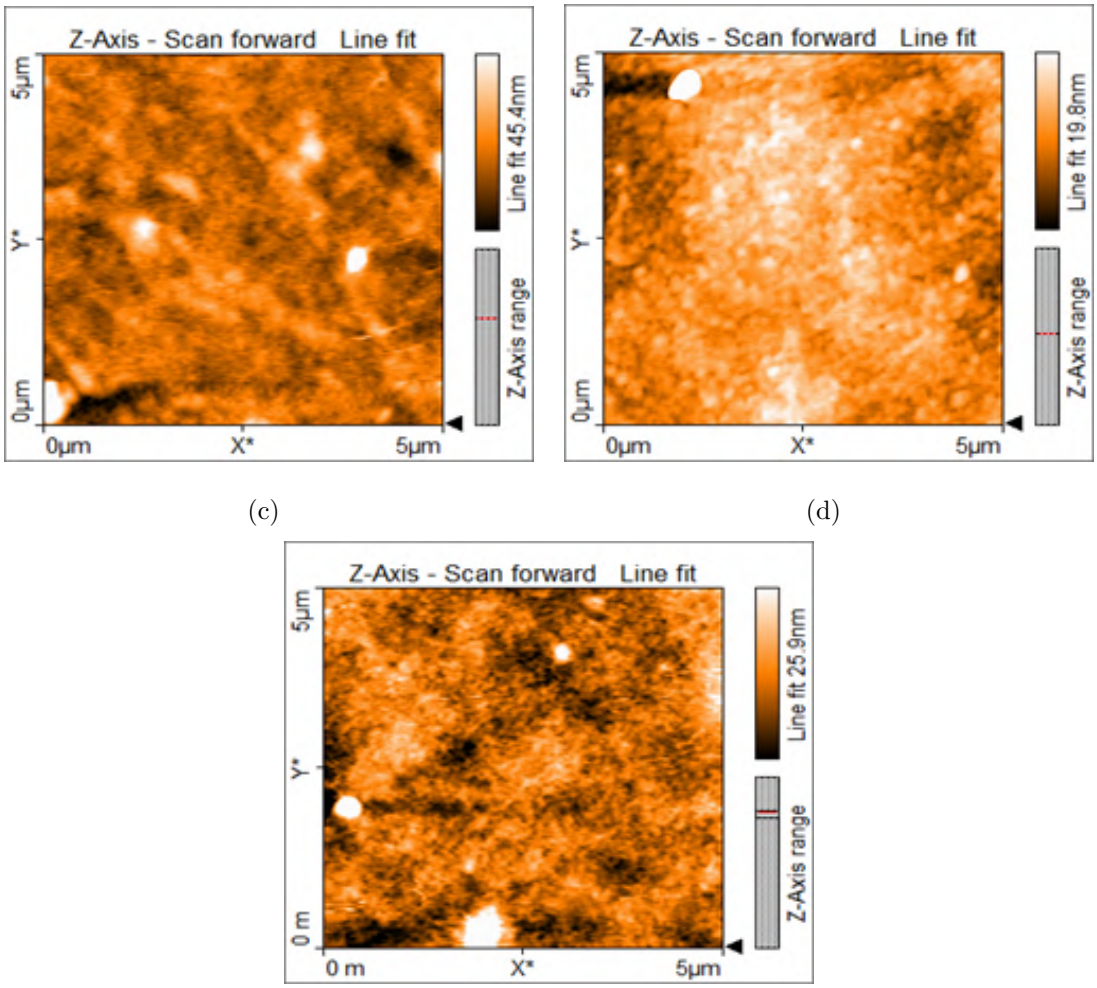

Figure 5-6: Morphology by AFM of: (a) glass substrate, (b) PGD with treatments, (c) PGD-based TLGA, (d) PH1000 anode (6 layers), and (e) HMGA.

5.1.5 Field emission scanning electron microscopy (FESEM)

Figure 5-7 shows the morphological characterization by FESEM of SPGSW with and without treaments, PGD with treatments, PGD-based TLGA, PH1000 anode and HMGA. These images also corroborated the deposition of SPGSW, PGD, PH1000 and PH1000:PGD on the glass substrate. The images of SPGSW with and without treatments (Figures 5-7a - 5-7c) showed wrinkles, which is something characteristic of graphene materials [111, 112]. These

wrinkles were also observed by AFM (Figures 5-5b - 5-5d). The SPGSW film treated with HI (Figure 5-7b) showed certain pores that could be due to the ability of HI to remove the epoxy and hydroxyl functional groups found on the surface and edges of the graphene material [112]. Figure 5-7c corresponds to the SPGSW treated with HI and UV-ozone plasma and shows smoothing and reduction of wrinkles in the material morphology (verified by AFM in Figure 5-5d); likewise, it presents overlapping flakes with a non-uniform and apparently thick morphology. Similar to what was observed in the SPGSW, wrinkles were also observed on the surface of the PGD and exhibited a smoother appearance (Figure 5-7d), which was also corroborated by AMF (Figure 5-6b). The smoothing of wrinkles is caused by the UV-ozone plasma treatment. Fig. 5-7e corresponds to the PGD-based TLGA that presents a uniform morphology, and this is because the PH1000 layers adequately covered the PGD. This was also observed by AFM (Fig. 5-6c). In the case of the SPGSW-based TLGA, a similar morphology would also be expected. Figures 5-7f and 5-7g show the morphologies of the PH1000 anode and HMGA, respectively. Both images showed a quite similar morphology, and no significant differences are observed, which is also corroborated by the AFM images (Figures 5-6d and 5-6e). It is also possible to observe certain pores in the morphological images of both anodes, which may be due to the removal of the PSS chains in the PH1000 and functional groups (epoxy and hydroxyl) on the PGD by the HI treatment [113, 114].

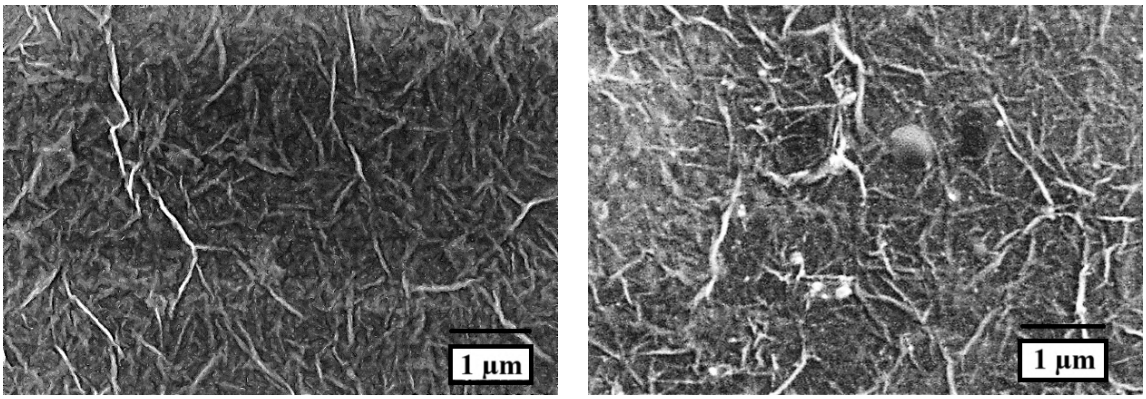

(a) (b)

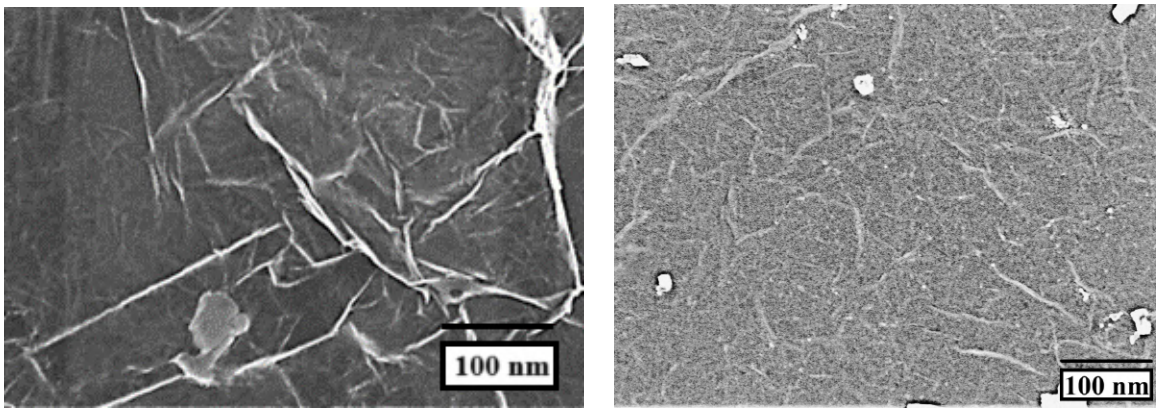

(c) (d)

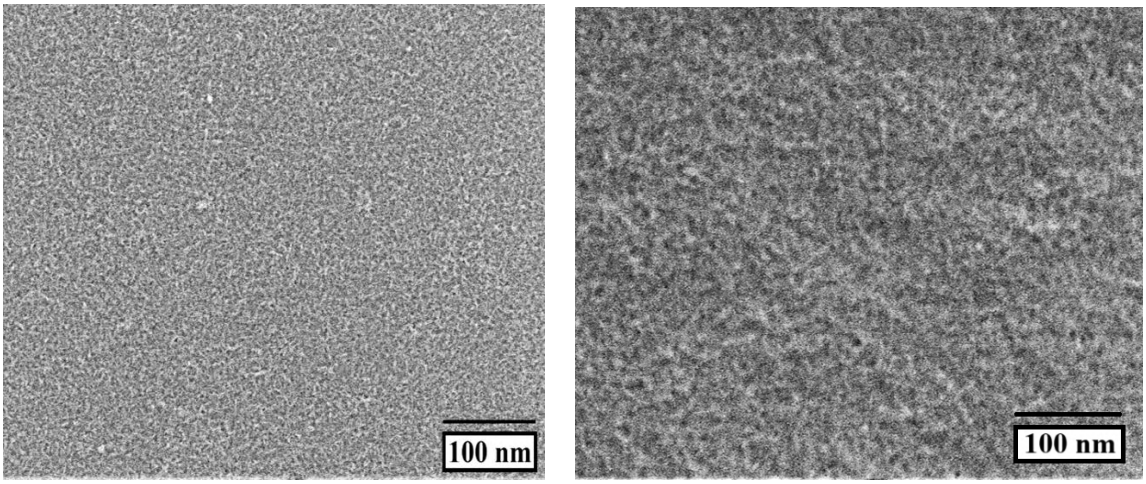

(e) (f)

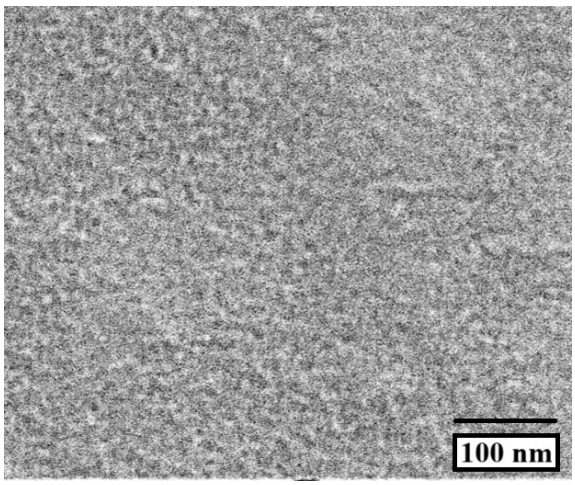

(g)

Figure 5-7: Morphology by FESEM of: (a) SPGSW/WT, (b) SPGSW+HI, (c) SPGSW+HI+UV-ozone plasma, (d) PGD with treatments, (e) PGD-based TLGA (f) PH1000 anode (6 layers) and (g) HMGA.

5.1.6 Optical and electrical properties

Figure 5-8 shows the UV-Vis transmittance spectra of SPGSW (with and without treatments), PH1000, and TLGA based on SPGSW (with and without plasma treatment). From figure 5-8a, transmittances of $\sim$ 94 %, $\sim$ 96 % and $\sim$ 86 % at 550 nm were determined for SPGSW/WT, SPGSW+HI and SPGSW+HI+UV-ozone plasma, respectively. From figure 5-8b, transmittances of $\sim$ 91 %, $\sim$ 85 % and $\sim$ 78 % at 550 nm were reached for the PH1000 (2 layers), TLGA based on SPGSW without UV-ozone plasma treatment and TLGA based on SPGSW with UV-ozone plasma treatment, respectively. Considering the experimental transmittance of the SPGSW+HI+UV-ozone plasma ($\sim$ 86 %) and considering that a graphene sheet absorbs $\sim$ 2.3 % of light in the Vis region [24], then, the sheets number of SPGSW+HI+UV-ozone plasma can be estimated theoretically: $\sim$ 6 graphene layers, which is very close to the determined value using Raman spectroscopy ($\sim$ 7 graphene layers). Both theoretical and experimental number of layers corroborate that the graphene film is multilayer. Besides, considering that the film SPGSW+HI+UV-ozone plasma (6 layers) has an absorbance of $\sim$ 14 % and PH1000 polymer (2 layers) an absorbance of $\sim$ 9 %, thus, the expected transmittance for the three-layer graphene electrode is $\sim$ 77 %, which is quite close to the experimentally measured (78 %).

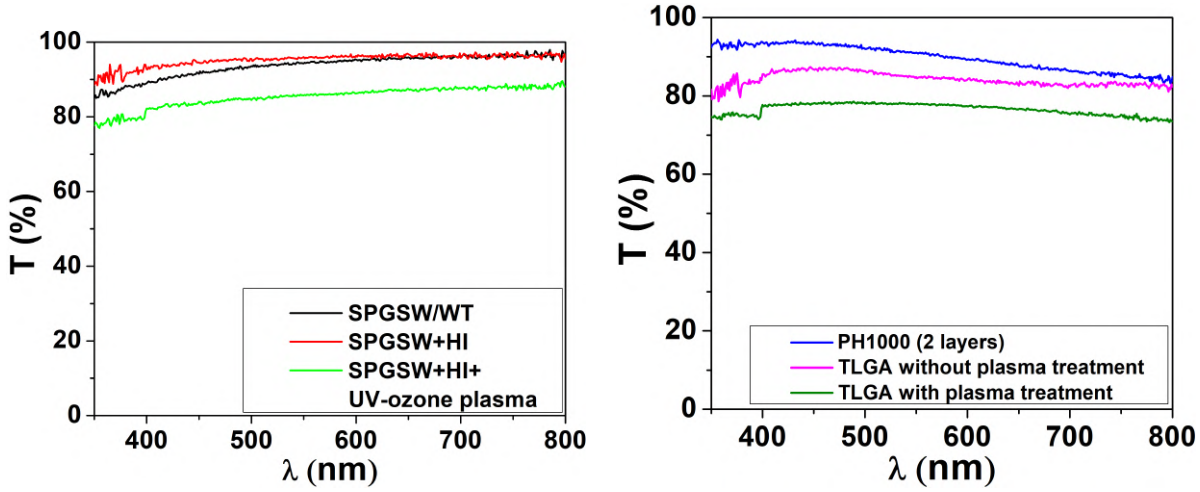

(a) (b)

Figure 5-8: Transmittance spectra: (a) SPGSW (with and without treatments), and (b) SPGSW-based TLGA (with and without UV-ozone plasma treatment). The films were deposited on glass substrates.

The electrical resistance of the SPGSW/WT film (initially in the MΩ order) decreased when the HI treatment was applied because it removed the oxygenated groups present in the graphene material due to GO; however, when the plasma treatment was applied, a certain amount of the graphene material was degraded, generating some defects, and slightly increasing the electrical resistance. Despite these treatments, the electrical resistance was still above the kΩ range. The average electrical resistances were 10^6 Ω/sq, ∼ 91 kΩ/sq, ∼ 168 kΩ/sq, ∼ 102 Ω/sq, ∼ 131 Ω/sq and ∼ 88 Ω/sq determined for SPGSW/WT, SPGSW+HI, SPGSW+HI+UV-ozone plasma, PH1000 (2 layers), TLGA based on SPGSW without UV-ozone plasma treatment and TLGA based on SPGSW with UV-ozone plasma treatment (electrode with the minimum electrical resistance in this work), respectively. Deposition of the two PH1000 layers contributed to a considerable decrease in the electrical resistance in the TLGA based on SPGSW with and without plasma treatment. As mentioned [24], the incorporation of PH1000 may indicate that defects present in SPGSW are covered, causing an improvement in the morphology and restoration of the electrical paths in the alternative electrode. On the other hand, UV-ozone plasma treatment also significantly reduced

the electrical resistance of the TLGA based on SPGSW compared to the TLGA based on SPGSW without UV-ozone treatment, although there was a $\sim$ 7 % decrease in transmittance, that could result by the exposure of dark areas after the plasma treatment (figure 5-3d). The decrease in electrical resistance could be explained by the fact that the UV-ozone plasma treatment incorporated oxygenated groups only on the surface of the SPGSW+HI, improving the film morphology and allowing better adhesion of the first PH1000 sheet to the SPGSW+HI after the plasma treatment. On the other hand, it is assumed that work function of the SPGSW+HI+UV-ozone plasma film is in the range of $\sim$ 4.4 eV to 4.9 eV, as has been reported for other graphene derivatives [20, 115–117]. This would indicate two facts: 1) the mentioned graphene film has a work function similar to ITO ($\sim$ 4.8 eV) [22] and 2) this TLGA based on SPGSW can adequately be an alternative to ITO in opto-electronic devices.

On the other hand, the optical and electrical properties of the PGD-based TLGA and HMGA electrodes were also studied. Figure 5-9 shows the transmittance curves of ITO ($\sim$ 88 %), PGD-based TLGA ($\sim$ 74 %), HMGA ($\sim$ 79 %) and PH1000 anode ($\sim$ 76 %). In TLGA, PGD film was treated with HI and UV-ozone plasma, and HMGA and PH1000 anode were treated with HI. The difference of 3 % between HMGA and PH1000 anode could be due to the fact that PGD is suspended in distilled water, which helps to dilute the PH1000 solution, allowing thinner films with higher transmittance. The average electrical resistance (measured just after manufacture) of the PGD-based TLGA, HMGA and PH1000 anode were $\sim$ 170 Ω/sq, $\sim$ 134 Ω/sq and $\sim$ 73 Ω/sq, respectively. To ITO, the electrical resistance is about 10 – 15 Ω/sq.

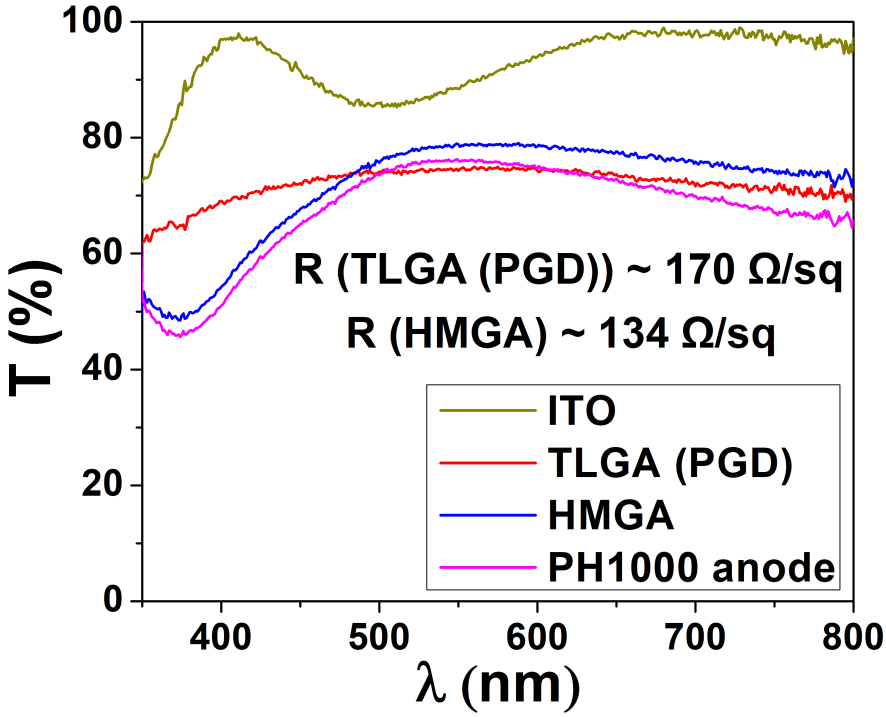

Figure 5-9: UV-Vis transmittance spectra of ITO, PGD-based TLGA, HMGA and PH1000 anode. Both anodes, HMGA and PH1000, have 6 layers. TLGA, HMGA and PH1000 films were deposited on glass substrates.

The transmittance and electrical resistance stability of PGD-based TLGA and HMGA were analyzed (figure 5-10) for 192 h under regular atmosphere conditions, temperature about 25 – 30 °C and humidity in the range 20 – 25 %.

For transmittance, this study showed that both alternative anodes PGD-based TLGA (figure 5-10a) and HMGA (figure 5-10b) maintained good stability under regular atmospheric conditions. A significant reduction in the transmittance of the PGD-based TLGA was observed, mainly due to the presence of the PGD film. Previous reports have shown that a graphene film absorbs $\sim$ 2.3 %. Through Raman spectroscopy analysis, it was determined that PGD film has more than 7 layers of graphene material, resulting in a light absorption of more than 16 %. On the other hand, the HMGA has a slightly higher transmittance than the PH1000. This is due to the dilution of the PH1000 solution by the suspension of the PGD, which reduces the thickness of the films and therefore increases the transmittance of the electrode.

The electrical resistance stability study of the PGD-based TLGA (Figure 5-10c) showed that this alternative anode presents a significant difference with respect to the PH1000 (2 layers). The PH1000 (2 layers) initially had an electrical resistance of $\sim$ 358 Ω/sq, which remained stable for the first 24 h. Subsequently, at 48 h, the electrical resistance decreased significantly to $\sim$ 295 Ω/sq. However, over the next 72 h, the electrical resistance gradually increased in the range of $\sim$ 316 – 328 Ω/sq. Then, at 144 h, the electrical resistance experienced a significant decrease and reached $\sim$ 232 Ω/sq. After 144 h, the electrical resistance began to gradually increase again. This behavior can be interpreted as a result of effective initial compaction of the PH1000 films during the first 48 h, which reduced the electrical resistance to $\sim$ 295 Ω/sq. However, over the next 72 h, the PH1000 films began to gradually degrade, resulting in an increase in electrical resistance. This cycle repeats after 144 h. On the other hand, the electrical resistance of the PGD-based TLGA remained fairly constant throughout the study period. This could suggest several important implications about the role of PGD in the electrode: (1) it could contribute to the reduction of the electrical resistance of the electrode, (2) it could play a role in slowing down the degradation of PH1000, which is reflected in the stability of the electrical parameter, and (3) it is possible that it favors better compaction between the PH1000 and PGD films.

Similarly, the electrical resistance stability study of the HMGA (figure 5-10d) showed that this alternative anode presents a significant difference with respect to the PH1000 anode. The PH1000 anode showed an initial electrical resistance of $\sim$ 70 Ω/sq, which gradually increased to $\sim$ 78 Ω/sq over the first 120 h. After this time, it presented a significant increase in electrical resistance, reaching approximately 100 Ω/sq. This constant increase in electrical resistance could be because the PH1000 presents a continuous degradation process; during the first 120 h its degradation is slow, while afterwards the degradation of PH1000 begins to accelerate. On the other hand, HMGA showed an initial electrical resistance $\sim$ 134 Ω/sq, which increases to $\sim$ 160 Ω/sq in the first 24 h, and this resistance remained stable during the next 48 h. After the first 72 h of the fabrication of the anode, the electrical resistance decreased, and it started to stabilize around $\sim$ 145 – 150 Ω/sq. The increase in the electrical resistance of the HMGA in the first 24 h could be due to an accelerated degradation process

of the PH1000. However, the decrease in the electrical resistance (after the first 72 h of anode manufacturing) could be attributed to the fact that the PGD is retarding the degradation of the PH1000 and allowing the films to compact better to stabilize the electrical resistance of the anode. These differences, that can be interpreted from the study of electrical resistance stability between the PH1000 and HMGA, show the significant impact that PGD has on the electrical stability of the anode over time.

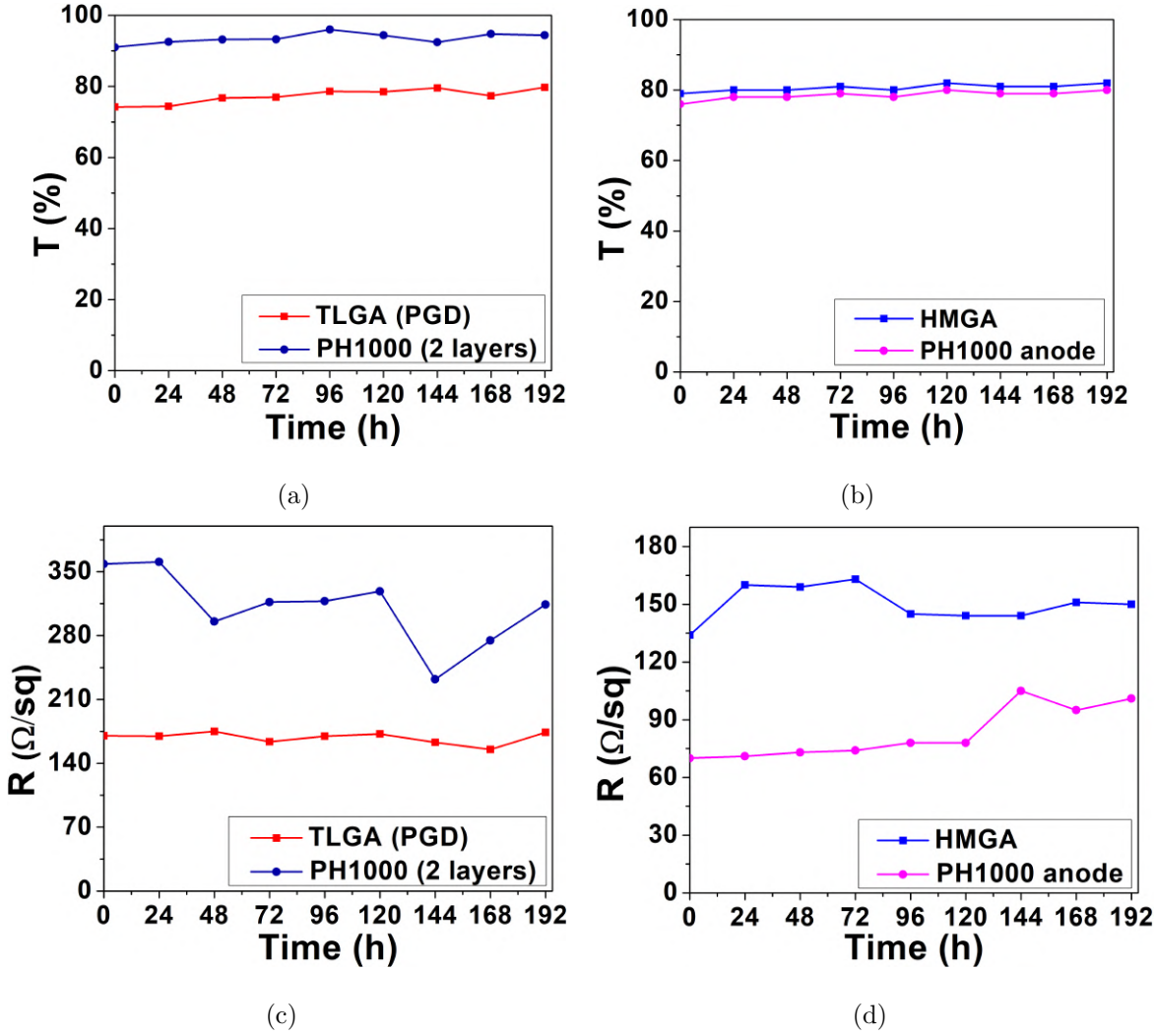

Figure 5-10: Transmittance and electrical resistance stability study of PGD-based TLGA (a and c) and HMGA (b and d).

Table 5-3 presents the comparison between previously reported graphene electrodes and ours: SPGSW-based TLGA, PGD-based TLGA and HMGA. The electrical resistance and transmittance values of these alternative anodes are very promising for their application in future photovoltaic devices. Furthermore, they demonstrate the effectiveness of deposition techniques, such as drop-casting and spin-coating, for the economical and efficient production of graphene electrodes. low-cost process.

Table 5-3: Comparison of the electrical resistance (R) and transmittance at 550 nm (T) parameters in alternative graphene electrodes with different deposition methods and our electrodes (TLGA based on SPGSW, TLGA based on PGD and HMGA). *Typically, ITO shows a T (at 550 nm) $\sim$ 90 % and R $<$ 20 Ω/sq [118].

Electrodes	**Deposition**	**R (Ω/sq)**	**T (%)**	**Ref.**
PH1000	Spin-coating	$\sim$ 219	$\sim$ 98	[20]
PH1000/Graphene (wrinkled)	CVD	$\sim$ 147	$\sim$ 88	[20]
Bilayer (SPG/PH1000)	Drop-casting	$\sim$ 226	$\sim$ 82	[24]
Graphene/PES	PATCVD	$\sim$ 82	$\sim$ 86	[115]
PI@Graphene	CVD	$\sim$ 83	$\sim$ 92	[116]
Cu (7 nm thick)/ Graphene (4 layers)	CVD	$\sim$ 75	$\sim$ 92	[117]
graphene-AgNWs/PET (Commercial)	Spray-coating	$\sim$ 129 - 194	$\sim$ 70	[119]

Few-layer graphene/PET	Rubbing	$\sim$ 400	$\sim$ 60	[120]
Graphene/PEDOT:PSS	Rod-coating	$\sim$ 1902	$\sim$ 90	[118]
GO:PEDOT:PSS	Drop-casting	$\sim$ 400 - 500	$\sim$ 78	[121]
TLGA (SPGSW/PH1000/PH1000)	Drop-casting	$\sim$ 88	$\sim$ 78	This work
TLGA (PGD/PH1000/PH1000)	Drop-casting	$\sim$ 170	$\sim$ 74	This work
HMGA (PH1000:PGD - 6 layers)	Spin-coating	$\sim$ 134	$\sim$ 79	This work

5.2 Concept test: PGD-based TLGA and HMGA as anodes in OSCs

PGD-based TLGA and HMGA were implemented in PM6:Y7-based OSCs as anodes. Fig. 5-11 shows the device architecture and diagram of the device energy levels (previously reported in [20, 24, 122, 123]).

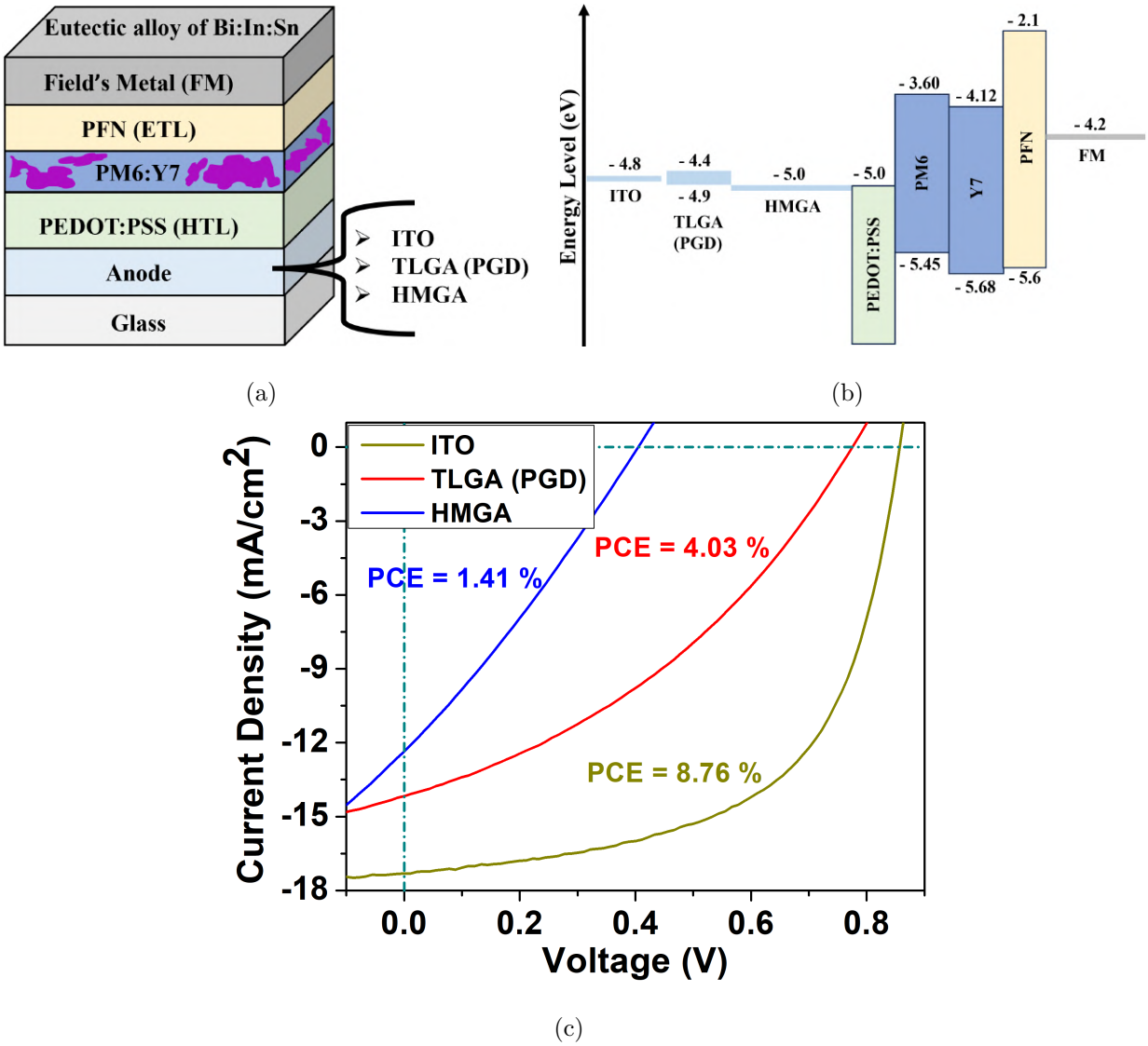

Figure 5-11: (a) OSCs architecture, (b) OSCs energy levels, and (c) OSCs J-V curves for ITO, PGD-based TLGA and HMGA.

Figure 5-11c shows the J-V curves for the OSCs with the configuration glass/anode/ PEDOT:PSS/PM6:Y7/PFN/FM; the PV parameters are summarized in the table 5-4. The difference in PCEs values could be mainly attributed to the decrease in transmittance and increase in electrical resistance in both alternative electrodes, PGD-based TLGA (T (at 550 nm) $\sim$ 74 % and R $\sim$ 170 Ω/sq) and HMGA (T (at 550 nm) $\sim$ 79 % and R $\sim$ 134 Ω/sq), compared to ITO (T (at 550 nm) $\sim$ 88 % and R $\sim$ 10 - 15 Ω/sq), which would affect the

generation of charge carriers (less transmittance) and facilitate trapping and recombination of charges (increase in electrical resistance). On the other hand, the difference in PV performance between PGD-based TLGA and HMGA could be partially due to the variation of the sheet thickness of each alternative anode, PGD-based TLGA ($\sim$ 106 nm) and HMGA ($\sim$ 170 nm), which could influence the charge generation and conduction in the bulk layer through different film conformations. However, for the TLGA case, the device performance could be considered moderately acceptable with respect to other studies [24,117,124], therefore, these concept tests reveal the potential of graphene material for future applications in photovoltaic devices. Furthermore, it is important to mention several relevant aspects: (1) various OSCs reported in the literature implemented top electrodes deposited by evaporation (Al, Ag, Au, Ca, etc.), on the contrary, devices manufactured in these concept tests used a top electrode (Field's Metal) that is easy to deposit, and it does not require evaporation and high vacuum techniques. (2) The graphene material, PGD, is not doped with any metallic nanostructure. (3) The deposition of the PGD, in TLGA, was carried out by drop casting, which is an easy-to-use and low-cost technique. With this stated procedure, the electrode achieved optical and electrical parameters comparable to other reports in the literature that used more expensive and complex deposition techniques [118,120,124]. (4) Deposition, fabrication and tests of the electrodes and OSCs were carried out under regular atmosphere conditions. However, it is necessary to continue optimizing the deposition and manufacturing processes of the electrode and OSCs. (5) The contribution of PGD to the stability of the alternative anodes was acceptable. Particularly, in terms of electrical resistance, PGD may have delayed the degradation process of PH1000, facilitating greater compaction of the films and thus contributing to the stabilization of the electrical parameter of the alternative anodes.

Table 5-4: PV parameters for HMGA, TLGA based on PGD and ITO.

Anodes	**V_{OC} (V)**	**J_{SC} (mA/cm^2)**	**FF**	**PCE (%)**	**T (%)**	**R (Ω/sq)**
ITO (Indium tin oxide)	0.86	- 17.33	0.59	8.76	$\sim$ 88	10 - 15
TLGA (PGD/PH1000/PH1000)	0.78	- 14.17	0.37	4.03	$\sim$ 74	$\sim$ 170
HMGA (PH1000:PGD - 6 layers)	0.41	- 12.36	0.28	1.41	$\sim$ 79	$\sim$ 134

Table 5-5 shows a comparison between our PV results and previous studies that have incorporated graphene electrodes in solar devices. In some cases, our solar devices exhibited PV parameters with quite acceptable values compared to previous reports. Furthermore, these results highlight that drop-casting or spin-coating techniques, are viable and efficient options to fabricate graphene electrodes in an accessible and rapid manner.

Table 5-5: PV parameters of OSCs that use graphene anodes reported in the literature. *Values in parentheses refer to the control OSCs (ITO).

OSCs architecture	**V_{OC} (V)**	**J_{SC} (mA/cm^2)**	**FF**	**PCE (%)**	**Ref.**
glass/Gra/PEDOT:PSS/ PCDTBT:PC_{71}BM/Ca/Ag	0.82 (0.89)	9.36 (10.81)	0.38 (0.53)	2.93 (5.08)	[20]
glass/PH1000/PEDOT:PSS/ PCDTBT:PC_{71}BM/Ca/Ag	0.83 (0.89)	9.18 (10.81)	0.45 (0.53)	3.45 (5.08)	[20]

glass/Gra(wrinkled)/PH1000/ PEDOT:PSS/PCDTBT: $PC_{71}BM$/Ca/Ag	0.84 (0.89)	12.38 (10.81)	0.45 (0.53)	4.67 (5.08)	[20]
glass/SPG/PH1000/PEDOT: PSS/PBDB–T:ITIC/PFN/FM	0.86 (0.88)	12.00 (16.70)	0.41 (0.59)	4.20 (8.60)	[24]
PET/3L Bi-graphene/MoO_x/ PPDT2FBT:$PC_{71}BM$/Ca/Al	0.76 (0.76)	13.70 (14.00)	0.62 (0.66)	6.85 (7.12)	[84]
glass/PI@graphene/PEDOT: PSS/PM6:Y6/PDINO/Al	0.84 (0.85)	25.80 (25.00)	0.70 (0.74)	15.20 (15.70)	[116]
glass/graphene (4 layers)/Cu (7 nm thick)/PEDOT:PSS/ PTB7:$PC_{71}BM$/$PEIH^+Bim_4{}^-$/Al	0.27 (0.74)	10.27 (16.25)	0.24 (0.59)	0.66 (7.05)	[117]
glass/graphene (4 layers)/Cu (3 nm thick)/PEDOT:PSS/ PTB7:$PC_{71}BM$/$PEIH^+Bim_4{}^-$/Al	0.73 (0.74)	13.01 (16.25)	0.46 (0.59)	4.38 (7.05)	[117]
PEN/graphene/ZnO/P3HT: $PC_{61}BM$/PEDOT:PSS/ graphene/Al	0.62 (0.48)	3.60 (5.10)	0.28 (0.30)	0.63 (0.73)	[125]
glass/MLG/MoO_3/PTB7: $PC_{70}BM$/Ca/Al	0.58 (0.69)	4.70 (15.60)	0.26 (0.57)	0.70 (6.10)	[124]

glass/MLG/Ni-grid (40 nm thick)/MoO_3/PTB7:$PC_{70}BM$/Ca/Al	0.64 (0.69)	12.70 (15.60)	0.52 (0.57)	4.20 (6.10)	[124]
glass/Gr&AgNWs/PEDOT:PSS/PM6:Y6/PDINO/Al	0.66 (0.85)	4.37 (24.71)	0.24 (0.75)	0.70 (15.58)	[126]
glass/Gr&AgNWs/PH1000 (160 nm thick)/PEDOT:PSS/PM6:Y6/PDINO/Al	0.83 (0.85)	23.20 (24.71)	0.70 (0.75)	13.44 (15.58)	[126]
glass/TLGA (PGD)/PEDOT:PSS/PM6:Y7/PFN/FM	0.78 (0.86)	14.17 (17.33)	0.37 (0.59)	4.03 (8.76)	This work
glass/HMGA/PEDOT:PSS/PM6:Y7/PFN/FM	0.41 (0.86)	12.36 (17.33)	0.28 (0.59)	1.41 (8.76)	This work

For instance, in reference [124], alternative electrodes composed of a graphene monolayer (MLG) and MLG with nickel grids (MLG/Ni-grid) were implemented, achieving efficiencies of $\sim$ 0.70 % and $\sim$ 4 %, respectively. Compared to our electrodes (PGD-baed TLGA and HMGA), which do not contain any metallic nanostructure, they could be considered to have acceptable performance in solar devices. On the other hand, reference [126] implemented a commercially alternative electrode composed of graphene and silver nanowires (graphene&AgNWs) in PM6:Y6 solar devices, achieving an efficiency of $\sim$ 0.70 %. Given these low efficiencies, they considered adding a layer of PH1000 (160 nm thick) to improve the electrode (graphene&AgNWs/PH1000) roughness reaching a PCE $\sim$ 13.4 %; thus, the addition of PH1000 significantly improved device efficiency and highlighted the capability of PH1000 film; a feature that was also presented in our alternative electrodes (PGD-based TLGA and HMGA) and reflected in the OSCs performance. In addition, the reference [20]

implemented graphene electrodes based on graphene monolayer (Gra) and Gra with PH1000 (Gra/PH1000) in OSCs. These electrodes achieved efficiencies about 2.9 % and 4.7 %, respectively. Once again, the significant influence of the addition of PH1000 in the improvement of these graphene electrodes is highlighted. It is worth noting that the solar devices of references [20,124,126] incorporated metallic top electrodes, which require high vacuum deposition techniques.

Chapter 6

Conclusions

The fabrication and characterization of the three alternative graphene anodes SPGSW-based TLGA, PGD-based TLGA and HMGA were presented. Alternative anodes TLGA based on PGD and HMGA were also implemented in PM6:Y7-based OSCs as a concept test to confirm the application of PGD. In the manufacturing process of the anodes, easy-to-use and low-cost deposition techniques (drop-casting and spin-coating) were used. The HI treatment was applied to SPGSW, PGD and HMGA to remove the oxygenated groups and to improve the films conductivity (SPGSW and PGD) and the anode (HMGA). Also, a UV-ozone plasma treatment was applied to SPGSW and PGD to improve adhesion between the deposited film and conducting polymer PEDOT:PSS (PH1000). The TLGA based on SPGSW, TLGA based on PGD and HMGA achieved T (at 550 nm) $\sim$ 78 % and R $\sim$ 88 Ω/sq, T (at 550 nm) $\sim$ 74 % and R $\sim$ 170 Ω/sq and T (at 550 nm) $\sim$ 79 % and R $\sim$ 134 Ω/sq, respectively; which are quite acceptable results and compared favorably with those of other graphene electrodes that implement complex synthesis processes and deposition techniques. Raman spectroscopy and XRD characterizations provided information on the structural defects of SPGSW and PGD in both film and powder. The observations corroborate that both samples are graphenic materials, as well as that both samples have many defects in their structure, particularly when they were deposited on film. On the other hand, both techniques also corroborated the presence of PGD in the HMGA. Also, the morphology of the alternative electrodes were analyzed, presenting a fairly homogeneous surface, which could be corroborated by AFM and

SEM.

As a concept test, the alternative anodes TLGA based on PGD and HMGA were implemented in PM6:Y7-based OSCs. The achieved efficiencies of $\sim$ 4.0 % for TLGA based on PGD and $\sim$ 1.4 % for HMGA are acceptable concept tests compared to some previous reports. These preliminary results suggest that PGD has promising applications as an alternative electrode to ITO in photovoltaic devices. In addition, it also allows improving and optimizing the manufacturing and deposition processes for both electrodes and OSCs.

6.1 Future work

- To improve the electrical properties of graphene derivative during its synthesis, ensuring that the material has a certain electrical conductivity before subjecting it to chemical or thermal reduction treatments.
- To explore and examine chemical treatment alternatives, such as $NaBH_4$ or hydrazine and its derivatives, to reduce the graphene film and increase its conductivity. These agents could be applied using techniques such as vapor deposition, drop-casting, immersion or other methods.
- To explore thermal treatment as another additional alternative to reduce the graphene layer and thus enhance its electrical conductivity. It would be beneficial to perform thermogravimetric analyzes (TGA) to evaluate how the mass of the graphene material varies in response to temperature variations..
- It would be interesting to explore the incorporation of these graphene electrodes in Perovskite solar cells (PSCs). However, prior to the introduction of these graphene electrodes, it is crucial to have a manufacturing process for PSCs that is well established and guarantees acceptable reproducibility.
- Furthermore, it would be advisable to explore the application of these graphene electrodes in other optoelectronic devices, such as OLEDs, and analyze their performance when used as alternative anodes.

Appendix A

Scientific publications and conferences

1. **Scientific publications**

   - **Alvaro Guerra-Him**, Yaily Fernández-Arteaga, José-Luis Maldonado, Maiby Valle-Orta, Uriel Sierra, Salvador Fernández, and Bernardo Antonio Frontana-Uribe. ***Implementation of an alternative graphene-based electrode***. J. Mater. Sci. Mater. Electron., 34 (6), 2023. DOI: https://doi.org/ 10.1007/s10854-023-09901-x
   - **Alvaro Guerra-Him**, Julio C. Carrillo-Sendejas, José-Luis Maldonado, Yaily Fernández-Arteaga, Maiby Valle-Orta, Uriel Sierra, and Salvador Fernández. ***Processable graphene derivative as an alternative carbon-based electrode***. **Submitted**

2. **Participation in conferences**

   - Presentation on "On the use of a three-layer graphene anode in solar devices" at "31st International Materials Research Congress". Organized by the Mexican Society of Materials A.C., from August 13 to 18, 2023 in Cancún, Quintana Roo, Mexico.
   - Presentation on "An alternative graphene-based electrode for use in solar devices" at the "RIAO/OPTILAS 2023". From March 27 – 31, 2023 in San José, Costa Rica.

- Presentation on "Implementation of an alternative graphene-based electrode and its potential use in solar devices" at "XXX International Materials Research Congress". Organized by the Mexican Society of Materials A.C., from August 14 to 19, 2022 in Cancún, Quintana Roo, Mexico.

References

[1] Janet M. Box-Steffensmeier, Jean Burgess, Maurizio Corbetta, Kate Crawford, Esther Duflo, Laurel Fogarty, Alison Gopnik, Sari Hanafi, Mario Herrero, Ying yi Hong, Yasuko Kameyama, Tatia M.C. Lee, Gabriel M. Leung, Daniel S. Nagin, Anna C. Nobre, Merete Nordentoft, Aysu Okbay, Andrew Perfors, Laura M. Rival, Cassidy R. Sugimoto, Bertil Tungodden, and Claudia Wagner. ***The future of human behaviour research***. *Nat. Hum. Behav.*, 6(1):15–24, 2022.

[2] Krishna Kumar Jaiswal, Chandrama Roy Chowdhury, Deepti Yadav, Ravikant Verma, Swapnamoy Dutta, Km Smriti Jaiswal, SangmeshB, and Karthik Selva Kumar Karuppasamy. ***Renewable and sustainable clean energy development and impact on social, economic, and environmental health***. *Energy Nexus*, 7:100118, 2022.

[3] Hannah Ritchie and Pablo Rosado. ***Fossil Fuels***. *Our World Data.*, 2017.

[4] Nicholas Apergis, Mita Bhattacharya, and Walid Hadhri. ***Health care expenditure and environmental pollution: a cross-country comparison across different income groups***. *Environ. Sci. Pollut. Res.*, 27(8):8142–8156, 2020.

[5] Khuram Shahzad Ahmad, Syeda Naima Naqvi, and Shaan Bibi Jaffri. ***Systematic review elucidating the generations and classifications of solar cells contributing towards environmental sustainability integration***. *Rev. Inorg. Chem.*, 41(1):21–39, 2021.

[6] Mugdha V. Dambhare, Bhavana Butey, and S. V. Moharil. ***Solar photovoltaic technology: A review of different types of solar cells and its future trends***. *J. Phys. Conf. Ser.*, 1913(1), 2021.

[7] Neeraj Kant and Pushpendra Singh. ***Review of next generation photovoltaic solar cell technology and comparative materialistic development***. *Mater. Today Proc.*, 56:3460–3470, 2022.

[8] Um Kanta Aryal, Mehrad Ahmadpour, Vida Turkovic, Horst-Günter Rubahn, Aldo Di Carlo, and Morten Madsen. ***2D materials for organic and perovskite photovoltaics***. *Nano Energy*, 94:106833, 2022.

[9] Jiehao Fu, Patrick W.K. Fong, Heng Liu, Chieh-Szu Huang, Xinhui Lu, Shirong Lu, Maged Abdelsamie, Tim Kodalle, Carolin M. Sutter-Fella, Yang Yang, and Gang Li. ***19.31% Binary Organic Solar Cell and Low Non-Radiative Recombination Enabled By Non-Monotonic Intermediate State Transition***. *Nat. Commun.*, 14(1):1760, 2023.

[10] Zhong Zheng, Jianqiu Wang, Pengqing Bi, Junzhen Ren, Yafei Wang, Yi Yang, Xiaoyu Liu, Shaoqing Zhang, and Jianhui Hou. ***Tandem Organic Solar Cell with 20.2% Efficiency***. *Joule*, 6(1):171–184, 2022.

[11] Yu Zou, Yuping Gao, and Yongsheng Liu. ***The role of organic spacers in 2D/3D hybrid perovskite solar cells***. *Mater. Chem. Front.*, 8(1):82–103, 2023.

[12] The National Renewable Energy Laboratory (NREL). ***Best Research-Cell Efficiency Chart: https://www.nrel.gov/pv/cell-efficiency.html. Last visited: October 22***, 2023.

[13] N. Shah, A. A. Shah, P. K. Leung, S. Khan, K. Sun, X. Zhu, and Q. Liao. ***A Review of Third Generation Solar Cells***. *Processes*, 11(6):1852, 2023.

[14] Sonali Das, Deepak Pandey, Jayan Thomas, and Tania Roy. ***The Role of Graphene and Other 2D Materials in Solar Photovoltaics***. *Adv. Mater.*, 31(1):1–35, 2019.

[15] K. S. Novoselov, A. K. Geim, S. V. Morozov, D. Jiang, Y. Zhang, S. V. Dubonos, I. V. Grigorieva and A. A. Firsov. ***Electric Field Effect in Atomically Thin Carbon Films***. *Science.*, 306:666–669, 2004.

[16] Chintam Hanmandlu, Mamina Sahoo, Chi Ching Liu, Hsin An Chen, Chun Wei Pao, Yun Chorng Chang, Chih Wei Chu, and Chao Sung Lai. ***Few-layer fluorine-functionalized graphene hole-selective contacts for efficient inverted perovskite solar cells***. *Chem. Eng. J.*, 430:132831, 2022.

[17] Dinh Cung Tien Nguyen, Van Dung Mai, Van Huong Tran, Van Phu Vu, and Soo Hyoung Lee. ***Use of modified PEDOT:PSS/Graphene oxide dispersions as a hole transport layer for inverted bulk-heterojunction organic solar cells***. *Org. Electron.*, 100:106388, 2022.

[18] Ghazaleh Bagha, Homam Naffakh-Moosavy, and Mansour Rezaee Mersagh. ***The effect of reduced graphene oxide sheet on the optical and electrical characteristics of Ni-doped and Ag-doped ZnO ETLs in planar perovskite solar cells***. *J. Alloys Compd.*, 870:159658, 2021.

[19] Kavitha Pandi, Thimmapyampalayam Ramasamy Naveen Kumar, Sandeep Kumar Lakhera, and Bernaurdshaw Neppolian. ***Simultaneous Passivation of Surface Vacancies and Enhancement in Charge Transfer Property of ZnO Electron Transport Layer for Inverted Organic Solar Cells***. *Energy Technol.*, 8(11):1–13, 2020.

[20] Yang Chen, Yuan-yuan Yue, Shi-Rong Wang, Nan Zhang, Jing Feng, and Hong-Bo Sun. ***Thermally-induced wrinkles on PH1000/graphene composite electrode for enhanced efficiency of organic solar cells***. *Sol. Energy Mater. Sol. Cells*, 201:110075, 2019.

[21] Hyangki Sung, Namyoung Ahn, Min Seok Jang, Jong Kwon Lee, Heetae Yoon, Nam Gyu Park, and Mansoo Choi. ***Transparent Conductive Oxide-Free***

Graphene-Based Perovskite Solar Cells with over 17% Efficiency. *Adv. Energy Mater.*, 6(3):2–7, 2016.

[22] Yang Chen, Yuan Yuan Yue, Shi Rong Wang, Nan Zhang, Jing Feng, and Hong Bo Sun. ***Graphene as a Transparent and Conductive Electrode for Organic Optoelectronic Devices***. *Adv. Electron. Mater.*, 5(10):1–29, 2019.

[23] Edwin T. Mombeshora, Edigar Muchuweni, Rodrigo Garcia-Rodriguez, Matthew L. Davies, Vincent O. Nyamori, and Bice S. Martincigh. ***A review of graphene derivative enhancers for perovskite solar cells***. *Nanoscale Adv.*, 4(9):2057–2076, 2022.

[24] Yaily Fernández-Arteaga, José-Luis Maldonado, Juan Nicasio-Collazo, Marco-Antonio Meneses-Nava, Mario Rodríguez, Oracio Barbosa-García, Uriel Sierra, Salvador Fernández, and Bernardo Antonio Frontana-Uribe. ***Solution processable graphene derivative used in a bilayer anode with conductive PEDOT:PSS on the non-fullerene PBDB-T:ITIC based organic solar cells***. *Sol. Energy*, 225:656–665, 2021.

[25] David Kearns and Melvin Calvin. ***Photovoltaic effect and photoconductivity in laminated organic systems***. *J. Chem. Phys.*, 29(4):950–951, 1958.

[26] C. W. Tang. ***Two-layer organic photovoltaic cell***. *Appl. Phys. Lett.*, 48(2):183–185, 1986.

[27] Dou Luo, Woongsik Jang, Dickson D. Babu, Min Soo Kim, Dong Hwan Wang, and Aung Ko Ko Kyaw. ***Recent progress in organic solar cells based on non-fullerene acceptors: materials to devices***. *J. Mater. Chem. A*, 10(7):3255–3295, 2022.

[28] G. Yu, J. Gao, J. C. Hummelen, F. Wudi and A. J. Heeger. ***Polymer Photovoltaic Cells: Enhanced Efficiencies via a Network of Internal Donor-Acceptor Heterojunctions***. *Science.*, 270:1–3, 1995.

[29] Gang Li, Vishal Shrotriya, Jinsong Huang, Yan Yao, Tom Moriarty, Keith Emery, and Yang Yang. ***High-efficiency solution processable polymer photovoltaic cells by self-organization of polymer blends***. *Nat. Mater.*, 4(11):864–868, 2005.

[30] Wanli Ma, Cuiying Yang, Xiong Gong, Kwanghee Lee, and Alan J. Heeger. ***Thermally stable, efficient polymer solar cells with nanoscale control of the interpenetrating network morphology***. *Adv. Funct. Mater.*, 15(10):1617–1622, 2005.

[31] Yuze Lin, Jiayu Wang, Zhi Guo Zhang, Huitao Bai, Yongfang Li, Daoben Zhu, and Xiaowei Zhan. ***An electron acceptor challenging fullerenes for efficient polymer solar cells***. *Adv. Mater.*, 27(7):1170–1174, 2015.

[32] Wenchao Zhao, Deping Qian, Shaoqing Zhang, Sunsun Li, Olle Inganäs, Feng Gao, and Jianhui Hou. ***Fullerene-Free Polymer Solar Cells with over 11% Efficiency and Excellent Thermal Stability***. *Adv. Mater.*, 28(23):4734–4739, 2016.

[33] Lingxian Meng, Yamin Zhang, Xiangjian Wan, Chenxi Li, Xin Zhang, Yanbo Wang, Xin Ke, Zuo Xiao, Liming Ding, Ruoxi Xia, Hin Lap Yip, Yong Cao, and Yongsheng Chen. ***Organic and solution-processed tandem solar cells with 17.3% efficiency***. *Science (80-.).*, 361(6407):1094–1098, 2018.

[34] Hui Huang and Wei Deng. ***Introduction to Organic Solar Cells***. In *Org. Hybrid Sol. Cells*, chapter 1, pages 1–18. Springer, 2014.

[35] Kojima; A, Teshima K, Shirai; Y, and Miyasaka; T. ***Organometal halide perovskites as visible-light sensitizers for photovoltaic cells***. *J. Am. Chem. Soc.*, 131(17):6050–6051, 2009.

[36] Hui Seon Kim, Chang Ryul Lee, Jeong Hyeok Im, Ki Beom Lee, Thomas Moehl, Arianna Marchioro, Soo Jin Moon, Robin Humphry-Baker, Jun Ho Yum, Jacques E. Moser, Michael Grätzel, and Nam Gyu Park. ***Lead iodide perovskite sensitized all-solid-state submicron thin film mesoscopic solar cell with efficiency exceeding 9%***. *Sci. Rep.*, 2:1–7, 2012.

[37] Lee Michael M., Teuscher Joel, Miyasaka Tsutomu, Murakami Takurou N., and Snaith Henry J. ***Efficient Hybrid Solar Cells Basedon Meso-Superstructured Organometal Halide Perovskites***. *Science (80-.).*, 338(6107):643–647, 2012.

[38] Wei Chen, Yongzhen Wu, Youfeng Yue, Jian Liu, Wenjun Zhang, Xudong Yang, Han Chen, Enbing Bi, Islam Ashraful, Michael Grätzel, and Liyuan Han. ***Efficient and stable large-area perovskite solar cells with inorganic charge extraction layers***. *Science (80-.).*, 350(6263):944–948, 2015.

[39] Xiaopeng Zheng, Bo Chen, Jun Dai, Yanjun Fang, Yang Bai, Yuze Lin, Haotong Wei, Xiao Cheng Zeng, and Jinsong Huang. ***Defect passivation in hybrid perovskite solar cells using quaternary ammonium halide anions and cations***. *Nat. Energy*, 2(7):1–9, 2017.

[40] Xiaopeng Zheng, Yi Hou, Chunxiong Bao, Jun Yin, Fanglong Yuan, Ziru Huang, Kepeng Song, Jiakai Liu, Joel Troughton, Nicola Gasparini, Chun Zhou, Yuanbao Lin, Ding Jiang Xue, Bin Chen, Andrew K. Johnston, Nini Wei, Mohamed Nejib Hedhili, Mingyang Wei, Abdullah Y. Alsalloum, Partha Maity, Bekir Turedi, Chen Yang, Derya Baran, Thomas D. Anthopoulos, Yu Han, Zheng Hong Lu, Omar F. Mohammed, Feng Gao, Edward H. Sargent, and Osman M. Bakr. ***Managing grains and interfaces via ligand anchoring enables 22.3%-efficiency inverted perovskite solar cells***. *Nat. Energy*, 5(2):131–140, 2020.

[41] Hanul Min, Do Yoon Lee, Junu Kim, Gwisu Kim, Kyoung Su Lee, Jongbeom Kim, Min Jae Paik, Young Ki Kim, Kwang S. Kim, Min Gyu Kim, Tae Joo Shin, and Sang Il Seok. ***Perovskite solar cells with atomically coherent interlayers on SnO2 electrodes***. *Nature*, 598:444–450, 2021.

[42] Xiaodong Li, Wenxiao Zhang, Xuemin Guo, Chunyan Lu, Jiyao Wei, and Junfeng Fang. ***Constructing heterojunctions by surface sulfidation for efficient inverted perovskite solar cells***. *Science.*, 375(6579):434–437, 2022.

[43] Zhen Li, Bo Li, Xin Wu, Stephanie A. Sheppard, Shoufeng Zhang, Danpeng Gao, Nicholas J. Long, and Zonglong Zhu. ***Organometallic-functionalized interfaces for highly efficient inverted perovskite solar cells***. *Science.*, 376(6591):416–420, 2022.

[44] Qi Jiang, Jinhui Tong, Yeming Xian, Ross A. Kerner, Sean P. Dunfield, Chuanxiao Xiao, Rebecca A. Scheidt, Darius Kuciauskas, Xiaoming Wang, Matthew P. Hautzinger, Robert Tirawat, Matthew C. Beard, David P. Fenning, Joseph J. Berry, Bryon W. Larson, Yanfa Yan, and Kai Zhu. ***Surface reaction for efficient and stable inverted perovskite solar cells***. *Nature*, 611:278–283, 2022.

[45] Qiang Bei, Bei Zhang, Kaifeng Wang, Shiming Zhang, Guichuan Xing, and Clément Cabanetos. ***Benzothiadiazole-based materials for organic solar cells***. *Chinese Chem. Lett.*, 35(1):108438, 2023.

[46] Yang Li, Wei Huang, Dejiang Zhao, Lu Wang, Zhiqiang Jiao, Qingyu Huang, Peng Wang, Mengna Sun, and Guangcai Yuan. ***Recent Progress in Organic Solar Cells: A Review on Materials from Acceptor to Donor***. *Molecules*, 27(6), 2022.

[47] N. S. Sariciftci, L. Smilowitz, A. J. Heeger, and F. Wudi. ***Photoinduced Electron Transfer from a Conducting Polymer to Buckminsterfullerene***. *C. R. B. List. Geophys. J. R. Astron. Soc*, 104:8389, 1991.

[48] Jianhua Chen, Yao Chen, Liang Wen Feng, Chunling Gu, Guoping Li, Ning Su, Gang Wang, Steven M. Swick, Wei Huang, Xugang Guo, Antonio Facchetti, and Tobin J. Marks. ***Hole (donor) and electron (acceptor) transporting organic semiconductors for bulk-heterojunction solar cells***. *EnergyChem*, 2(5):100042, 2020.

[49] Shi-yu Yuan, Hang Zhao, Yi-tong Wang, Zhen-zhen Li, Xiao-dong Wang, and Wei-peng Cao. ***Research status of all-inorganic perovskite solar cells: A review***. *J. Solid State Chem.*, 328:124299, 2023.

[50] Syed M. Hasnain. ***Examining the advances, obstacles, and achievements of tin-based perovskite solar cells: a review***. *Sol. Energy*, 262:111825, 2023.

[51] Zhifang Wu, Enbing Bi, Luis K. Ono, Dengbing Li, Osman M. Bakr, Yanfa Yan, and Yabing Qi. ***Passivation strategies for enhancing device performance of perovskite solar cells***. *Nano Energy*, 115:108731, 2023.

[52] Tanzi Ahmed Chowdhury, Md Arafat Bin Zafar, Md Sajjad-Ul Islam, M. Shahinuzzaman, Mohammad Aminul Islam, and Mayeen Uddin Khandaker. ***Stability of perovskite solar cells: issues and prospects***. *RSC Adv.*, 13(3):1787–1810, 2023.

[53] George G. Njema and Joshua K. Kibet. ***A Review of the Technological Advances in the Design of Highly Efficient Perovskite Solar Cells***. *Int. J. Photoenergy*, 2023, 2023.

[54] Ebru Kondolot Solak and Erdal Irmak. ***Advances in organic photovoltaic cells: a comprehensive review of materials, technologies, and performance***. *RSC Adv.*, 13(18):12244–12269, 2023.

[55] Thomas Baumeler, Amina A. Saleh, Tajamul A. Wani, Siming Huang, Xiaohan Jia, Xinyu Bai, Mojtaba Abdi-Jalebi, Neha Arora, Michael Grätzel, and M. Ibrahim Dar. ***Champion Device Architectures for Low-Cost and Stable Single-Junction Perovskite Solar Cells***. *ACS Mater. Lett.*, 5:2408–2421, 2023.

[56] Priyanka P. Kumavat, Prashant Sonar, and Dipak S. Dalal. ***An overview on basics of organic and dye sensitized solar cells, their mechanism and recent improvements***. *Renew. Sustain. Energy Rev.*, 78:1262–1287, 2017.

[57] Sanwan Liu, Vasudevan P. Biju, Yabing Qi, Wei Chen, and Zonghao Liu. ***Recent progress in the development of high-efficiency inverted perovskite solar cells***. *NPG Asia Mater.*, 15(1), 2023.

[58] Michael Saliba and Lioz Etgar. ***Current density mismatch in Perovskite solar cells***. *ACS Energy Lett.*, 5(9):2886–2888, 2020.

[59] Eugen Zimmermann, Philipp Ehrenreich, Thomas Pfadler, James A. Dorman, Jonas Weickert, and Lukas Schmidt-Mende. ***Erroneous efficiency reports harm organic solar cell research***. *Nat. Photonics*, 8(9):669–672, 2014.

[60] Jonathan D. Servaites, Mark A. Ratner, and Tobin J. Marks. ***Organic solar cells: A new look at traditional models***. *Energy Environ. Sci.*, 4(11):4410–4422, 2011.

[61] Mahmoud N. Zidan, Nicola Everitt, Tawfik Ismail, and Irene S. Fahim. ***Review organic solar cells parameters extraction and characterization techniques***. *Polymers (Basel).*, 13(19):1–19, 2021.

[62] Ali Khorami and Mojtaba Joodaki. ***Extracting voltage-dependent series resistance of single diode model for organic solar cells***. *SN Appl. Sci.*, 1(6):1–11, 2019.

[63] Fahmi F. Muhammad, Mohd Y. Yahya, Shilan S. Hameed, Fakhra Aziz, Khaulah Sulaiman, Mariwan A. Rasheed, and Zubair Ahmad. ***Employment of single-diode model to elucidate the variations in photovoltaic parameters under different electrical and thermal conditions***. *PLoS One*, 12(8), 2017.

[64] Kang Shyang Liao, Soniya D. Yambem, Amrita Haldar, Nigel J. Alley, and Seamus A. Curran. ***Designs and architectures for the next generation of organic solar cells***. *Energies*, 3(6):1212–1250, 2010.

[65] R. Ramarajan, D. Paul Joseph, K. Thangaraju and M. Kovendhan. ***Indium-Free Alternative Transparent Conducting Electrodes: An Overview and Recent Developments***. In Saravanan Rajendran, Jiaqian Qin, Francisco Gracia and Eric Lichtfouse, editors, *Met. Met. Oxides Energy Electron.*, chapter 5, pages 149–183. Springer, 2021.

[66] Yumeng Xu, Zhenhua Lin, Wei Wei, Yue Hao, Shengzhong Liu, Jianyong Ouyang, and Jingjing Chang. ***Recent Progress of Electrode Materials for Flexible Perovskite Solar Cells***. *Nano-Micro Lett.*, 14(1):1–30, 2022.

[67] Tingting Wang, Kuankuan Lu, Zhuohui Xu, Zimian Lin, Honglong Ning, Tian Qiu, Zhao Yang, Hua Zheng, Rihui Yao, and Junbiao Peng. ***Recent developments in flexible transparent electrode***. *Crystals*, 11(5):1–22, 2021.

[68] Pan Wen, Ruixiang Peng, Wei Song, Jinfeng Ge, Xu Yin, Xia Chen, Cuirong Liu, Xiaoli Zhang, and Ziyi Ge. ***A simple and effective method via PH1000 modified Ag-Nanowires electrode enable efficient flexible nonfullerene organic solar cells***. *Org. Electron.*, 94:106172, 2021.

[69] Il Jeon, Jungjin Yoon, Unsoo Kim, Changsoo Lee, Rong Xiang, Ahmed Shawky, Jun Xi, Junseop Byeon, Hyuck Mo Lee, Mansoo Choi, Shigeo Maruyama, and Yutaka Matsuo. ***High-Performance Solution-Processed Double-Walled Carbon Nanotube Transparent Electrode for Perovskite Solar Cells***. *Adv. Energy Mater.*, 9(27):1–10, 2019.

[70] Jae-Gyeong Kim, Seok-In Na, and Han-Ki Kim. ***Flexible and transparent IWO films prepared by plasma arc ion plating for flexible perovskite solar cells***. *AIP Adv.*, 8(10), 2018.

[71] Karim Khan, Ayesha Khan Tareen, Muhammad Iqbal, Zhe Shi, Han Zhang, and Zhongyi Guo. ***Novel emerging graphdiyne based two dimensional materials: Synthesis, properties and renewable energy applications***. *Nano Today*, 39:101207, 2021.

[72] Run-Sen Zhang and Jin-Wu Jiang. ***Frontiers of Physics The art of designing carbon allotropes***. *Front. Phys*, 14(1):13401, 2019.

[73] Luca Bellucci and Valentina Tozzini. ***Engineering 3D graphene-based materials: State of the art and perspectives***. *Molecules*, 25(2), 2020.

[74] Pankaj Chamoli, Soma Banerjee, K. K. Raina and Kamal K. Kar. ***Characteristics of Graphene/Reduced Graphene Oxide.*** In *Handb. Nanocomposite Supercapacitor Mater. I.*, volume 300, chapter 5, pages 155–173. Springer Series in Materials Science, 2020.

[75] Alexander A. Balandin. ***Thermal properties of graphene and nanostructured carbon materials***. *Nat. Mater.*, 10(8):569–581, 2011.

[76] Dimitrios G. Papageorgiou, Ian A. Kinloch, and Robert J. Young. ***Graphene/elastomer nanocomposites***. *Carbon N. Y.*, 95:460–484, 2015.

[77] Akanksha R. Urade, Indranil Lahiri, and K. S. Suresh. ***Graphene Properties, Synthesis and Applications: A Review***. *Jom*, 75(3):614–630, 2023.

[78] Tahreem Nawz, Amna Safdar, Muzammil Hussain, Dae Sung Lee, and Muhammad Siyar. ***Graphene to Advanced MoS2: A Review of Structure, Synthesis, and Optoelectronic Device Application***. pages 1–31, 2020.

[79] Neeraj Kumar, Reza Salehiyan, Vongani Chauke, Orebotse Joseph Botlhoko, Katlego Setshedi, Manfred Scriba, Mike Masukume, and Suprakas Sinha Ray. ***Top-down synthesis of graphene: A comprehensive review***. *FlatChem*, 27(January):100224, 2021.

[80] Aojie Zhang, Zihao Wang, Hao Ouyang, Wenhao Lyu, Jingxuan Sun, Yuan Cheng, and Bo Fu. ***Recent progress of two-dimensional materials for ultrafast photonics***. *Nanomaterials*, 11(7):1–46, 2021.

[81] Dong Hee Shin, Sang Woo Seo, Jong Min Kim, Ha Seung Lee, and Suk-Ho Choi. ***Graphene transparent conductive electrodes doped with graphene quantum dots-mixed silver nanowires for highly-flexible organic solar cells***. *J. Alloys Compd.*, 744:1–6, 2018.

[82] Chunyang Zhang, Shi Wang, Hong Zhang, Yulin Feng, Wenming Tian, Ying Yan, Jiming Bian, Yuchen Wang, Shengye Jin, Shaik Mohammed Zakeeruddin, Michael Grätzel, and Yantao Shi. ***Efficient stable graphene-based perovskite solar cells with high flexibility in device assembling: Via modular architecture design***. *Energy Environ. Sci.*, 12(12):3585–3594, 2019.

[83] Gyujeong Jeong, Donghwan Koo, Jihyung Seo, Seungon Jung, Yunseong Choi, Junghyun Lee, and Hyesung Park. ***Suppressed interdiffusion and degradation in flexible and transparent metal electrode-based perovskite solar cells with a graphene interlayer***. *Nano Lett.*, 20(5):3718–3727, 2020.

[84] Jinhong Du, Dingdong Zhang, Xiao Wang, Hui Jin, Weimin Zhang, Bo Tong, Yu Liu, Paul L. Burn, Hui Ming Cheng, and Wencai Ren. ***Extremely efficient flexible organic solar cells with a graphene transparent anode: Dependence on number of layers and doping of graphene***. *Carbon N. Y.*, 171:350–358, 2021.

[85] Rui Chen, Kuan Sun, Qi Zhang, Yongli Zhou, Meng Li, Yuyang Sun, Zhou Wu, Yuyang Wu, Xinlu Li, Jialei Xi, Chi Ma, Yiyang Zhang, and Jianyong Ouyang. ***Sequential Solution Polymerization of Poly(3,4-ethylenedioxythiophene)Using V2O5 as Oxidant for Flexible Touch Sensors***. *iScience*, 12:66–75, 2019.

[86] Minghua Kong, Miquel Garriga, Juan Sebastián Reparaz, and Maria Isabel Alonso. ***Advanced Optical Characterization of PEDOT:PSS by Combining Spectroscopic Ellipsometry and Raman Scattering***. *ACS Omega*, 7(43):39429–39436, 2022.

[87] A. Young Lee, Kihyuk Yang, Nguyen Duc Anh, Chulho Park, Seung Mi Lee, Tae Geol Lee, and Mun Seok Jeong. ***Raman study of D* band in graphene oxide and its correlation with reduction***. *Appl. Surf. Sci.*, 536:147990, 2021.

[88] R. Bakhshandeh and A. Shafiekhani. ***Ultrasonic waves and temperature effects on graphene structure fabricated by electrochemical exfoliation method***. *Mater. Chem. Phys.*, 212:95–102, 2018.

[89] Jiang-Bin Wu, Miao-Ling Lin, Xin Cong, He-Nan Liu, and Ping-Heng Tan. ***Raman spectroscopy of graphene-based materials and its applications in related devices***. *Chem. Soc. Rev.*, 47(5):1822–1873, 2018.

[90] Gaurav Kumar Yogesh, E. P. Shuaib, Purandhi Roopmani, Manju Bhargavi Gumpu, Uma Maheswari Krishnan, and D. Sastikumar. ***Synthesis, characterization***

and bioimaging application of laser-ablated graphene-oxide nanoparticles (nGOs). *Diam. Relat. Mater.*, 104:107733, 2020.

[91] It-Meng Low, Hani Manssor Albetran, and Michael Degiorgio. ***Structural Characterization of Commercial Graphite and Graphene Materials***. *J. Nanotechnol. Nanomater.*, 1(1):23–30, 2020.

[92] Karthikeyan Krishnamoorthy, Gui Shik Kim, and Sang Jae Kim. ***Graphene nanosheets: Ultrasound assisted synthesis and characterization***. *Ultrason. Sonochem.*, 20(2):644–649, 2013.

[93] Bablu Basumatary, Santanu Podder, Samir Thakur, Jyotisman Bora, Bikash Sharma, Sankar Moni Borah, Nirab Ch Adhikary, Dinkar S. Patil, and Arup R. Pal. ***Synergistic Effect of Au Interband Transition on Graphene Oxide/ZnO Heterostructure: Experimental Analysis with FDTD Simulation***. *ACS Omega*, 7(9):7662–7674, 2022.

[94] Jie Tian, Sai Wu, Xianglu Yin, and Wei Wu. ***Novel preparation of hydrophilic graphene/graphene oxide nanosheets for supercapacitor electrode***. *Appl. Surf. Sci.*, 496:143696, 2019.

[95] Jie Tian, Li Guo, Xianglu Yin, and Wei Wu. ***The liquid-phase preparation of graphene by shear exfoliation with graphite oxide as a dispersant***. *Mater. Chem. Phys.*, 223:1–8, 2019.

[96] Li Guo, Xianglu Yin, Wei Wu, and Hong Meng. ***Preparation of graphene via liquid-phase exfoliation with high gravity technology from edge-oxidized graphite***. *Colloids Surfaces A Physicochem. Eng. Asp.*, 531:25–31, 2017.

[97] Vibhor Thapliyal, Mohamad E. Alabdulkarim, Donna R. Whelan, Bandita Mainali, and James L. Maxwell. ***A concise review of the Raman spectra of carbon allotropes***. *Diam. Relat. Mater.*, 127:109180, 2022.

[98] Sreemannarayana Mypati, Andrew Sellathurai, Marianna Kontopoulou, Aristides Docoslis, and Dominik P.J. Barz. ***High concentration graphene nanoplatelet dispersions in water stabilized by graphene oxide***. *Carbon N. Y.*, 174:581–593, 2021.

[99] Meenu Sharma, Sonam Rani, Devesh K. Pathak, Ravi Bhatia, Rajesh Kumar, and I. Sameera. ***Temperature dependent Raman modes of reduced graphene oxide: Effect of anharmonicity, crystallite size and defects***. *Carbon N. Y.*, 184:437–444, 2021.

[100] Anastasia V. Tyurnina, Iakovos Tzanakis, Justin Morton, Jiawei Mi, Kyriakos Porfyrakis, Barbara M. Maciejewska, Nicole Grobert, and Dmitry G. Eskin. ***Ultrasonic exfoliation of graphene in water: A key parameter study***. *Carbon N. Y.*, 168:737–747, 2020.

[101] David López-Díaz, Marta López Holgado, José L. García-Fierro, and M. Mercedes Velázquez. ***Evolution of the Raman Spectrum with the Chemical Composition of Graphene Oxide***. *J. Phys. Chem. C*, 121(37):20489–20497, 2017.

[102] Rajib Kar and Namita Maiti. ***Observation of D band splitting in vertically aligned graphene nanowalls and their evolution with laser power during Raman spectroscopy***. *J. Nanoparticle Res.*, 23(1), 2021.

[103] H. M. Albetran. ***Investigation of the Morphological, Structural, and Vibrational Behaviour of Graphite Nanoplatelets***. *J. Nanomater.*, 2021, 2021.

[104] Gintare Rimkute, Mantvydas Gudaitis, Jurgis Barkauskas, Aleksej Zarkov, Gediminas Niaura, and Justina Gaidukevic. ***Synthesis and Characterization of Graphite Intercalation Compounds with Sulfuric Acid***. *Crystals*, 12(3):421, 2022.

[105] Swapan Das, Chandan K. Ghosh, Chandan K. Sarkar, and Sunipa Roy. ***Facile synthesis of multi-layer graphene by electrochemical exfoliation using organic solvent***. *Nanotechnol. Rev.*, 7(6):497–508, 2018.

[106] Yun Hwangbo, Choong-Kwang Lee, Alexander E. Mag-Isa, Jae-Won Jang, Hak-Joo Lee, Soon-Bok Lee, Seong-Su Kim, and Jae-Hyun Kim. ***Interlayer non-coupled optical properties for determining the number of layers in arbitrarily stacked multilayer graphenes***. *Carbon N. Y.*, 77:454–461, 2014.

[107] Bing Ma, Raul D. Rodriguez, Alexey Ruban, Sergey Pavlov, and Evgeniya Sheremet. ***The correlation between electrical conductivity and second-order Raman modes of laser-reduced graphene oxide***. *Phys. Chem. Chem. Phys.*, 21(19):10125–10134, 2019.

[108] Fei Zhong, Yi He, Pingquan Wang, Chunlin Chen, Yan Lin, Youqing Wu, and Jingyu Chen. ***Self-assembled graphene oxide-graphene hybrids for enhancing the corrosion resistance of waterborne epoxy coating***. *Appl. Surf. Sci.*, 488:801–812, 2019.

[109] Wei Liu and Giorgio Speranza. ***Tuning the Oxygen Content of Reduced Graphene Oxide and Effects on Its Properties***. *ACS Omega*, 6(9):6195–6205, 2021.

[110] Guohua Chen, Wengui Weng, Dajun Wu, Cuiling Wu, Jinrong Lu, Pingping Wang, and Xiangfeng Chen. ***Preparation and characterization of graphite nanosheets from ultrasonic powdering technique***. *Carbon N. Y.*, 42(4):753–759, 2004.

[111] Fadi Dawaymeh, Yawar Abbas, Maryam Khaleel, Anas Alazzam, and Nahla Alamoodi. ***Tuning the surface wettability of cyclic olefin copolymer by plasma treatment and graphene oxide deposition and reduction***. *Polymers (Basel).*, 13(14), 2021.

[112] Iftikhar Ali Sahito, Kyung Chul Sun, Alvira Ayoub Arbab, and Sung Hoon Jeong. ***Synergistic effect of thermal and chemical reduction of graphene oxide at the counter electrode on the performance of dye-sensitized solar cells***. *Sol. Energy*, 190:112–118, 2019.

[113] Xinkai Wu, Lu Lian, Shuai Yang, and Gufeng He. ***Highly conductive PEDOT:PSS and graphene oxide hybrid film from a dipping treatment with hydroiodic acid for organic light emitting diodes***. *J. Mater. Chem. C*, 4(36):8528–8534, 2016.

[114] Ashis K. Sarker, Jaehoon Kim, Boon Hong Wee, Hyung Jun Song, Yeonkyung Lee, Jong Dal Hong, and Changhee Lee. ***Hydroiodic acid treated PEDOT:PSS thin film as transparent electrode: an approach towards ITO free organic photovoltaics***. *RSC Adv.*, 5(64):52019–52025, 2015.

[115] Van Dang Tran, S. V.N. Pammi, Byeong Ju Park, Yire Han, Cheolho Jeon, and Soon Gil Yoon. ***Transfer-free graphene electrodes for super-flexible and semi-transparent perovskite solar cells fabricated under ambient air***. *Nano Energy*, 65:104018, 2019.

[116] Donghwan Koo, Sungwoo Jung, Jihyung Seo, Gyujeong Jeong, Yunseong Choi, Junghyun Lee, Sang Myeon Lee, Yongjoon Cho, Mingyu Jeong, Jungho Lee, Jiyeon Oh, Changduk Yang, and Hyesung Park. ***Flexible Organic Solar Cells Over 15% Efficiency with Polyimide-Integrated Graphene Electrodes***. *Joule*, 4(5):1021–1034, 2020.

[117] Ju Hwan Kang, Sukyung Choi, Yu Jung Park, Jin Sung Park, Nam Sung Cho, Shinuk Cho, Bright Walker, Dong Soo Choi, Jin-Wook Shin, and Jung Hwa Seo. ***Cu/graphene hybrid transparent conducting electrodes for organic photovoltaic devices***. *Carbon.*, 171:341–349, 2021.

[118] Zhe Li, Xinyu Zhang, Long Shen, Zhijun Fan, Xuewen Chen, Min Chen, Shaohua Qiu, Fatemeh Zabihi, Morteza Eslamian, and Qianli Chen. ***Performance enhancement of large-area graphene–polymer flexible transparent conductive films fabricated by ultrasonic substrate vibration-assisted rod coating***. *J. Coatings Technol. Res.*, 16(6):1773–1780, 2019.

[119] Jun Jun Jin, Jinhua Li, Qidong Tai, Yuan Chen, Debesh Devadutta Mishra, Wenqiu Deng, Juan Xin, Songyang Guo, Bichen Xiao, and Xianbao Wang. ***Efficient and stable flexible perovskite solar cells based on graphene-AgNWs substrate and carbon electrode without hole transport materials***. *J. Power Sources*, 482:228953, 2021.

[120] Sandeep Sharma, Karamvir Singh, Sandeep Kumar, Abhimanyu Rana, Kapil Bhatt, Y. Dwivedi, Monish Gupta, and C.C. Tripathi. ***Optical and electrical investigations of rubbing assisted few-layer graphene thin film for feasibility of flexible electrode***. *Optik (Stuttg).*, 203:163989, feb 2020.

[121] Matheus Felipe Fagundes Das Neves, João Paulo Vita Damasceno, Soheila Holakoei, Maria Luiza M. Rocco, Aldo José Gorgatti Zarbin, Camilla Karla Brites Queiroz Martins De Oliveira, and Lucimara Stolz Roman. ***Enhancement of conductivity and transmittance of graphene oxide/PEDOT:PSS electrodes and the evaluation of charge transfer dynamics***. *J. Appl. Phys.*, 126(21), 2019.

[122] Diana Marcela Montoya, Enrique Pérez-Gutiérrez, Oracio Barbosa-Garcia, Wilson Bernal, José-Luis Maldonado, M. Judith Percino, Marco-Antonio Meneses, and Margarita Cerón. ***Defects at the interface electron transport layer and alternative counter electrode, their impact on perovskite solar cells performance***. *Sol. Energy*, 195:610–617, 2020.

[123] Enas Moustafa, Maria Méndez, José G. Sánchez, Josep Pallarès, Emilio Palomares, and Lluis F. Marsal. ***Thermal Activation of PEDOT:PSS/PM6:Y7 Based Films Leads to Unprecedent High Short-Circuit Current Density in Nonfullerene Organic Photovoltaics***. *Adv. Energy Mater.*, 13(4):26–29, 2023.

[124] Martina Dianetti, Gianpaolo Susanna, Emanuele Calabrò, Giuseppina Polino, Martin Otto, Daniel Neumaier, Andrea Reale, and Francesca Brunetti. ***Graphene with Ni-Grid as Semitransparent Electrode for Bulk Heterojunction Solar Cells (BHJ-SCs)***. *Polymers.*, 14(5):1–11, 2022.

[125] Zexia Zhang, Ruitao Lv, Yi Jia, Xin Gan, Hongwei Zhu, and Feiyu Kang. ***All-carbon electrodes for flexible solar cells***. *Appl. Sci.*, 8(2):1–11, 2018.

[126] Wenxia Zhang, Wei Song, Jiaming Huang, Like Huang, Tingting Yan, Jinfeng Ge, Ruixiang Peng, and Ziyi Ge. ***Graphene:silver nanowire composite transparent electrode based flexible organic solar cells with 13.4% efficiency***. *J. Mater. Chem. A*, 7(38):22021–22028, 2019.